Polarons

Interacting Impurities in Ultracold Gases

Rasmus Søgaard Christensen

PhD Dissertation

Supervisor: Georg M. Bruun

Institut for Fysik og Astronomi
Aarhus Universitet

Februar 2017

Til Mette, Frej og hvem der
ellers vil være med.

Dansk Resumé

Denne afhandling omhandler vekselvirkende urenheder i ultrakolde gasser. Når urenhederne vekselvirker med det omkringliggende miljø danner de kvasipartikler kaldet polaroner. Disse polaroner opfører sig som partikler med ændret energi og effektiv masse sammenlignet med de nøgne urenhedsatomer.

Denne først halvdel af afhandlingen omhandler spredningsraten for en bevægelig urenhed nedsunket i en ultrakold gas af fermioner, en Fermi-polaron. Spredningsraten diskuteres i stor detalje indenfor "Fermi ĺiquid"-teori. Efterfølgende benyttes spredningsraten til at modellere dekohærensraten af urenheder nedsunket i en Fermi gas. Et eksperiment udført af R. Grimms gruppe.

Anden halvdel af afhandlingen omhandler egenskaberne for en kvasipartikel formet af en bevægelig urenhed nedsunket i et Bose-Einstein kondensat, en Bose-polaron. Her beregnes energien, kvasipartikel-vægten og den effektive masse perturbativt til tredje(!) orden i spredningslængden for spredningen mellem en boson og et urenhedsatom. Efterfølgende benyttes perturbationsteorien til at modellere og verificere den allerførste observation af Bose-polaronen i et forsøg udført af J. Arlts gruppe ved Aarhus Universitet og i parallelt arbejde af D. Jin ved JILA, Colorado.

English Summary

The work of this thesis considers interacting impurities in ultracold gases. When the impurities interact with the environment they form quasiparticles coined polarons. These polarons behave as particles with a renormalised energy and an effective mass as compared to the bare impurity atoms.

The first half of this thesis considers the scattering rate of a mobile impurity emerged in an ultracold gas of fermions, a Fermi polaron. The scattering rate is discussed in detail within Fermi liquid theory. Afterwards, the scattering rate is used to model the observed decoherence rate of impurities emerged in a Fermi gas. An experiment performed by the group of R. Grimm.

The second half of this thesis discuss the quasiparticle properties of a mobile impurity emerged in a Bose-Einstein condensate, a Bose polaron. Here, the energy, the quasiparticle residue and the effective mass of the Bose polaron is obtained perturbatively to third(!) order in the impurity-Bose scattering length. Afterwards, the perturbation theory is used to model and verify the very first observation of the Bose polaron in an experiment performed by the group of J. Arlt at Aarhus University and in parallel work by D. Jin at JILA, Colorado.

List of Publications

- R. S. Christensen and G. M. Bruun. Quasiparticle scattering rate in a strongly polarized Fermi mixture. *Physical Review A*, **91**: 042702, 2015.
- M. Cetina, M. Jag, R. S. Lous, J. T. M. Walraven, R. Grimm, R. S. Christensen, and G. M. Bruun. Decoherence of Impurities in a Fermi Sea of Ultracold Atoms. *Physical Review Letters*, **115**: 135302, 2015.
- R. S. Christensen, J. Levinsen, and G. M. Bruun. Quasiparticle Properties of a Mobile Impurity in a Bose-Einstein Condensate. *Physical Review Letters*, **115**: 160401, 2015.
- N. B. Jørgensen et al. Observation of Attractive and Repulsive Polarons in a Bose-Einstein Condensate. *Physical Review Letters*, **117**: 055302, 2016.
- R. S. Christensen. *Progress Report: Polaron Physics*. Progress Report. Aarhus University, Apr. 2015.

Contents

CHAPTER

1 Introduction

Fundamentally, particles can be either bosonic or fermionic of nature.[1–5] Famously, Bose and Einstein predicted in 1924 the formation of a Bose-Einstein condensate (BEC), where a macroscopic number of bosons occupy a single wave function. This is in sharp contrast to the nature of fermions, where no identical particles can occupy the same wave function due to the Pauli exclusion principle.[6] Hence, the "most quantum" many-body system we can imagine for fermions, is a system where all the lowest energy states are occupied completely. The temperature scale for the onset of this quantum degeneracy is the same for bosons and fermions; $k_B T_{deg} \sim \hbar^2 n^{2/3}/m$, where n is the density, m the mass of the particles, and k_B and $\hbar$ are respectively the Boltzmann and Planck constants.[7]

Even though Bose-Einstein condensation was predicted in 1924, it was not realised experimentally until 1995, where multiple groups succeeded in cooling a gas of bosons to the quantum degeneracy

[1] S. N. Bose. *Z. Phys.*, **26**: 178–181, 1924.

[2] A. Einstein. *Quantentheorie des einatomigen idealen Gases*. Akademie der Wissenshaften, in Kommission bei W. de Gruyter, 1924.

[3] E. Fermi. *Z. Phys.*, **36**: 902–912, 1926.

[4] E. Fermi. *Rend. Lincei*, **3**: 145–149, 1926.

[5] P. A. M. Dirac. *Proc. R. Soc. A*, **112**: 661–677, 1926.

[6] W. Pauli. *Z. Phys.*, **31**: 765–783, 1925.

[7] S. Giorgini et al. *Rev. Mod. Phys.*, **80**: 1215–1274, 2008.

level.[8–10] An achievement for which E. Cornell, C. Wieman, and W. Ketterle was awarded the Nobel prize in 2001. Reaching the quantum degeneracy level for fermions has proven even harder, since the Pauli exclusion principle forbids *s*-wave scattering in a single component Fermi gas, which has drastic consequences for evaporative cooling mechanisms. Quantum degeneracy for fermions was eventually reached right around the turn of the century.[11–13]

Fermions at low temperatures were predicted by Bardeen, Cooper, and Schrieffer (BCS) to form a superconducting phase, where fermions of opposite spin and momentum pair up in Cooper pairs.[14–16] A phenomenon which has been observed in ultracold fermion gases.[17,18] Many more quantum many-body phenomena have been observed in these ultracold gases where temperatures reach nanokelvin and typical densities are $n \sim 1 \times 10^{15}\,\mathrm{cm}^{-3}$, e.g. the interference of two overlapping Bose-Einstein condensates, long-range phase coherence, quantized vortices and vortex lattices, and molecular condensates of bound pairs of fermions.[19] What all of these phenomena have in common is the existence of a coherent many-body state, a concept which was introduced phenomenologically by Ginzburg and Landau as far back as 1950 in order to explain superconductivity.[20]

Additionally, the discovery of Feshbach resonances for atoms was essential for achieving many of these many-body phenomena in

[8] K. B. Davis et al. *Phys. Rev. Lett.*, **75**: 3969–3973, 1995.
[9] M. H. Anderson et al. *Science*, **269**: 198–201, 1995.
[10] C. C. Bradley et al. *Phys. Rev. Lett.*, **75**: 1687–1690, 1995.
[11] B. DeMarco and D. S. Jin. *Science*, **285**: 1703–1706, 1999.
[12] F. Schreck et al. *Phys. Rev. Lett.*, **87**: 080403, 2001.
[13] A. G. Truscott et al. *Science*, **291**: 2570–2572, 2001.
[14] J. Bardeen. *Phys. Rev.*, **80**: 567–574, 1950.
[15] J. Bardeen et al. *Phys. Rev.*, **108**: 1175–1204, 1957.
[16] L. N. Cooper. *Phys. Rev.*, **104**: 1189–1190, 1956.
[17] C. A. Regal et al. *Phys. Rev. Lett.*, **92**: 040403, 2004.
[18] M. W. Zwierlein et al. *Nature*, **435**: 1047–1051, 2005.
[19] I. Bloch et al. *Rev. Mod. Phys.*, **80**: 885–964, 2008.
[20] L. D. Landau and V. Ginzburg. *Zh. Eksp. Teor. Fiz.*, **20**: 1064, 1950.

ultracold gases.[21–24] By exploiting a Feshbach resonance it is possible to tune the interaction between atoms to arbitrary strength and even from repulsive to attractive.

Recently, attention has turned to population imbalanced two component gases, where the population of one of the components (majority atoms) is larger than the population of the other component (minority atoms).[25–28] Making the population imbalance very large, the ultracold gases have opened up a whole new and ideal testbed for mobile impurities (minority atoms) interacting with a medium (majority atoms).[29,30]

Impurity physics or mobile impurities interacting with an environment poses a central problem for understanding quantum many-body systems. Landau and Pekar famously demonstrated that electrons in a dielectric medium are dressed by phonons forming quasi-particles termed polarons.[31–33] Polarons are now a core concept in our understanding of a range of many-body systems, ranging from semiconductors;[34] helium mixtures;[35] Λ particles in nuclear matter;[36] and high temperature superconductors[37] all the way to the standard model, where elementary particles acquire their mass by coupling

---

[21]H. Feshbach. *Ann. Phys.*, **19**: 287–313, 1962.
[22]W. C. Stwalley. *Phys. Rev. Lett.*, **37**: 1628–1631, 1976.
[23]S. Inouye et al. *Nature*, **392**: 151–154, 1998.
[24]C. Chin et al. *Rev. Mod. Phys.*, **82**: 1225–1286, 2010.
[25]G. B. Partridge et al. *Science*, **311**: 503–505, 2006.
[26]M. W. Zwierlein et al. *Science*, **311**: 492–496, 2006.
[27]F. Chevy and C. Mora. *Rep. Prog. Phys.*, **73**: 112401, 2010.
[28]K. Gubbels and H. Stoof. *Phys. Rep.*, **525**: 255–313, 2013.
[29]A. P. Chikkatur et al. *Phys. Rev. Lett.*, **85**: 483–486, 2000.
[30]N. Spethmann et al. *Phys. Rev. Lett.*, **109**: 235301, 2012.
[31]L. D. Landau. *Phys. Z. Sowjetunion*, **3**: 644, 1933.
[32]S. I. Pekar. *Zh. Eksp. Teor. Fiz.*, **16**: 335, 1946.
[33]L. D. Landau and S. I. Pekar. *Phys. Z. Sowjetunion*, **18**: 419, 1948.
[34]M. E. Gershenson et al. *Rev. Mod. Phys.*, **78**: 973–989, 2006.
[35]G. Baym and C. Pethick. *Landau Fermi-Liquid Theory: Concepts and Applications*. Wiley, 1991.
[36]R. Bishop. *Ann. Phys.*, **78**: 391–420, 1973.
[37]E. Dagotto. *Rev. Mod. Phys.*, **66**: 763–840, 1994.

to the Higgs boson.[38–40]

Recently, impurities interacting with a fermionic environment as well as impurities interacting with a bosonic environment have been realised.[41–46] These experiments have spawned new theoretical interest into impurity physics, where the polaron concept has experienced a successful renaissance. The interacting impurity atoms have been shown to form well-defined quasiparticles coined Fermi or Bose polarons depending on the nature of the environment.[47–51]

This thesis considers these interacting impurities or polarons. We shall model the decoherence rate of impurities emerged in a fermionic environment as the scattering of Fermi polarons, develop the quasiparticle properties of the Bose polaron perturbatively to third order, and model the observed signal from Bose polarons in a Bose-Einstein condensate. The last experiment presented the first ever observation of the Bose polaron, and the theory presented in this thesis was crucial for verifying the result.

Most of the cited work above considers three dimensional systems, which is also the focus of this thesis. In addition to three dimensional systems, one and two dimensional systems have also been realised in ultracold gases, where a wide range of phenomena including impurity physics have been studied. We will however not consider these studies here.

Finally, we note that we set $\hbar = k_{\mathrm{B}} = 1$ throughout this thesis.

---

[38] S. Chatrchyan et al. *Phys Lett. B*, **716**: 30, 2012.
[39] G. Aad et al. *Phys Lett. B*, **716**: 1, 2012.
[40] P. W. Higgs. *Phys. Rev. Lett.*, **13**: 508–509, 1964.
[41] A. Schirotzek et al. *Phys. Rev. Lett.*, **102**: 230402, 2009.
[42] C. Kohstall et al. *Nature*, **485**: 615–618, 2012.
[43] M. Koschorreck et al. *Nature*, **485**: 619–622, 2012.
[44] N. B. Jørgensen et al. *Phys. Rev. Lett.*, **117**: 055302, 2016.
[45] M.-G. Hu et al. *Phys. Rev. Lett.*, **117**: 055301, 2016.
[46] F. Scazza et al. *Phys. Rev. Lett.*, **118**: 083602, 2017.
[47] F. Chevy. *Phys. Rev. A*, **74**: 063628, 2006.
[48] P. Massignan et al. *Rep. Prog. Phys.*, **77**: 034401, 2014.
[49] J. Tempere et al. *Phys. Rev. B*, **80**: 184504, 2009.
[50] S. P. Rath and R. Schmidt. *Phys. Rev. A*, **88**: 053632, 2013.
[51] F. M. Cucchietti and E. Timmermans. *Phys. Rev. Lett.*, **96**: 210401, 2006.

Outline of the Thesis

Chapter 2 considers an impurity in an ultracold gas and presents a brief introduction to the core concepts and techniques used for the remaining part of the thesis. We briefly introduce the Feshbach resonance, the $\mathcal{T}$-matrix, and how the interacting impurity is described as a quasiparticle, before we discuss how an atom interacts with a laser field and the experimental technique of radio frequency spectroscopy.

Chapter 3 discusses the work done in Ref. [52], where we obtain the scattering rate for the Fermi polaron from the Boltzmann transport equation.

Chapter 4 uses the scattering rate obtained in chapter 3 to model the observed decoherence of impurities interacting with a fermionic environmnet in Ref. [53].

Chapter 5 discusses the work done in Ref. [54], where the quasiparticle properties of the Bose polaron are obtained perturbatively to third order.

Chapter 6 models the spectral signal from a Bose polaron in a trapped Bose-Einstein condensate observed in Ref. [44].

Chapter 7 ends this thesis with a conclusion and an outlook.

CHAPTER

2 Impurity In an Ultracold Gas

This thesis considers impurities in ultracold dilute gases of alkali atoms of bosonic or fermionic nature. Due to the diluteness and low temperatures of these systems, the typical scattering is binary, low-energy and s-wave and can be characterised by a single parameter: the scattering length a typically on the order of the van der Waals range $r_0 \approx 50 - 100\,a_0$. Since the systems are very dilute with a typical interparticle spacing on the order of $n^{-1/3} \sim 10\,000\,a_0$, we have respectively $na^3 \ll 1$ (Bose system) and $k_F a \ll 1$ (Fermi system) with n being the density of the system and $k_F = (6\pi^2 n)^{1/3}$ for spin-polarised Fermi systems.[55,56] Thus, typical interactions in these systems are very weak, but by exploiting Feshbach resonances the interactions can be tuned at will.[24]

In this chapter we present brief overview of the most important concepts for the modelling and observation of an impurity in an ultracold gas. We start by introducing the Feshbach resonance, before moving on to the central $\mathcal{T}$-matrix, modelling the interaction

[55] C. Pethick and H. Smith. *Bose-Einstein Condensation in Dilute Gases*. Cambridge University Press, 2002.

[56] W. Ketterle and Z. M. W. "Making, probing and understanding ultracold Fermi gases" in: *Proceedings of the International School of Physics "Enrico Fermi", Course CLXIV, Ultra-cold Fermi Gases*. ed. by M. Inguscio et al. IOS Press, 2007. pp. 95–287

[24] C. Chin et al. *Rev. Mod. Phys.*, **82**: 1225–1286, 2010.

between atoms, and the quasiparticle properties of an interacting impurity in an ultracold characterising our polaron. These concepts are introduced in various textbooks and are typically well-known by people working with theoretical many-body physics.[55,57–59] Thus, we do not re-derive these concepts in great detail, but focus on the last two sections of this chapter, where we introduce radio frequency (rf) spectroscopy. Rf spectroscopy is used extensively in the study impurities in ultracold gases, and we derive the central equations and provide a link from rf spectroscopy to the spectral function of the system.

2.1 FESHBACH RESONANCE

A Feshbach resonance for two scattering atoms occurs, when the energy of the incoming atoms is close an energy level of a bound state. The energy level of the bound state or dimer can be tuned by an externally applied magnetic field, and the Feshbach resonance can be modelled by an effective two-channel model considering an open and a closed scattering channel as depicted in Fig. 2.1(a).[24,55,60] The open (or background) channel is characterised by a potential asymptotically connecting to two free atoms for a large atomic separation R, and it is the only scattering channel in the absence of a Feshbach resonance. The closed channel is associated with a potential supporting bound states. Due to energy conservation, the bound state can never be a final state, when we only consider two atoms scattering, hence the denotation "closed channel".

Analysing the sketched two-channel model, the scattering length is described by the phenomenological expression[24,55,60]

$$a(B) = a_{\mathrm{bg}}\left(1 - \frac{\Delta B}{B - B_0}\right), \tag{2.1}$$

[57] A. Fetter and J. Walecka. *Quantum theory of many-particle systems*. McGraw-Hill, 1971.

[58] G. Mahan. *Many-Particle Physics*. Plenum Press, 1990.

[59] H. Bruus and K. Flensberg. *Many-Body Quantum Theory in Condensed Matter Physics: An Introduction*. Oxford University Press, 2004.

[60] A. J. Moerdijk et al. *Phys. Rev. A*, **51**: 4852–4861, 1995.

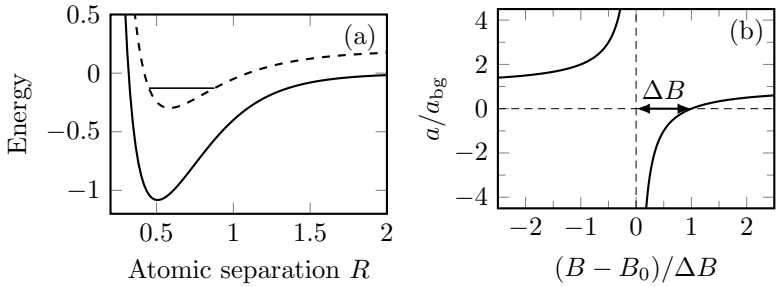

Figure 2.1: (a) Sketch of the two-channel model for the Feshbach resonance. The full line is the open channel scattering potential V_{o}, while the dashed line is the closed channel scattering potential V_{c} supporting a bound state. (b) The scattering length as a function of the externally applied magnetic field scanning across a Feshbach resonance. Both figures are inspired by figures in Ref. [24]

where a_{bg} is the background scattering length associated with scattering purely through the open channel, B is the externally applied magnetic field, B_0 is the position of the Feshbach resonance, where the bound state is resonant with the incoming atoms, and ΔB is a parameter characterising the width of the resonance. The three parameters characterising the Feshbach resonance: a_{bg}, B_0 and ΔB are all measured experimentally, and we show the scattering length as a function of magnetic field in Fig. 2.1(b).

From a theory point of view, we prefer working with the effective range $r_{\mathrm{eff}} = -(m_r a_{\mathrm{bg}} \delta\mu \Delta B)^{-1}$, where m_r is the reduced mass of the two atoms and $\delta\mu$ is the magnetic moment of the bound state with respect to the two atoms in the open channel.[55] Finally, we denote a Feshbach resonance with r_{eff} small (ΔB large) a broad resonance and a resonance with r_{eff} large (ΔB small) a narrow resonance. In this thesis we describe all scattering of atoms through $\mathcal{T}$-matrices and the size of r_{eff} determines whether we need to include the closed channel in the $\mathcal{T}$-matrix. For a narrow resonance we explicitly include the closed channel, while it can be ignored for a broad resonance.

2.2 $\mathcal{T}$-MATRIX

Throughout this thesis we rely heavily on the concepts of Green's functions, Feynman diagrams and the $\mathcal{T}$-matrix in the ladder approximation. These concepts can be found in various textbooks and hence, will not be re-derived in great detail here.[57–59] We present a brief derivation of the open channel scattering $\mathcal{T}$-matrix in the ladder approximation between two atoms of different species, before moving on to the discussion of an interacting impurity in an ultracold gas.

We denote the two atoms by respectively spin-$\downarrow$ and spin-$\uparrow$, which can be either atoms of different species or atoms of the same species, but in different hyperfine states. An effective Hamiltonian describing the open channel scattering of such atoms is

$$\mathscr{H} = \sum_{p,\sigma} \xi_{p\sigma} c^\dagger_{p\sigma} c_{p\sigma} + \frac{1}{\mathcal{V}} \sum_{p,p',q} V_{\mathrm{o}}(\boldsymbol{q}) c^\dagger_{p+q\downarrow} c^\dagger_{p'-q\uparrow} c_{p'\uparrow} c_{p\downarrow}, \tag{2.2}$$

where $c_{p\sigma}(c^\dagger_{p\sigma})$ is the annihilation (creation) operator for a spin-σ atom with momentum $\boldsymbol{p}$, $\xi_{p\sigma} = p^2/2m_\sigma - \mu_\sigma$ is the atomic kinetic energy with μ_σ the chemical potential of the spin-σ atoms, $V_{\mathrm{o}}(\boldsymbol{q})$ is the open channel scattering potential and $\mathcal{V}$ is the volume of the system. We assume the scattering potential V_{o} to be short-ranged and momentum independent, hence we replace the potential $V_{\mathrm{o}}(\boldsymbol{q})$ by the pseudopotential g_{o} which we require to correctly reproduce the two-body scattering properties in vacuum.[57]

From this Hamiltonian we define the associated Green's functions and Feynman rules for drawing Feynman diagrams. For instance, the Green's function for a freely propagating atom is given by

$$\begin{aligned} G_\sigma(\boldsymbol{p}, i\omega_\lambda) &= -\left\langle \mathscr{T}\left\{ c_{p,\sigma}(\tau) c^\dagger_{p,\sigma}(0) \right\} \right\rangle \\ &= \frac{1}{i\omega_\lambda - \xi_{p\sigma}}, \end{aligned} \tag{2.3}$$

where $\mathscr{T}$ is the time-ordering operator with respect to the imaginary time τ and $\omega_\lambda = \lambda\pi/\beta$ is a Matsubara frequency with $\beta = 1/T$ and λ being an odd (even) integer for a fermion (boson).

We define the $\mathcal{T}$-matrix in the ladder approximation as the infinite resummation of scattering events between the two propagating particles. Graphically, in terms of Feynman diagrams, we have

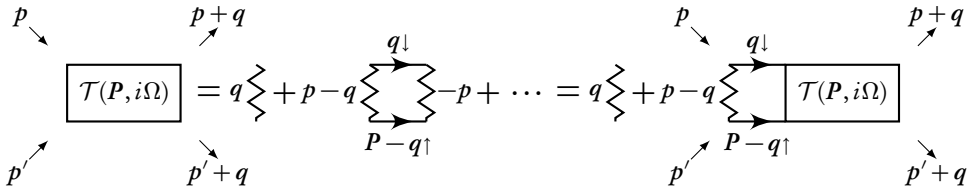

where $\boldsymbol{P} = \boldsymbol{p}+\boldsymbol{p}'$ and $i\Omega = i\omega_\lambda + i\omega_\nu$. Thus, we define the $\mathcal{T}$-matrix graphically by

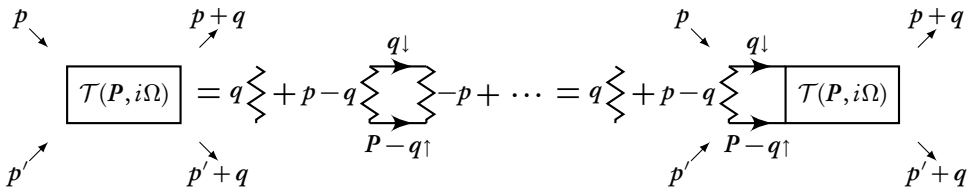

where it is understood that all outer points contains a vertex, where incoming and outgoing particle lines should be connected. For clarity, we have left out the Matsubara frequencies in the last diagram. The diagram corresponds to the equation

$$\mathcal{T}(\boldsymbol{P}, i\Omega) = \mathrm{g}_\mathrm{o} + \mathrm{g}_\mathrm{o}\Pi(\boldsymbol{P}, i\Omega)\mathcal{T}(\boldsymbol{P}, i\Omega) \tag{2.4}$$

which is the Lippmann-Schwinger equation defining the $\mathcal{T}$-matrix in the ladder approximation, and we have defined the pair-propagator for two propagating atoms[57]

$$\begin{aligned}\Pi(\boldsymbol{P}, i\Omega) &= -\frac{1}{\beta}\sum_{i\omega_q}\frac{1}{\mathcal{V}}\sum_{\boldsymbol{q}} G_\downarrow(\boldsymbol{q}, i\omega_q)G_\uparrow(\boldsymbol{P}-\boldsymbol{q}, i\Omega - i\omega_q) \\ &= \int\frac{\mathrm{d}^3q}{(2\pi)^3}\frac{1 \pm n_\downarrow(\epsilon_{q\downarrow}) \pm n_\uparrow(\epsilon_{P-q\downarrow})}{i\Omega - \xi_{q\downarrow} - \xi_{P-q\uparrow}},\end{aligned} \tag{2.5}$$

where $\pm n_\sigma(\epsilon_p) = [e^{\beta(\epsilon_{p\sigma}-\mu_\sigma)} \mp 1]^{-1}$ with $\epsilon_{p\sigma} = p^2/2m_\sigma$ is either the Bose or Fermi distribution depending on the nature of the propagating atoms. We use the upper (lower) sign for a Bose (Fermi)

distribution. The pair-propagator is ultraviolet divergent, but by inverting Eq. (2.4) and relating the zero energy, vacuum $\mathcal{T}$-matrix to the scattering length a through

$$\frac{2\pi a}{m_r} \equiv \mathcal{T}_v^{-1}(0,0) = g_0^{-1} - \Pi_v(0,0), \tag{2.6}$$

we relate the scattering potential to the scattering length through $g_0^{-1} = \mathcal{T}_v^{-1}(0,0) + \Pi_v(0,0)$, which we then use to express the $\mathcal{T}$-matrix Eq. (2.4) as

$$\begin{aligned} \mathcal{T}^{-1}(\boldsymbol{P}, i\Omega) &= \mathcal{T}_v^{-1}(0,0) - \left[\Pi(\boldsymbol{P}, i\Omega) - \Pi_v(0,0)\right] \\ \mathcal{T}(\boldsymbol{P}, i\Omega) &= \frac{\mathcal{T}_v(0,0)}{1 + \mathcal{T}_v(0,0)\tilde{\Pi}(\boldsymbol{P}, i\Omega)}, \end{aligned} \tag{2.7}$$

where

$$\begin{aligned} \tilde{\Pi}(\boldsymbol{P}, i\Omega) &\equiv \Pi(\boldsymbol{P}, i\Omega) - \Pi_v(0,0) \\ &= \int \frac{\mathrm{d}^3 q}{(2\pi)^3} \left[\frac{1 \pm n_\downarrow(\epsilon_{q\downarrow}) \pm n_\uparrow(\epsilon_{\boldsymbol{P}-q\downarrow})}{i\Omega - \xi_{q\downarrow} - \xi_{\boldsymbol{P}-q\uparrow}} + \frac{2m_r}{q^2} \right] \end{aligned} \tag{2.8}$$

is the convergent renormalised pair-propagator. For the remaining part of this thesis, we use the renormalised pair-propagator, and we will thus drop the tilde-notation and simply denote the renormalised pair-propagator by $\Pi(\boldsymbol{P}, i\Omega)$. Finally, we note that in order to relate the Matsubara frequencies to real energies, we do analytic continuation, taking $i\omega \to \omega + i\eta$, where η is an infinitesimal positive quantity.

2.3 INTERACTING IMPURITY IN AN ULTRACOLD GAS

Throughout this thesis we investigate impurities interacting with either a fermionic or bosonic environment. The impurity interacting with an environment forms a quasiparticle termed a polaron, named after Landau and Pekar's famous study of electrons in a dielectric medium forming quasiparticles.[31,32] We denote the quasiparticle

[31] L. D. Landau. *Phys. Z. Sowjetunion*, **3**: 644, 1933.

[32] S. I. Pekar. *Zh. Eksp. Teor. Fiz.*, **16**: 335, 1946.

formed when an impurity interacts with a bosonic (fermionic) environment by Bose (Fermi) polaron, and we determine the quasiparticle properties of the polaron from the associated self-energy.[57–59] In the following two sections, we briefly present theory on the self-energy and the derived quasiparticle properties relevant for this thesis.

Self-Energy

The self-energy is defined as the sum of all irreducible Feynman diagrams for the polaron propagator without the two external lines. This is perhaps better understood by investigating the Dyson equation for a propagating polaron, i.e. an impurity interacting with an environment. Since we assume all scattering to happen within the ladder approximation for the $\mathcal{T}$-matrix, the Dyson equation for the propagating polaron is

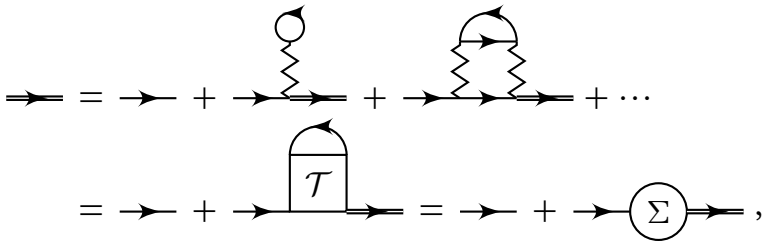

(2.9)

defining the self-energy as

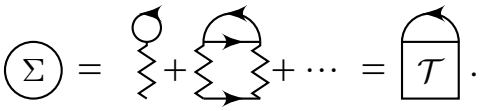

(2.10)

In Eq. (2.9) a thick line corresponds to the propagating polaron with Green's function G, while a thin line corresponds to the freely propagating impurity with Green's function G^0 given by Eq. (2.3). Expressing Eq. (2.9) algebraically, we write the polaron propagator as

$$G(\boldsymbol{p}, i\omega_\lambda) = G^0(\boldsymbol{p}, i\omega_\lambda) + G^0(\boldsymbol{p}, i\omega_\lambda)\Sigma(\boldsymbol{p}, i\omega_\lambda)G(\boldsymbol{p}, i\omega_\lambda), \tag{2.11}$$

which is easily solved

$$G(\boldsymbol{p},\omega) = \frac{1}{\omega - \epsilon_p - \Sigma(\boldsymbol{p},\omega) + i\eta}, \tag{2.12}$$

where we have inserted the free propagator Eq. (2.3) and done analytic continuation by taking $i\omega_\lambda \to \omega + i\eta$. We see from Eq. (2.12) that the self-energy $\Sigma(\boldsymbol{p},\omega)$ enters directly as a correction to the unperturbed energy taking $\epsilon_p \to \epsilon_p + \Sigma(\boldsymbol{p},\omega)$, hence the name self-energy.

Quasiparticle Properties And Spectral Function

As stated above, we can derive various quasiparticle properties from the self-energy or actually from the polarons Greens function as given by Eq. (2.12). We derive the polarons energy E_{pol}, quasiparticle residue Z, effective mass m^* and the lifetime τ, and then we will give an interpretation of these afterwards.

We start from Eq. (2.12) by explicitly splitting the self-energy into its real and imaginary parts

$$G(\boldsymbol{p},\omega) = \frac{1}{\omega - \epsilon_p - \mathfrak{Re}[\Sigma(\boldsymbol{p},\omega)] - i\mathfrak{Im}[\Sigma(\boldsymbol{p},\omega)]}. \tag{2.13}$$

From this equation we solve for the energy, by self-consistently solving

$$E_{\text{pol}} = \epsilon_p + \mathfrak{Re}[\Sigma(\boldsymbol{p}, E_{\text{pol}})] \tag{2.14}$$

for E_{pol}. The main assumption throughout this thesis is that a well-defined quasiparticle exists for small excitations around E_{pol} and for low momentum. Letting the energy of the zero momentum polaron be E_{pol}, we expand the real part of the self-energy around

$(\boldsymbol{p},\omega)\to(0,E_{\rm pol})$ to obtain

$$\begin{aligned}G(\boldsymbol{p},\omega)&\approx\Big(\omega-E_{\rm pol}-\omega\,\partial_\omega\big(\mathfrak{Re}[\Sigma(0,\omega)]\big)\Big|_{\omega=E_{\rm pol}}\\&\qquad-p^2\,\partial_{p^2}\big[\epsilon_p+\mathfrak{Re}[\Sigma(\boldsymbol{p},0)]\big]\Big|_{p^2=0}-i\,\mathfrak{Im}[\Sigma(\boldsymbol{p},\omega)]\Big)^{-1}\\&=\Big(1-\partial_\omega\big(\mathfrak{Re}[\Sigma(0,\omega)]\big)\Big|_{\omega=E_{\rm pol}}\Big)^{-1}\\&\quad\times\Big(\omega-Zp^2\big[\frac{1}{2m}+\partial_{p^2}\mathfrak{Re}[\Sigma(\boldsymbol{p},0)]\Big|_{p^2=0}\big]-iZ\,\mathfrak{Im}[\Sigma(\boldsymbol{p},\omega)]\Big)^{-1}\\&=\frac{Z}{\omega-E_{\rm pol}-\frac{p^2}{2m^*}-i\frac{1}{2\tau_p(\omega)}},\end{aligned}\tag{2.15}$$

where we have introduced

$$Z^{-1}\equiv Z(\omega=E_{\rm pol})=1-\partial_\omega\big(\mathfrak{Re}[\Sigma(0,\omega)]\big)\Big|_{\omega=E_{\rm pol}},\tag{2.16}$$

$$\frac{m}{m^*}=Z\Big(1+2m\,\partial_{p^2}\mathfrak{Re}[\Sigma(\boldsymbol{p},0)]\Big|_{p^2=0}\Big),\tag{2.17}$$

$$\frac{1}{\tau_p(\omega)}=-2Z(\omega)\mathfrak{Im}[\Sigma(\boldsymbol{p},\omega)].\tag{2.18}$$

Thus, for small excitations we expect the energy of the quasiparticle ω to behave as

$$\omega-E_{\rm pol}=\frac{p^2}{2m^*}=Zp^2\Big(\frac{1}{2m}+\partial_{p^2}\mathfrak{Re}[\Sigma(\boldsymbol{p},0)]\Big|_{p^2=0}\Big)\tag{2.19}$$

which is the defining relation for the effective mass m^*.

We can interpret the Green's function Eq. (2.15) as a (free) quasiparticle with weight (residue) Z and mass m^*. To see this, we determine the spectral function in the vicinity of the peak $\omega\simeq E_{\rm pol}$. Expanding around $E_{\rm pol}$, we write

$$\begin{aligned}\mathfrak{Re}[\Sigma(\boldsymbol{p},\omega)]&\simeq\mathfrak{Re}[\Sigma(\boldsymbol{p},E_{\rm pol})]+(\omega-E_{\rm pol})\partial_\omega\mathfrak{Re}[\Sigma(\boldsymbol{p},\omega)]\Big|_{\omega=E_{\rm pol}}\\&=E_{\rm pol}-\epsilon_p+(\omega-E_{\rm pol})\partial_\omega\mathfrak{Re}[\Sigma(\boldsymbol{p},\omega)]\Big|_{\omega=E_{\rm pol}}\end{aligned}\tag{2.20}$$

such that the spectral function around E_{pol} is approximately given by

$$A(\boldsymbol{p},\omega) = -2\Im\mathfrak{m}[G(\boldsymbol{p},\omega)] \tag{2.21}$$

$$= \frac{-2\Im\mathfrak{m}[\Sigma(\boldsymbol{p},\omega)]}{\left(\omega-\epsilon_p-\Re\mathfrak{e}[\Sigma(\boldsymbol{p},\omega)]\right)^2+\left(\Im\mathfrak{m}[\Sigma(\boldsymbol{p},\omega)]\right)^2} \tag{2.22}$$

$$\simeq \frac{-2\Im\mathfrak{m}[\Sigma(\boldsymbol{p},E_{\text{pol}})]}{[(\omega-E_{\text{pol}})/Z(E_{\text{pol}})]^2+(\Im\mathfrak{m}[\Sigma(\boldsymbol{p},E_{\text{pol}})])^2}\,. \tag{2.23}$$

We can obtain the real time Green's function by a Fourier transform of Eq. (2.23) as

$$\begin{aligned} G(\boldsymbol{p},t) &= \frac{\theta(t)}{2\pi}\int_{-\infty}^{\infty} \mathrm{d}\omega\, e^{-i\omega t}A(\boldsymbol{p},\omega) \\ &= \theta(t)Z(E_p)e^{-iE_{\text{pol}}t}e^{Z(E_p)\Im\mathfrak{m}[\Sigma(\boldsymbol{p},E_{\text{pol}})]t}\,, \end{aligned} \tag{2.24}$$

where we have assumed $Z(E_p)\Im\mathfrak{m}[\Sigma(\boldsymbol{p},E_{\text{pol}})]>0$. This motivates the definition of lifetime in Eq. (2.18), since we associate a decaying Green's function with an amplitude decay: $\langle a(t)a^\dagger(0)\rangle$. Hence, a particle decay with lifetime τ is associated with $|\langle a(t)a^\dagger(0)\rangle|^2 \propto e^{-t/\tau}$ and thus, requiring $G(\boldsymbol{p},t)\propto e^{-t/2\tau}$ we have $Z\Im\mathfrak{m}[\Sigma]=-1/2\tau$.

Expressing Eq. (2.23) in terms of the lifetime, we have

$$A(\boldsymbol{p},E_{\text{pol}}) \simeq Z(E_{\text{pol}})\frac{1/\tau_p}{(\omega-E_{\text{pol}})^2+(1/2\tau_p)^2}\,, \tag{2.25}$$

which we identify as a Lorentzian shape. Furthermore we notice that if the lifetime goes to infinity ($\Im\mathfrak{m}\Sigma\to 0$), the spectral function approaches a δ-function

$$\lim_{\tau\to\infty} A(\boldsymbol{p},\omega) = 2\pi Z(E_{\text{pol}})\delta(\omega-E_{\text{pol}}). \tag{2.26}$$

Hence, for a well-defined quasiparticle with a long lifetime, we have a distinct peak of weight Z in the spectral function. However, since the general sum rule requires the spectral function to integrate to 1 and $Z\leq 1$ this is not the whole story. Thus, there is a part of the

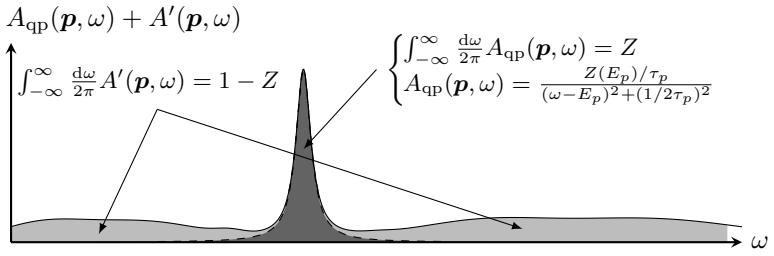

Figure 2.2: A generic spectral function for an impurity interacting with an ultracold gas. We have a distinct quasiparticle peak $A_{\rm qp}$ with spectral weight Z and a continuum of excited states of total weight $1-Z$. Figure, inspired from Fig. 15.2 of Ref. [59].

spectral function not associated with the quasiparticle of total weight $1-Z$. Denoting the quasiparticle part of the spectral function by $A_{\rm qp}$ and the remaining part by A', we thus have

$$\frac{1}{2\pi}\int_{-\infty}^{\infty} \mathrm{d}\omega\, A_{\rm qp}(\boldsymbol{p},\omega) + \frac{1}{2\pi}\int_{-\infty}^{\infty} \mathrm{d}\omega\, A'(\boldsymbol{p},\omega) = 1, \tag{2.27}$$

where $A_{\rm qp}(\boldsymbol{p},\omega)$ is given by Eq. (2.25). We show a sketch of the spectral function in Fig. 2.2, where we see a distinct quasiparticle peak (and hence a well-defined quasiparticle) and a continuum of more complicated excitations of the systems associated with A'.

Another, maybe more intuitive, way of understanding the quasiparticle residue Z is through Chevy's ansatz, which has successfully characterised the Fermi polaron.[47,48,61] Chevy's ansatz is a variational ansatz expanding the many-body wave function of an impurity emerged in a Fermi sea in terms of the number of particle-hole excitations in the Fermi sea, such that the wave function is expressed as

$$|\psi\rangle = \sqrt{Z} c_{0\downarrow}^{\dagger}|\mathrm{FS}\rangle + \sum_{q<k_{\rm F}<p} \phi_{q,k} c_{q-p\downarrow}^{\dagger} c_{p\uparrow}^{\dagger} c_{q\uparrow}|\mathrm{FS}\rangle + \cdots, \tag{2.28}$$

[47] F. Chevy. *Phys. Rev. A*, **74**: 063628, 2006.
[48] P. Massignan et al. *Rep. Prog. Phys.*, **77**: 034401, 2014.
[61] Z. Lan and C. Lobo. *J. Indian Inst. Sci.*, , 2014.

where $c^\dagger_{p\downarrow}$ ($c^\dagger_{p\uparrow}$) creates an impurity (majority) atom with momentum p, $|FS\rangle$ is the wave function of the Fermi sea of majority atoms and $Z, \phi_{q,k}$ are variational parameters. One can show that the variational parameter Z is exactly the quasiparticle residue as introduced above. Hence, we see that the quasiparticle residue directly enters as the weight $\langle \mathrm{FS}|c_{0\downarrow}\sqrt{Z}|\psi\rangle = Z$ of the single impurity on top of a Fermi sea.

2.4 ATOM INTERACTING WITH A LASER FIELD

A great part of this thesis is devoted to relating the theoretical properties of polarons to experimentally measurable quantities. In this and the following section, we will introduce radio frequency (rf) spectroscopy, which is used experimentally to determine quasiparticle properties such as the energy and quasiparticle residue. We consider an impurity in a surrounding medium of majority atoms and model the internal state of the impurity atom as a two level atom with the two internal states $|1\rangle$ and $|2\rangle$ of energy E_1 and E_2 respectively. $|1\rangle$ is a non-interacting state which does not interact with the surrounding environment, while $|2\rangle$ is an interacting state which interacts with the surrounding medium. When the surrounding medium of majority atoms is not present, the energy splitting between the two states is ω_0, while the energy splitting is $E_1 - E_2 = \omega_{12} = \omega_0 - E_{\mathrm{pol}}$ when the surrounding medium is present as shown in Fig. 2.3. Hence, the polaron energy is defined as the additional energy shift of the interacting state $|2\rangle$ when the medium is present as compared to vacuum, $E_{\mathrm{pol}} = \omega_0 - \omega_{21}$.[44] We stress that this defines the polaron energy shown in Fig. 2.3 as negative. This rather unintuitive way of the defining the polaron energy mimics the definition of the polaron energy in Ref. [44], where the non-interacting state has a higher energy than the interacting state in vacuum.

In the following we start by discussing a two level atom interacting with a classical laser field, before introducing the Bloch sphere and formalising rf spectroscopy.

[44] N. B. Jørgensen et al. *Phys. Rev. Lett.*, **117**: 055302, 2016.

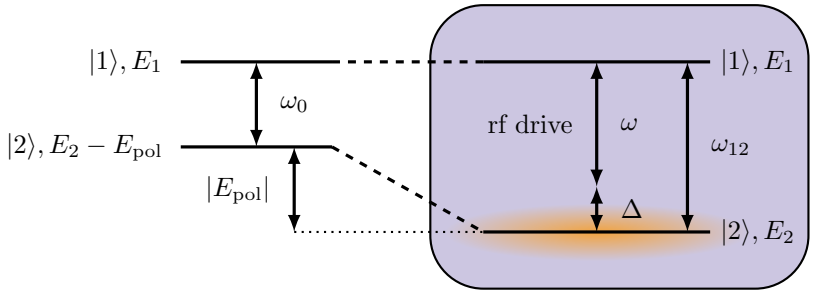

Figure 2.3: A two level atom with (right) and without (left) the medium gas of majority atoms present (see text). (Vertical energy is not to scale.)

Atom Interacting With a Classical Field

We quantify the internal state of the impurity atom with the general state vector

$$|\psi\rangle = c_1|1\rangle + c_2|2\rangle = \begin{pmatrix} c_2 \\ c_1 \end{pmatrix} \tag{2.29}$$

or equivalently by the 2×2 density matrix

$$\rho = \begin{pmatrix} \rho_{22} & \rho_{21} \\ \rho_{12} & \rho_{11} \end{pmatrix} = |\psi\rangle\langle\psi| = \begin{pmatrix} c_2 \\ c_1 \end{pmatrix} \begin{pmatrix} c_2^* & c_1^* \end{pmatrix} = \begin{pmatrix} |c_2|^2 & c_2 c_1^* \\ c_1 c_2^* & |c_1|^2 \end{pmatrix}, \tag{2.30}$$

where the entries are the expectation values $\langle\psi|\hat{\rho}|\psi\rangle$ of the density operator $\hat{\rho} = \begin{pmatrix} |2\rangle\langle 2| & |2\rangle\langle 1| \\ |1\rangle\langle 2| & |1\rangle\langle 1| \end{pmatrix}$.

When no external field is present, the evolution of the internal state vector is described by the Hamiltonian[62]

$$\hat{\mathcal{H}}_0 = E_1|1\rangle\langle 1| + E_2|2\rangle\langle 2| = \frac{\omega_{12}}{2}\big(|2\rangle\langle 2| - |1\rangle\langle 1|\big) = \frac{\omega_{12}}{2}\hat{\sigma}_z, \tag{2.31}$$

where we measure the energy relative to $(E_2 + E_1)/2$. $\hat{\sigma}_z$ is the z Pauli matrix and for reference, we state the three Pauli matrices in

[62] D. A. Steck *Quantum and Atom Optics* available online at `http://steck.us/teaching` (revision 0.11.5, 27 November 2016)

this basis:

$$\hat{\sigma}_x = \begin{pmatrix} 0 & 1 \\ 1 & 0 \end{pmatrix} = |2\rangle\langle 1| + |1\rangle\langle 2|, \quad \hat{\sigma}_y = \begin{pmatrix} 0 & -i \\ i & 0 \end{pmatrix} = i(|1\rangle\langle 2| - |2\rangle\langle 1|), \\ \hat{\sigma}_z = \begin{pmatrix} 1 & 0 \\ 0 & -1 \end{pmatrix} = |2\rangle\langle 2| - |1\rangle\langle 1|. \tag{2.32}$$

The time-evolution of the system when there is no external field present is trivially given by $c_1(t) = e^{i\omega_{12}t/2}c_1(t=0)$ and $c_2(t) = e^{-i\omega_{12}t/2}c_2(t=0)$.

A two level atom interaction with a classical field can be found in multiple textbooks. Here, we roughly follow Ref. [62]. Introducing an externally applied rf field with frequency ω and phase ϕ, we obtain within the dipole approximation the coupling

$$\hat{\mathcal{H}}_{\mathrm{rf}} = \Omega\cos(\omega t + \phi)\big(|1\rangle\langle 2| + |2\rangle\langle 1|\big) \tag{2.33}$$

$$\approx \frac{\Omega}{2}\big(e^{i(\omega t+\phi)}|1\rangle\langle 2| + e^{-i(\omega t+\phi)}|2\rangle\langle 1|\big), \tag{2.34}$$

where $\Omega = -E_0\langle 1|\hat{\epsilon}\cdot\boldsymbol{d}|2\rangle$ is the Rabi frequency with E_0 being the amplitude and $\hat{\epsilon}$ the polarization of the applied field and $\boldsymbol{d}$ is the dipole operator of the atom. In the second line we have applied the rotating wave approximation by ignoring the two rapidly oscillating terms, when we assume the rf driving frequency to be close to resonance $\omega \simeq \omega_{12}$ and recognize that the expectation value $|1\rangle\langle 2|$ is $\rho_{21} \propto e^{-i\omega_{12}t}$ and likewise for $|2\rangle\langle 1|$ is $\propto e^{i\omega_{12}t}$ in the absence of an externally applied field.

With the resulting Hamiltonian $\hat{\mathcal{H}} = \hat{\mathcal{H}}_0 + \hat{\mathcal{H}}_{\mathrm{rf}}$ the time evolution of the density matrix is given by the von Neumann equation: $\partial_t\rho = -i[\mathcal{H},\rho] = -i[\mathcal{H}_0 + \mathcal{H}_{\mathrm{rf}},\rho]$, yielding

$$\partial_t\rho = \begin{pmatrix} i\frac{\Omega}{2}\big(\rho_{21}e^{i(\omega t+\phi)} - \rho_{12}e^{-i(\omega t+\phi)}\big) & -i\omega_{12}\rho_{21} + i\frac{\Omega}{2}\big(\rho_{22}-\rho_{11}\big)e^{-i(\omega t+\phi)} \\ i\omega_{12}\rho_{12} - i\frac{\Omega}{2}\big(\rho_{22}-\rho_{11}\big)e^{i(\omega t+\phi)} & -i\frac{\Omega}{2}\big(\rho_{21}e^{i(\omega t+\phi)} - \rho_{12}e^{-i(\omega t+\phi)}\big) \end{pmatrix}.$$

In order to simplify this equation, we transform into a co-rotating frame introducing $\tilde{c}_1(t) = c_1(t)e^{-i\omega_{12}t/2}$ and $\tilde{c}_2(t) = c_2(t)e^{i(\omega-\omega_{12}/2)t}$ corresponding to the two unitary transformations:

$$U_1 = e^{-i\omega_{12}t/2|1\rangle\langle 1|}, \qquad U_2 = e^{i(\omega-\omega_{12}/2)t|1\rangle\langle 1|}. \tag{2.35}$$

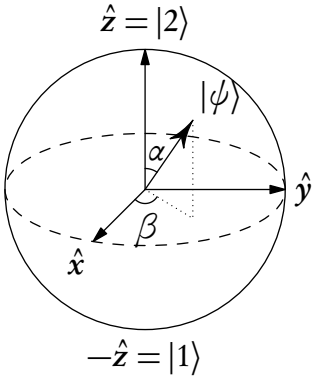

Figure 2.4: Bloch Sphere (see text). Adopted from Ref. [63].

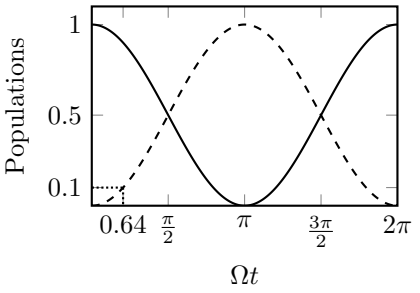

Figure 2.5: Rabi oscillations. The full (dashed) line is the population of the state $|1\rangle$ ($|2\rangle$) as a function of time, when a resonant laser field is applied to a two level atom initially in the $|1\rangle$ state.

Defining $\tilde{\rho}_{ij} = \tilde{c}_i \tilde{c}_j^*$, we obtain the equations of motion for $\tilde{\rho}$:

$$\partial_t \tilde{\rho} = \begin{pmatrix} i\frac{\Omega}{2}(\tilde{\rho}_{21}e^{i\phi} - \tilde{\rho}_{12}e^{-\phi}) & i\Delta\tilde{\rho}_{21} + i\frac{\Omega}{2}(\rho_{22} - \rho_{11})e^{-i\phi} \\ -i\Delta\tilde{\rho}_{12} - i\frac{\Omega}{2}(\rho_{22} - \rho_{11})e^{i\phi} & -i\frac{\Omega}{2}(\tilde{\rho}_{21}e^{i\phi} - \tilde{\rho}_{12}e^{-i\phi}) \end{pmatrix}, \quad (2.36)$$

where we have introduced $\Delta = \omega - \omega_{12}$. Note that $\tilde{\rho}_{ii} = \rho_{ii}$ and hence the populations are unaltered in the rotating frame.

Bloch Sphere And Bloch Vector

As an alternative to the density matrix, we introduce the Bloch vector

$$\langle \boldsymbol{\sigma} \rangle = \begin{pmatrix} \langle \hat{\sigma}_x \rangle \\ \langle \hat{\sigma}_z \rangle \\ \langle \hat{\sigma}_z \rangle \end{pmatrix} = \begin{pmatrix} \tilde{\rho}_{21} + \tilde{\rho}_{12} \\ i(\tilde{\rho}_{21} - \tilde{\rho}_{12}) \\ \tilde{\rho}_{22} - \tilde{\rho}_{11} \end{pmatrix} \quad (2.37)$$

which has the expectation values of the Pauli matrices as entries. This maps the systems three degrees of freedom onto the Bloch sphere shown in Fig. 2.4. We introduce an equation of motion for the Bloch

vector by combining Eqs. (2.37) and (2.36) to obtain

$$\begin{aligned}\partial_t \langle \boldsymbol{\sigma} \rangle &= \begin{pmatrix} \Delta \langle \hat{\sigma}_y \rangle + \Omega \langle \hat{\sigma}_z \rangle \sin\phi \\ -\Delta \langle \hat{\sigma}_x \rangle - \Omega \langle \hat{\sigma}_z \rangle \cos\phi \\ \Omega \langle \hat{\sigma}_y \rangle \cos\phi - \Omega \langle \hat{\sigma}_x \rangle \sin\phi \end{pmatrix} \\ &= -\Delta\, \hat{\boldsymbol{z}} \times \langle \boldsymbol{\sigma} \rangle + \Omega\, \boldsymbol{n} \times \langle \boldsymbol{\sigma} \rangle\,, \end{aligned} \tag{2.38}$$

where $\boldsymbol{n} = (\cos\phi, \sin\phi, 0)$ and $\hat{z}$ is the unit vector in the z direction on the Bloch sphere. Thus, we see that it is possible to represent the internal degrees of freedom for the impurity atom by a Bloch vector processing around the vector $\Omega \boldsymbol{n} - \Delta \hat{\boldsymbol{z}}$.

The Bloch vector, originally introduced to describe nuclear magnetization in a magnetic field, is an useful tool to describe the internal degrees of freedom for our impurity atom.[64,65] First off, we immediately see from Eq. (2.37) that the z component of the Bloch vector directly quantifies to which degree the impurity is in the state $|1\rangle$ or $|2\rangle$ respectively. The x and y components are related to the coherences, and the azimuthal angle of the Bloch vector is directly related to the relative phase between the states $|1\rangle$ and $|2\rangle$. Investigating the time dependence of the Bloch vector Eq. (2.38), we see that applying a resonant laser field ($\Delta = 0$) corresponds to rotating around the $\boldsymbol{n}$-vector at rate Ω, while in the absence of an applied laser field ($\Omega = 0$) the Bloch vector simply rotates around the $\hat{\boldsymbol{z}}$ axis at a rate Δ. Note that the rotation speed here is $\Delta = \omega - \omega_{12}$, since we are in the rotating frame of reference with $\tilde{c}_1$ and $\tilde{c}_2$. Shifting back to the stationary frame of reference with c_1 and c_2 the relative phase of the two states are $e^{-i\omega_{12}t}$ as expected and stated following Eq. (2.32).

π- and $\pi/2$-pulse

Following the discussion above, we see that starting with the impurity in the non-interacting state $|1\rangle$ and applying a resonant laser field ($\Delta = 0$), the Bloch vector rotates from its starting point pointing downwards, around the vector $\boldsymbol{n}$ in the xy-plane at a rate Ω.

[64] F. Bloch. *Phys. Rev.*, **70**: 460–474, 1946.

[65] F. Arecchi and R. Bonifacio. *IEEE J. Quantum Electron.*, **1**: 169–178, 1965.

Hence, applying the resonant laser field for a time $t_{\pi/2}$ defined by $\Omega t_{\pi/2} = \pi/2$ the atom will end in an equal superposition of the two states as shown in Fig. 2.5. Likewise, applying the laser field for a time $t_\pi = 2t_{\pi/2}$ the system will cause the impurity initially in the non-interacting state to end up fully in the interacting state $|2\rangle$. A laser pulse of duration $t_{\pi/2}$ is denoted a $\frac{\pi}{2}$-pulse while a pulse of duration t_π is a π-pulse.

In fact, when a resonant laser field is applied, the resulting equations of motion Eq. (2.36) corresponds to an effective Hamiltonian

$$\mathcal{H}_{\text{eff}} = \frac{\Omega}{2}\begin{pmatrix} 0 & e^{i\phi} \\ e^{-i\phi} & 0 \end{pmatrix}. \tag{2.39}$$

Using that $e^{i\theta A} = \cos\theta \mathbb{1} + i \sin\theta A$ for a unitary matrix A, we can express the time-evolution operator for the effective Hamiltonian as[66]

$$U(t,\Omega,\varphi) = e^{-i\mathcal{H}_{\text{eff}}t} = \begin{pmatrix} \cos\left(\frac{\Omega}{2}t\right) & \sin\left(\frac{\Omega}{2}t\right)e^{i\varphi} \\ -\sin\left(\frac{\Omega}{2}t\right)e^{-i\varphi} & \cos\left(\frac{\Omega}{2}t\right) \end{pmatrix}, \tag{2.40}$$

where we have done a trivial phase shift setting $\varphi = \phi + \pi/2$. This time-evolution operator operates on state vectors in the rotating frame obtained by applying the unitary transformations U_1 and U_2, Eq. (2.35), to the state vector Eq. (2.29). However, since the state vectors only differ by unitary rotations, the populations ρ_{11} and ρ_{22} are the same in the rotating and stationary frame.

We immediately see that Eq. (2.40) agrees with our arguments above that a $\frac{\pi}{2}$-pulse of duration $t_{\pi/2} = \pi/2\Omega$ puts a system initially in the non-interacting state into an equal superposition of the non-interacting and the interacting state, while a π-pulse of duration $t_\pi = \pi/\Omega$ would put the system fully into the interacting state.

Finally, we note that a full turn on the Bloch sphere (a 2π-pulse) does not return to the original state, but introduces an overall phase $|1\rangle \xrightarrow{2\pi} -|1\rangle$, while we need two turns on the Bloch sphere to return to the original state $|1\rangle \xrightarrow{4\pi} |1\rangle$.

[66] M. A. Nielsen and I. L. Chuang. *Quantum Computation and Quantum Information*. Cambridge University Press, 2000.

Decoherence Due To Collisions

As mentioned at the beginning of this section, the state $|2\rangle$ interacts with the majority atoms and hence, the momentum states will be damped due to collisions between the impurity and the majority atoms, while the non-interacting state $|1\rangle$ is unaffected.[67] Starting with an impurity of momentum $\boldsymbol{p}_0$ in the interacting state $|2,\boldsymbol{p}_0\rangle$ the elastic scattering rate γ_{scat} causes the population of the state to decay at a rate γ_{scat} and the wave function amplitude of $|2,\boldsymbol{p}_0\rangle$ to decay at a rate $\gamma_{\text{scat}}/2$. Since the non-interacting state $|1,\boldsymbol{p}\rangle$ is not affected by collisions, the coherences $|2,\boldsymbol{p}\rangle\langle 1,\boldsymbol{p}|$ and $|1,\boldsymbol{p}\rangle\langle 2,\boldsymbol{p}|$ decay at a rate $\gamma_{\text{scat}}/2$ due to collisions, while collisions reshuffle the population of different momentum states of $|2,\boldsymbol{p}\rangle\langle 2,\boldsymbol{p}|$ at a rate γ_{scat} and $|1,\boldsymbol{p}\rangle\langle 1,\boldsymbol{p}|$ is unaffected by collisions. Finally, we also consider the possibility of direct decay of the $|2\rangle$ state into a third state outside our two level model of the atom. In practice this will be the decay of the repulsive polaron into a lower lying molecule state, where the minority atom pairs up with a majority atom. This direct decay of the $|2,\boldsymbol{p}\rangle$ state causes the population of the $|2,\boldsymbol{p}\rangle\langle 2,\boldsymbol{p}|$ to decay at a rate Γ, while the coherences $|2,\boldsymbol{p}\rangle\langle 1,\boldsymbol{p}|$ and $|1,\boldsymbol{p}\rangle\langle 2,\boldsymbol{p}|$ each decay at a rate $\Gamma/2$.[62]

Assuming that the Hamiltonian and the direct decay acts equally on all momentum states, we drop the momentum labels and introduce the decoherence to our equations "by hand"?[62]

$$\partial_t\langle\boldsymbol{\sigma}\rangle = -\Delta\,\hat{\boldsymbol{z}}\times\langle\boldsymbol{\sigma}\rangle + \Omega\,\boldsymbol{n}\times\langle\boldsymbol{\sigma}\rangle - \gamma_{\text{coh}}\begin{pmatrix}\langle\hat{\sigma}_x\rangle\\ \langle\hat{\sigma}_y\rangle\\ 0\end{pmatrix} - \frac{\Gamma}{2}\begin{pmatrix}0\\ 0\\ \langle\hat{\sigma}_z\rangle+1\end{pmatrix}, \tag{2.41}$$

where $\gamma_{\text{coh}} = (\Gamma+\gamma_{\text{scat}})/2$ and we have used that $\rho_{22} = (\langle\hat{\sigma}_z\rangle+1)/2$. This equation corresponds to the subtraction of $\gamma_{\text{coh}}\tilde{\rho}_{ij}$ for the off-diagonal terms and $\Gamma\rho_{22}$ for the upper left entry of Eq. (2.36), such

[67] M. Cetina et al. *Measurements of Polaron Coherence by Spin Echo* personal communication Feb. 17, 2014

that we end up with

$$\partial_t \tilde{\rho} = \begin{pmatrix} i\frac{\Omega}{2}\left(\tilde{\rho}_{21}e^{i\phi} - \tilde{\rho}_{12}e^{-i\phi}\right) - \Gamma\rho_{22} & -(\gamma_{\text{coh}} - i\Delta)\tilde{\rho}_{21} + i\frac{\Omega}{2}(\rho_{22} - \rho_{11})e^{-i\phi} \\ -(\gamma_{\text{coh}} + i\Delta)\tilde{\rho}_{12} - i\frac{\Omega}{2}(\rho_{22} - \rho_{11})e^{i\phi} & -i\frac{\Omega}{2}\left(\tilde{\rho}_{21}e^{i\phi} - \tilde{\rho}_{12}e^{-i\phi}\right) \end{pmatrix}.$$

That this density matrix yields Eq. (2.41) is easily verified by plugging it into Eq. (2.38). We see that the scattering term γ_{scat} do not enter in the diagonal terms, since we assume that collisions only reshuffle the population of momentum states and hence, do not affect the populations.

From Eq. (2.41) we see that the effect of collisions and the direct decay is to compress the Bloch vector in the xy-plane at a rate

$$T_2^{-1} = \gamma_{\text{coh}} = (\Gamma + \gamma_{\text{scat}})/2 \tag{2.42}$$

analogous to NMR-style damping of nuclear spins, and remove population from state $|2\rangle$ at a rate Γ.[62]

2.5 Radio Frequency Spectroscopy

In this section we go through the experimental technique of rf spectroscopy applied to measure e.g. the energy or internal decoherence of impurities in an ultracold gas.[56,62,67,68] As we will see rf spectroscopy directly probes the spectral function of the system, and the method is applicable to fermionic as well as bosonic systems, although care have to be taken when investigating a fermionic system due to the Pauli exclusion principle.[69] Thus, for a fermionic system we need to prepare a two component gas of either different internal states or different atomic species from the beginning. For a bosonic system we can start with a single component gas and then create impurities by flipping some of the atoms into a different internal state through a rf pulse.

We start our discussion of rf spectroscopy with a system, where an impurity atom of mass $m_\downarrow$ is situated in a single component ultracold gas of majority atoms with mass $m_\uparrow$ and total wave function

[68] G. M. Bruun *Ramsey and Spin Echo Spectroscopy and Many-Body Correlations* personal communication May 11, 2015

[69] M. W. Zwierlein et al. *Phys. Rev. Lett.*, **91**: 250404, 2003.

$|\Phi\rangle$. The impurity atom has a non-interacting $|1\rangle$ and an interacting $|2\rangle$ internal state with single particle energies E_1 and E_2 as shown in Fig. 2.3. Thus, when the impurity atom is in state $|1\rangle$ the system develops accordingly to the non-interacting Hamiltonian

$$\mathscr{H}_0 = \sum_p (\epsilon_p c_p^\dagger c_p + \varepsilon_p a_p^\dagger a_p), \tag{2.43}$$

where $c_p^\dagger$ ($a_p^\dagger$) creates an impurity (majority) atom with kinetic energy $\epsilon_p = p^2/2m_\downarrow$ ($\varepsilon_p = p^2/2m_\uparrow$). When the impurity is in state $|2\rangle$ the system develops according to the interacting Hamiltonian

$$\mathscr{H} = \mathscr{H}_0 + \frac{1}{\mathcal{V}} \sum_{p,p',q} V(\boldsymbol{q}) c_{p+q}^\dagger a_{p'-q}^\dagger a_{p'} c_p \tag{2.44}$$

with $V(\boldsymbol{q})$ being the interaction potential and $\mathcal{V}$ the volume of the system.

Measuring the Energy Shift of the Polaron

As discussed above and illustrated in Fig. 2.3, the energy level of the interacting $|2\rangle$ is shifted with E_{pol} when the impurity is emerged in a gas of majority atoms. Hence, by determining the energy difference between the states $|1\rangle$ and $|2\rangle$ with and without the majority gas present, we can determine the additional energy shift E_{pol} due to interactions with the majority gas.

Again, we stress that we use energy and frequency interchangeably with $\hbar = 1$. Experimentally, the energy difference between the two states can be determined by starting with the impurity atom in the non-interacting state and then applying a π-pulse transferring the non-interacting atoms into the interacting state. The population transfer is obviously maximal, when the π-pulse is resonant with the energy level splitting. Hence, by scanning a frequency range, we can determine the resonance frequency and thus, the energy level splitting between the states $|1\rangle$ and $|2\rangle$. Using a Feshbach resonance, we can measure the energy level splitting between states $|1\rangle$ and $|2\rangle$ with and without the majority atoms present (or in practice by

making the majority gas very dilute). The difference in the energy level splitting with and without the medium present is then the additional energy shift introduced by interactions and hence, the polaron energy as seen in Figs. 2.3 and 2.6.

In practice, we do not have a single impurity atom emerged in a majority gas, since this is experimentally impossible and the signal from a single atom would be completely absorbed by experimental noise. We briefly go through the experimental procedure of measuring the energy shift of the Bose polaron in the experiment discussed in Chapter 6. Here, we start with a Bose-Einstein condensate (BEC) of ^{39}K atoms. Since it is a Bose gas, we can start with a single species gas and then flip a fraction of the atoms into the interacting impurity state $|2\rangle$. A square rf pulse of length $100\,\mu$s is applied flipping atoms from state $|1\rangle$ to $|2\rangle$. The impurity atoms are then quickly lost through three-body recombination processes involving two atoms in state $|1\rangle$ and one atom in state $|2\rangle$.[44,70,71] Thus, flipping 10 % of the atoms into the interacting state results in a 30 % loss of atoms in total. The Rabi frequency Ω is adjusted through the intensity of the laser field in such a way, that the $100\,\mu$s rf pulse corresponds exactly to flipping 10 % of the atoms from state $|1\rangle$ to $|2\rangle$ at the resonance frequency as shown schematically in Fig. 2.7. A 10 % population transfer at resonance corresponds to $\Omega t \approx 0.64$ roughly corresponding to a $\frac{\pi}{5}$-pulse as seen in Fig. 2.5.[62] A frequency scan is then done in order to determine the resonance frequency and the width of the signal, similarly shown in Fig. 2.7. This procedure is repeated and applied for all interaction strengths, and the 10 % population transfer ensures that the signal is normalized in the same way for all interaction strengths.

Measuring the Scattering Rate of the Polaron

The scattering rate of a polaron, can be measured by determining the decoherence rate γ_{coh} as discussed in the end of Section 2.4. The scattering rate γ_{scat} is related to the decoherence rate through Eq. (2.42):

[70] B. D. Esry et al. *Phys. Rev. Lett.*, **83**: 1751–1754, 1999.
[71] E. Nielsen and J. H. Macek. *Phys. Rev. Lett.*, **83**: 1566–1569, 1999.

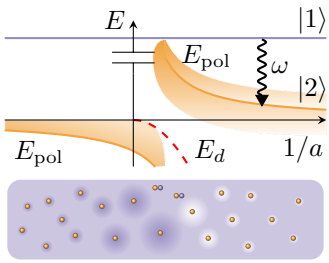

Figure 2.6: Sketch of the spectroscopic method used for determining the energy of a polaron. The solid lines are the polaron energy E_{pol} as a function of the inverse scattering length $1/a$, whereas the shaded areas are a continuum of different excitations. The dashed line show the dimer energy of the bound state E_d. The bottom cartoon show impurity atoms (orange) emerged in a majority gas (purple). The intensity of the background color indicates the change in the majority density due to the presence of impurity atoms.

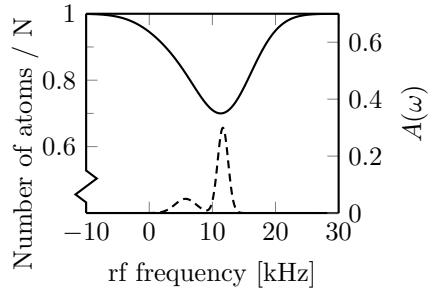

Figure 2.7: Sketch of a frequency scan with rf spectroscopy. The dashed line is the polaron's spectral function, whereas the full line is the number of atoms observed. N is the number of atoms initially in the BEC. Here, the rf pulse is a square pulse of duration 100 μs, and the pulse intensity is chosen such that the peak loss is 30 % of the atoms initially in the BEC.

$\gamma_{\text{coh}} = (\Gamma + \gamma_{\text{scat}})/2$. Ideally, the decoherence rate can be determined by applying Ramsey spectroscopy on a single impurity emerged in a majority gas. As before, we model the impurity atom as a two level atom with the general internal state vector $|\psi\rangle = c_1|1\rangle + c_2|2\rangle$, where we remember that the non-interacting state $|1\rangle$ develops according to the non-interacting Hamiltonian Eq. (2.43), while the interacting state $|2\rangle$ develops according to the interacting Hamiltonian Eq. (2.44). We quantify the full state of the system with a single impurity in momentum state $\boldsymbol{p}$ emerged in a majority gas by $|\Psi\rangle = |\psi\rangle \otimes c_{\boldsymbol{p}}^\dagger|\Phi\rangle$. With the impurity atom initially in the non-interacting $|1\rangle$, the Ramsey sequence then consists of four steps:[68]

1. Rotate the internal state by a $\frac{\pi}{2}$-pulse with phase φ_0. By inserting $\Omega t = \pi/2$ into Eq. (2.40) and multiplying it onto the initial state $\binom{0}{1}$, we obtain the state

$$|\Psi\rangle = \frac{1}{\sqrt{2}}\big(|1\rangle + e^{i\varphi_0}|2\rangle\big) \otimes c_p^\dagger |\Phi\rangle\,. \tag{2.45}$$

2. Letting the state evolve for a time t, we obtain

$$|\Psi\rangle = \frac{1}{\sqrt{2}}\big(e^{-i(E_1+\mathscr{H}_0)t}|1\rangle + e^{i\varphi_0}e^{-i(E_2+\mathscr{H})t}|2\rangle\big) \otimes c_p^\dagger |\Phi\rangle\,. \tag{2.46}$$

3. Then we apply a second $\frac{\pi}{2}$-pulse with phase φ_1:

$$\begin{aligned}|\Psi\rangle = \frac{1}{2}\big(e^{-i(E_1+\mathscr{H}_0)t} - e^{i(\varphi_0-\varphi_1)}e^{-i(E_2+\mathscr{H})t}\big)|1\rangle \otimes c_p^\dagger|\Phi\rangle \\ + \frac{1}{2}\big(e^{i\varphi_1}e^{-i(E_1+\mathscr{H}_0)t} + e^{i\varphi_0}e^{-i(E_2+\mathscr{H})t}\big)|2\rangle \otimes c_p^\dagger|\Phi\rangle\,.\end{aligned} \tag{2.47}$$

4. Finally, we measure $S_z = \langle\hat{\sigma}_z\rangle = (N_2 - N_1)/N$, where $N = N_1 + N_2$ and N_i is the population of the ith-state.

We then obtain

$$\begin{aligned}S_z &= \langle\Psi|\hat{\sigma}_z|\Psi\rangle = \frac{1}{N}\big(|\langle\Psi|2\rangle|^2 - |\langle\Psi|1\rangle|^2\big) \\ &= \mathfrak{Re}\big[e^{i(\varphi_0-\varphi_1)}e^{-i(E_2-E_1)t}\langle\Phi|c_p e^{-i(\mathscr{H}-\mathscr{H}_0)t}c_p^\dagger|\Phi\rangle \\ &= \mathfrak{Re}\big[e^{i\phi}S(t)\big],\end{aligned} \tag{2.48}$$

where we have used that $c_p e^{i\mathscr{H}_0 t} = e^{i\epsilon_p t}e^{i\mathscr{H}_0 t}c_p$ and introduced

$$\phi = (E_1 - E_2 + \epsilon_p)t + \varphi_0 - \varphi_1 \tag{2.49}$$

and

$$S(t) = \langle\Phi|c_p(t)c_p^\dagger(0)|\Phi\rangle \tag{2.50}$$

with $c_p(t) = e^{i\mathscr{H}t} c_p e^{-i\mathscr{H}t}$.

At low temperatures, we can ignore ϵ_p with respect to the energy level splitting $E_1 - E_2$ making the phase ϕ independent of the impurity's momentum. We see that the correlation function $S(t)$ can be directly related to the real time Green's function for an impurity on top of the state $|\Phi\rangle$. Furthermore, we can extract the amplitude and phase of $S(t)$ by measuring S_z as a function of ϕ at a given wait time t in step 2 above. For instance, we see that at $t = 0$ we have $S(0) = 1$ and $S_z(\phi) = \cos\phi$.

For $t > 0$ the impurity interacts and collides with the majority atoms during the waiting time randomising their phases leading to decoherence of the impurity as discussed in Section 2.4.

Defining $s_{z,\max}(t)$ $\left(s_{z,\min}(t)\right)$ as the maximum (minimum) of the $S_z(\phi)$ curve at a given waiting time t, the decay of the contrast $C(t) = \left(s_{z,\max}(t) - s_{z,\min}(t)\right)/2$ can be shown to relate to the decoherence rate γ_{coh} through[67]

$$C(t) = \frac{s_{z,\max}(t) - s_{z,\min}(t)}{2} \propto e^{-\gamma_{\text{coh}} t}. \tag{2.51}$$

Hence, since $C(t)$ essentially measures the amplitude of the correlation function $S(t)$, the decoherence rate is related to an amplitude decay of the correlation function $S(t)$. For a waiting $t = 0$ the system is fully coherent and $S_z(\phi) = \cos\phi$ corresponding to a contrast of $C = 1$, while for very long waiting times where the system is fully decohered $S_z(\phi) = 0$ corresponding to $C = 0$. By measuring the contrast $C(t)$as a function of the waiting time it is then possible to determine the decoherence rate γ_{coh} by fitting a curve of the form $Ae^{-\gamma_{\text{coh}} t}$ to $C(t)$ and then relating this to the impurity scattering rate through Eq. (2.42). Another way of understanding this amplitude decay is by relating the correlation function $S(t)$ to the spectral function of the impurity, as we will do below.

Relationship to the spectral function

As seen from Eqs. (2.48) and (2.50) the signal obtained from the Ramsey sequence is directly related to the real time Green's function

of the polaron. We see from Eq. (2.24) that by doing a Fourier transform on a real time Green's function given by $G(t) = A_0 e^{-i\phi t} e^{-t/2\tau}$, we obtain a Lorentzian spectral function

$$A(\omega) = A_0 \frac{1/\tau_p}{(\omega - \phi)^2 + (1/2\tau)^2}. \tag{2.52}$$

Hence, as we know from our discussion in Section 2.3, we associate a Lorentzian spectral function with a decaying particle of lifetime τ. Neglecting for a moment the direct decay to the molecular state Γ, we have assumed that the lifetime of our polaron state is given by $\tau = 1/\gamma_{\text{scat}}$. Hence, the associated real time Green's function corresponding to the correlation function $S(t)$ will decay at a rate $e^{-t/2\tau} = e^{-t/2\gamma_{\text{scat}}} = e^{-t/\gamma_{\text{coh}}}$, where we have used that $\gamma_{\text{coh}} = \gamma_{\text{scat}}/2$.

For completeness, we also show the correlation function associated with a δ-function spectral function $A(\omega) = 2\pi\delta(\omega - E_{\text{pol}})$:

$$\begin{aligned} S(t) &= \frac{1}{2\pi} \int_{-\infty}^{\infty} \mathrm{d}\omega \, e^{-i\omega t} 2\pi\delta(\omega - E_{\text{pol}}) \\ &= e^{-iE_{\text{pol}}t}. \end{aligned} \tag{2.53}$$

Thus, a δ-function spectral function merely translates into a rotating phase of the observed correlation function.

Summarising, we see the underlying spectral function determines the behaviour of the measured correlation function $S(t)$ and equivalently, that the underlying spectral function can be determined through an inverse Fourier transformation of the observed correlation function.[72,73]

Ramsey sequence in terms of the Bloch vector

In terms of the Bloch vector, we see that the four steps of the Ramsey sequence corresponds to:

1. The Bloch vector initially of length 1 and pointing to the south pole of the Bloch sphere is rotated by a $\frac{\pi}{2}$-pulse with phase

[72] A. D. Cronin et al. *Rev. Mod. Phys.*, **81**: 1051–1129, 2009.
[73] M. Knap et al. *Phys. Rev. X*, **2**: 041020, 2012.

φ_0 around the vector $\boldsymbol{n} = (\cos\varphi_0, \sin\varphi_0, 0)$. Thus, the Bloch vector ends up at the equator with an azimuthal angle of φ_0.

2. The Bloch vector evolves around the equator for a waiting time t according to the relative phase $e^{-i(E_2-E_1+\mathscr{H}-\mathscr{H}_0)t}$. During this waiting time collisions decohere the system at a rate γ_{coh}, such that the Bloch vector shortens as $\propto e^{-\gamma_{\text{coh}}t}$.

3. The Bloch vector is rotated by a $\frac{\pi}{2}$-pulse with phase φ_1 around the vector $\boldsymbol{n} = (\cos\varphi_1, \sin\varphi_1, 0)$. Depending on the total phase $\phi = (E_1 - E_2 + \epsilon_p)t + \varphi_0 - \varphi_1$, the Bloch vector can end up pointing along all directions yielding the variation of S_z as a function of ϕ.

4. A measurement of $\langle\hat{\sigma}_z\rangle$ is made corresponding to a projection of the Bloch vector onto the z-axis.

We stress that varying ϕ between 0 and 2π, for instance by varying the relative phase of the two $\frac{\pi}{2}$-pulses $\varphi_0 - \varphi_1$, ensures that $S_z(\phi)$ goes through its maximum and minimum values such that the contrast can be determined.

Spin-Echo Method

As seen from Eq. (2.49) the phase entering S_z in Eq. (2.48) depends on the energy level splitting $E_1 - E_2$. This is a problem experimentally, where the atoms are confined in a trap and thus not homogeneous, since the energy of the interacting state E_2 depends on the local density of the majority atoms. Thus individual impurity atoms sitting at different places in the trap will evolve with different phases during the waiting time. An elegant way of making the Ramsey sequence independent of the energy splitting $E_1 - E_2$ and hence the local density, is the introduction of an "echo"- or π-pulse in the middle of the waiting time. Hence, by introducing an extra π-pulse in the middle of waiting time, the spin-echo method have six steps:

1. As before: Rotate the initial state $|1\rangle$ by a $\frac{\pi}{2}$-pulse with phase φ_0.

2. Let the state evolve for a time $t/2$.
3. Rotate the state by a π-pulse with phase 0 and rotation matrix $\left(\begin{smallmatrix} 0 & 1 \\ -1 & 0 \end{smallmatrix}\right)$.
4. Let the state evolve for a time $t/2$.
5. As before: Rotate the state by a $\frac{\pi}{2}$-pulse with phase φ_1.
6. Measurement of S_z.

Going through steps analogously to what was done above, we end up with

$$S_z = -\mathfrak{Re}\Big[e^{i(\varphi_0+\varphi_1)} \langle \Phi | c_p e^{i(\mathscr{H}_0+\mathscr{H})t} e^{-i(\mathscr{H}_0+\mathscr{H})t} c_p^\dagger | \Phi \rangle \,. \tag{2.54}$$

Thus, we end up with a signal independent of the internal energy levels E_1 and E_2 and hence less sensitive to local density variations or fluctuations in the external magnetic field. It is however not possible to directly relate Eq. (2.54) to a single Green's function as Eq. (2.48), since the interaction is turned on and off multiple times.

In terms of the Bloch sphere, the problem with the Ramsey sequence is that due to variations of the internal levels between different impurity atoms, we do not have a single Bloch vector propagating around the z-axis after the first $\frac{\pi}{2}$-pulse. Rather, we have individual Bloch vectors for each of the impurity atoms all rotating with different speeds around the z-axis according to the local relative phase $e^{-i(E_2-E_1+\mathscr{H}-\mathscr{H}_0)t}$. The echo-pulse in the middle of the waiting time t mirrors the Bloch vectors through the plane spanned by the $\hat{z}$ and $\boldsymbol{n} = \hat{x}$ vectors, ensuring that the varying local phases due to the energy levels during the first half of the waiting and the second part of the waiting time cancel each other. Hence, an individual Bloch vector propagates as much "backward" after the π-pulse as it propagated "forward" before the π-pulse due to energy splitting $E_1 - E_2$.[74,75] Two nice illustrations of the spin-echo method with and without decoherence can be seen in Ref. [74, 75].

[74] G. W. Morley available online at `https://commons.wikimedia.org/wiki/File:GWM_HahnEchoDecay.gif`

[75] G. W. Morley available online at `https://commons.wikimedia.org/wiki/File:GWM_HahnEcho.gif`

The spin-echo method is used when experimentally determining the decoherence rate.

CHAPTER

3 Scattering Rate of the Fermi Polaron

This and the following chapter builds on work published in Refs. [52, 53] discussing the scattering rate of a quasiparticle in a Fermi gas, the Fermi polaron.This chapter discusses the theoretical work done on an ideal system with a single impurity atom emerged in a Fermi gas of majority atoms while the following chapter discusses the theoretical modelling of an experiment done at IQOQI in Innsbruck by the group of R. Grimm.[52,53] A large part of the theory discussing the Boltzmann transport equation and deriving the effective $\mathcal{T}$-matrix was done in my Master's thesis.[76] Hence, we cite the thesis accordingly and do not discuss the theory in detail here.

Impurities in a Fermi sea have been realised in a range of experiments and a rather simple and intuitive theory modelling the impurity as a quasiparticle within Fermi liquid theory has succeeded in describing the zero-momentum properties of this Fermi polaron, even for large coupling strengths using the $\mathcal{T}$-matrix in the ladder

[52]R. S. Christensen and G. M. Bruun. *Phys. Rev. A*, **91**: 042702, 2015.

[53]M. Cetina et al. *Phys. Rev. Lett.*, **115**: 135302, 2015.

[76]R. S. Christensen. *Collision Rate of Polarons*. Master's Thesis. Aarhus University, Aug. 2013.

approximation.[41–43,47,48,53,77–80] A range of studies have also investigated the finite lifetime of a Fermi polaron with non-zero momentum, but these are all limited by either weak coupling, zero or very low temperature, high momentum or performed exactly at unitarity.[81–86]

We model the scattering rate of the Fermi polaron through a non-perturbative approach to include strong interactions as well as finite temperature. We employ a semi-classical approach, where we model the scattering rate through the semi-classical Boltzmann transport equation (BTE), rather than the quasiparticle approach described in the previous chapter, but use the correct quantum mechanical cross-section through our $\mathcal{T}$-matrix approach. Hence, since BTE considers scattering of well-defined particles, we need the quasiparticle residue to be close to 1 for this approach to be valid. This limits our discussion to $|k_F a| \lesssim 1$ with k_F the Fermi momentum of the majority atoms and a the impurity-majority scattering length.[42,48,53]

Throughout this discussion we denote the impurity atom by spin-$\downarrow$ and the majority atoms by spin-$\uparrow$. Furthermore, we interchangeably use the terms scattering rate and lifetime for the inverse scattering rate.

[41] A. Schirotzek et al. *Phys. Rev. Lett.*, **102**: 230402, 2009.
[42] C. Kohstall et al. *Nature*, **485**: 615–618, 2012.
[43] M. Koschorreck et al. *Nature*, **485**: 619–622, 2012.
[47] F. Chevy. *Phys. Rev. A*, **74**: 063628, 2006.
[48] P. Massignan et al. *Rep. Prog. Phys.*, **77**: 034401, 2014.
[77] C. Lobo et al. *Phys. Rev. Lett.*, **97**: 200403, 2006.
[78] M. Punk et al. *Phys. Rev. A*, **80**: 053605, 2009.
[79] N. Prokof'ev and B. Svistunov. *Phys. Rev. B*, **77**: 020408, 2008.
[80] C. J. M. Mathy et al. *Phys. Rev. Lett.*, **106**: 166404, 2011.
[81] G. M. Bruun et al. *Phys. Rev. Lett.*, **100**: 240406, 2008.
[82] C. Trefzger and Y. Castin. *EPL*, **104**: 50005, 2013.
[83] C. Trefzger and Y. Castin. *Phys. Rev. A*, **90**: 033619, 2014.
[84] Z. Lan et al. *Phys. Rev. Lett.*, **111**: 145301, 2013.
[85] J. J. Kinnunen. *Phys. Rev. A*, **85**: 012701, 2012.
[86] Y. Nishida. *Phys. Rev. A*, **85**: 053643, 2012.

3.1 Scattering Rate From BTE And $\mathcal{T}$-matrix

From Fermi liquid theory the scattering rate of a quasiparticle with momentum $\boldsymbol{p}$ with the surrounding medium is[35,55,59,76]

$$\frac{1}{\tau_p} = \int \frac{\mathrm{d}^3 p_2}{(2\pi)^3} \frac{m_r p_r}{(2\pi)^3} \int \mathrm{d}\Omega W(12;34)[f_{2\uparrow}(1-f_{3\downarrow}-f_{4\uparrow})+f_{3\downarrow}f_{4\uparrow}], \quad (3.1)$$

which comes from linearising the collision integral in Boltzmann transport equation:

$$I_{\mathrm{coll}} = \int \frac{\mathrm{d}^3 p_2}{(2\pi)^3} \frac{\mathrm{d}^3 p_3}{(2\pi)^3} W(12;34)\delta(\epsilon_1+\epsilon_2-\epsilon_3-\epsilon_4) \times [f_{1\downarrow}f_{2\uparrow}(1-f_{3\downarrow})(1-f_{4\uparrow})-f_{3\downarrow}f_{4\uparrow}(1-f_{1\downarrow})(1-f_{2\uparrow})]. \quad (3.2)$$

Here, $W(12;34) = 2\pi^2\sigma/m_r^2$ is the transition probability for the scattering of impurity and majority atoms with momenta $\boldsymbol{p}_1$ and $\boldsymbol{p}_2$ respectively, to momenta $\boldsymbol{p}_3$ and $\boldsymbol{p}_4$ as seen in Fig. 3.1. σ is the scattering cross section, $m_r = m_\downarrow m_\uparrow/(m_\downarrow+m_\uparrow)$ is the reduced mass of the system, $\boldsymbol{p}_4 = \boldsymbol{p}_1+\boldsymbol{p}_2-\boldsymbol{p}_3$. Ω is the solid angle for the directions of the incoming relative momentum $\boldsymbol{p}_r = (m_\uparrow \boldsymbol{p}_1 - m_\downarrow \boldsymbol{p}_2)/M$ with respect to the outgoing relative momentum $\boldsymbol{p}_r' = (m_\uparrow \boldsymbol{p}_3 - m_\downarrow \boldsymbol{p}_4)/M$ with $M = m_\downarrow + m_\uparrow$ being the total mass. The Fermi distribution function is $f_{p\sigma} = [e^{\beta(\epsilon_{p\sigma}-\mu_\sigma)}+1]^{-1}$ with μ_σ the chemical potential of the σ-atoms, $\beta = 1/T$ and $\epsilon_{p\sigma} = p^2/2m_\sigma$. In the limit of a single impurity atom $\mu_\downarrow \to -\infty$, Eq. (3.1) reduces to

$$\frac{1}{\tau_p} = \int \frac{\mathrm{d}^3 p_2}{(2\pi)^3} \frac{m_r p_r}{(2\pi)^3} \int \mathrm{d}\Omega W(12;34) f_{2\uparrow}(1-f_{4\uparrow}). \quad (3.3)$$

[35] G. Baym and C. Pethick. *Landau Fermi-Liquid Theory: Concepts and Applications*. Wiley, 1991.

[55] C. Pethick and H. Smith. *Bose-Einstein Condensation in Dilute Gases*. Cambridge University Press, 2002.

[59] H. Bruus and K. Flensberg. *Many-Body Quantum Theory in Condensed Matter Physics: An Introduction*. Oxford University Press, 2004.

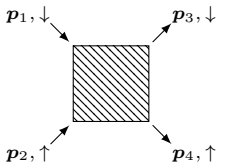

Figure 3.1: Sketch of a scattering event, where two particles of momentum p_1 and p_2 scatters of each other and ends up with momentum p_3 and p_4. For this event we have centre of mass momentum $P = p_1 + p_2 = p_3 + p_4$, incoming relative momentum $p_r = (m_\uparrow p_1 - m_\downarrow p_2)/M$, and outgoing relative momentum $p_r' = (m_\uparrow p_3 - m_\downarrow p_4)/M$.

In the following we will discuss two systems: An equal mass $m_\downarrow = m_\uparrow$ system with a broad Feshbach resonance, where the $\mathcal{T}$-matrix is given by Eq. (2.7), and the experimentally relevant system of a ^{40}K impurity immersed in a Fermi sea of ^{6}Li atoms interacting through a narrow Feshbach resonance corresponding to the setup of R. Grimm's group at IQOQI in Innsbruck.[53] An effective Hamiltonian for the experimentally relevant ^{40}K-^{6}Li system is given by

$$\mathscr{H} = \sum_{p,\sigma} \xi_{p\sigma} c_{p\sigma}^\dagger c_{p\sigma} + \frac{g_o}{\mathcal{V}} \sum_{p,p',q} c_{p+q\downarrow}^\dagger c_{p'-q\uparrow}^\dagger c_{p'\downarrow} c_{p\uparrow} + \sum_{p,\sigma} E_p b_p^\dagger b_p + \frac{g_c}{\sqrt{\mathcal{V}}} \sum_{p,p'} \left[b_P^\dagger c_{p\downarrow} c_{p'\uparrow} + b_P c_{p\downarrow}^\dagger c_{p'\uparrow}^\dagger \right], \quad (3.4)$$

where $P = p + p'$, $\xi_{p\sigma} = p^2/2m_\sigma - \mu_\sigma$ ($E_p = p^2/2M$) is the kinetic energy of a spin-σ atom (dimer), $c_{p\sigma}^\dagger (b_p^\dagger)$ is the creation operator for a spin-σ (dimer) with momentum p and g_o (g_c) is the pseudopotential associated with an open (closed) scattering channel as discussed in Section 2.1. Hence, the two new terms not included in the effective Hamiltonian for the broad Feshbach resonance, Eq. (2.2) are the possibility of scattering into and out of a dimer state as well as a kinetic energy term for this dimer state.

Starting from this Hamiltonian, we can derive a $\mathcal{T}$-matrix for a narrow Feshbach resonance, again in the ladder approximation.

This $\mathcal{T}$-matrix is given by[76,87]

$$\mathcal{T}(\boldsymbol{P},\omega)=\frac{2\pi a/m_r}{\frac{p_r^2 r_{\rm eff}(a-a_{\rm bg})/2-1}{p_r^2 r_{\rm eff}a_{\rm bg}(1-a_{\rm bg}/a)/2-1}-\frac{2\pi a}{m_r}\Pi(\boldsymbol{P},\omega)}, \tag{3.5}$$

where $r_{\rm eff}=-(m_r a_{\rm bg}\delta\mu\Delta B)^{-1}$ and $a_{\rm bg}$ is the background scattering length as introduced in Section 2.1, and we have performed analytic continuation: $i\Omega\to\omega+i\eta$ on the pair-propagator Eq. (2.8). We immediately see that this $\mathcal{T}$-matrix reduces to the $\mathcal{T}$-matrix for a broad resonance Eq. (2.7) for $r_{\rm eff}\to 0$.

For reference we note that in the vacuum limit of two atoms scattering without any medium present, the pair-propagator can be evaluated analytically yielding

$$\begin{aligned}\Pi_v(\boldsymbol{P},\omega)&=\int\frac{\mathrm{d}^3q}{(2\pi)^3}\left[\frac{1}{\omega-\epsilon_{q\downarrow}-\epsilon_{\boldsymbol{P}-q\uparrow}+i\eta}-\frac{2m_r}{q^2}\right]\\&=-i\frac{m_r^{3/2}}{\sqrt{2}\pi}\sqrt{\omega-\frac{P^2}{2M}}\end{aligned} \tag{3.6}$$

with ω measured relative to the chemical potential of the impurity and majority atoms. Using the vacuum pair-propagator and assuming a broad resonance, we obtain the simple well-known expression for the $\mathcal{T}$-matrix of a broad Feshbach resonance[55]

$$\mathcal{T}_v(P,\omega)=\frac{2\pi a/m_r}{1+ia\sqrt{2m_r\left(\omega-\frac{P^2}{2M}\right)}}. \tag{3.7}$$

3.2 Cross Section

We now turn to a discussion of the cross section for the scattering rate of the Fermi polaron. The scattering cross section relates to the $\mathcal{T}$-matrix through $\sigma=m_r^2|\mathcal{T}|^2/\pi$. We map out the cross section in energy and momentum space in order to understand which scattering events dominates the scattering rate for a single Fermi polaron Eq. (3.3).

[87] G. M. Bruun et al. *Phys. Rev. A*, **71**: 052713, 2005.

In Fig. 3.2 we show the cross section for zero centre of mass momentum $\boldsymbol{P} = 0$ at a very low temperature $T = 0.01\, T_{\mathrm{F}}$ with $T_{\mathrm{F}} = \epsilon_{\mathrm{F}} = k_{\mathrm{F}}^2/2m_{\uparrow}$ being the Fermi energy and k_{F} the Fermi momentum of the majority $\uparrow$-atoms. In the figure zero energy corresponds to the bottom of the Fermi sea for the majority atoms, and we show the cross section as function of total energy and the inverse scattering length in 6 different cases: The 3 figures to the left are all for a broad Feshbach resonance $r_{\mathrm{eff}} = 0$, while the 3 to the right show a narrow resonance $k_{\mathrm{F}} r_{\mathrm{eff}} = -1.8$ corresponding to effective range in Ref. [53]. In the 3 rows of figures, we have respectively vacuum conditions $f_{\uparrow} \to 0$ and equal mass $m_{\downarrow} = m_{\uparrow}$ (top row), including medium effects and equal mass $m_{\downarrow} = m_{\uparrow}$ (middle row) and including medium effects and different masses $m_{\downarrow}/m_{\uparrow} = 40/6$ (bottom row). We also show the energy of the dimer in vacuum[48]

$$E_d = -\frac{1}{2m_r a_*^2}, \qquad a_* = -\frac{r_{\mathrm{eff}}}{\sqrt{1 - 2r_{\mathrm{eff}}/a} - 1} \tag{3.8}$$

which reduces to the usual dimer energy $E_d = -1/2m_r a^2$ for a broad resonance.

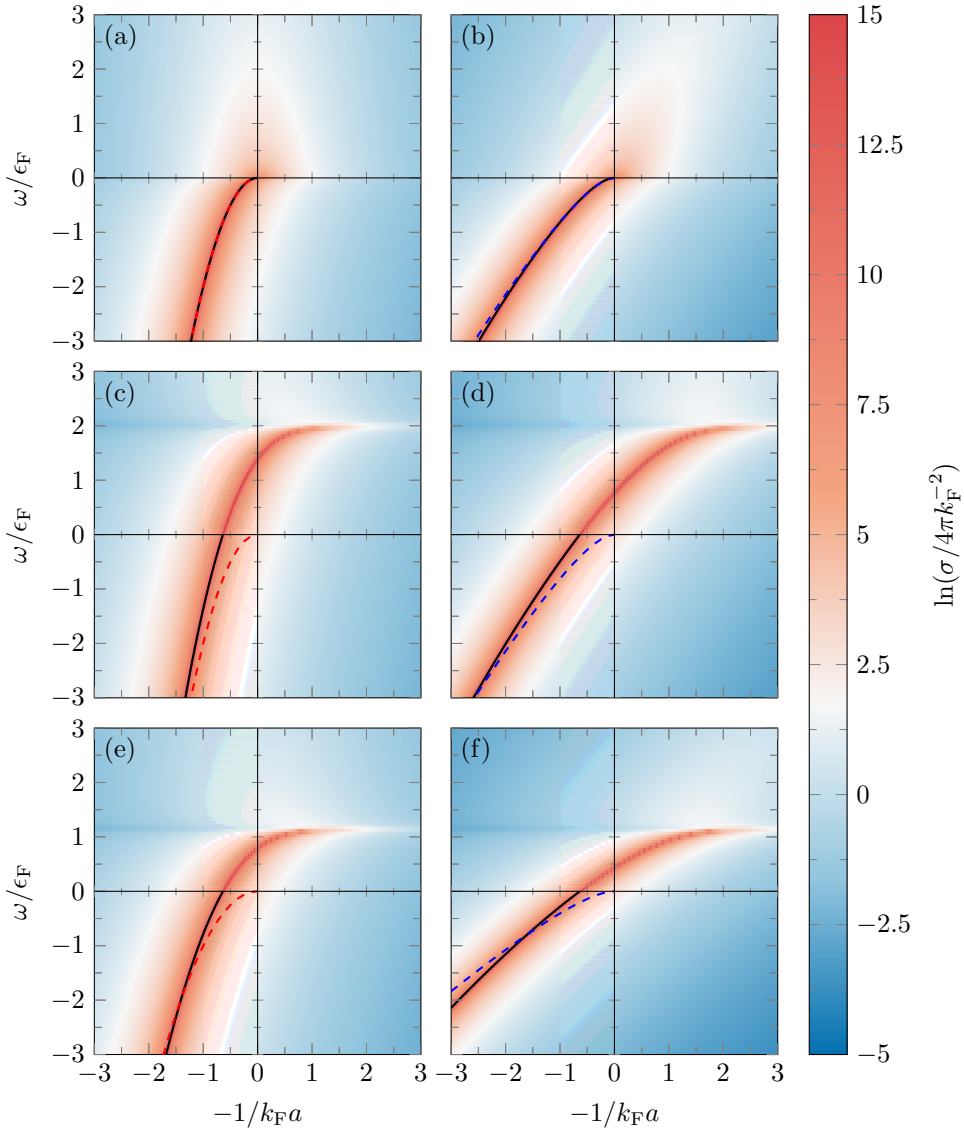

Figure 3.2: The cross section σ for $\boldsymbol{P} = 0$, $T = 0.01\,T_F$, and (a) $k_F r_{eff} = 0$, $m_\uparrow/m_\downarrow = 1$, (b) $k_F r_{eff} = -1.8$, $m_\uparrow/m_\downarrow = 1$, (c) $k_F r_{eff} = 0$, $m_\uparrow/m_\downarrow = 1$, (d) $k_F r_{eff} = -1.8$, $m_\uparrow/m_\downarrow = 1$, (e) $k_F r_{eff} = 0$, $m_\uparrow/m_\downarrow = 6/40$, (f) $k_F r_{eff} = -1.8$, $m_\uparrow/m_\downarrow = 6/40$. All figures except (a) and (b) include medium effects. The dashed lines is the vacuum dimer energy given by Eq. (3.8), while the full lines are the actual dimer energy obtained from the cross section.

In Figs. 3.2(a-b) we see the vacuum cross section in an equal mass system for respectively a broad and a narrow resonance. First off, we note that the two cross sections behave qualitatively in the same way and that we clearly see the dimer pole originating at the origin and coming down on the BEC side ($a > 0$) as expected from Eq. (3.8).

In the middle row Figs. 3.2(c-d) we see that introducing medium effects shifts the dimer pole upwards, and that it transforms into a resonance at positive energies acquiring a finite imaginary part, as the dimer can dissociate into two atoms with opposite momenta for $\omega > 0$ and $T > 0$. For $T = 0$ the dimer would be stable up to $\omega = 2\epsilon_F$, since Fermi blocking prohibits dissociation for $\omega \leq 2\epsilon_F$. In fact, it is straightforward to obtain the imaginary part of the pair-propagator describing the decay of the dimer to

$$\Im\mathrm{m}[\Pi(P=0,\omega)] = -\frac{m_r}{2\pi}\sqrt{2m_r\omega}[1-f_\uparrow(2m_r\omega)]. \tag{3.9}$$

Finally, in the bottom row Figs. 3.2(e-f) we introduce the experimentally relevant mass difference $m_\downarrow/m_\uparrow = 40/6$ along with the medium effects. We again note that the qualitative behaviour of the cross section does not change, but the position of the resonance on the BCS side ($a < 0$) is shifted down from $\omega \simeq 2\epsilon_F$ to $\omega \simeq (1 + m_\uparrow/m_\downarrow)\epsilon_F$.

In the BCS limit $k_F a \to 0_-$ the resonance seen in Figs. 3.2(c-f) is located at $\omega = p_r^2/2m_r = (1 + m_\uparrow/m_\downarrow)\epsilon_F$, since it corresponds to pairing between states on opposite states of the Fermi surface with zero centre-of-mass momentum. Hence, the resonance is the polaron analogue of Cooper pairing in a population balanced system with $n_\downarrow = n_\uparrow$. We stress that contrary to the balanced system, where there is a real and undamped pole below the critical temperature for Cooper pairing located at $\omega = (1 + m_\uparrow/m_\downarrow)\epsilon_F$, there is no true pole in the BCS regime for the polaron case due to the strong population imbalance. Importantly, we see from Fig. 3.2 that the cross section for the scattering of a polaron is significantly increased in the vicinity of the Cooper resonance. Thus, when including medium effects we expect an increase in the polaron scattering rate, since we include the possibility of resonantly scattering through a Cooper pair.

In Fig. 3.3 we show the behaviour of the cross section for increasing temperature. We show the cross section for a system with equal

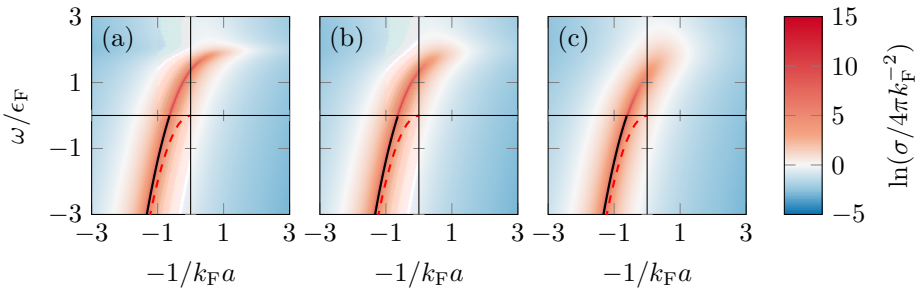

Figure 3.3: The cross section σ for $\boldsymbol{P} = 0$, $k_F r_{\text{eff}} = 0$, $m_\uparrow = m_\downarrow$ and (a) $T = 0.05\,T_F$, (b) $T = 0.10\,T_F$, and (c) $T = 0.20\,T_F$. The dashed line is the dimer energy given by Eq. (3.8).

mass and a broad Feshbach resonance, but the qualitative behaviour is the same for a mass imbalanced system with a narrow resonance. We see from the figure that medium effects are most important for low temperatures $T \ll \epsilon_F$, while the resonance becomes broader and weaker for increasing temperature. As we would expect, medium effects eventually vanish for high temperatures and the cross section reduces to the vacuum value $\sigma_v = m_r^2|\mathcal{T}_v|^2/\pi$ for $T \gg \epsilon_F$ (not shown).

When we determine the polarons scattering rate, we plug in the on-shell energy $\omega = P^2/2M + p_r^2/2m_r$, such that the cross section is given by $\sigma(\boldsymbol{P}, P^2/2M + p_r^2/2m_r) = m_r^2|\mathcal{T}(\boldsymbol{P}, P^2/2M + p_r^2/2m_r)|^2/\pi$. Hence, we enter the cross section shown in Fig. 3.2 with positive energies. Entering wit the on-shell energy we show in Fig. 3.4 the cross section at $k_F a = \pm 1$ as a function of the centre of mass and relative momenta. We show the cross section in units of the vacuum cross section σ_v in order to highlight where medium effects increase the cross section and hence the scattering rate of the polaron.

First off, we see that the cross section is drastically enhanced for $p_r \lesssim k_F$ and $P \simeq 0$ on the BCS side. This is consistent with the interpretation of the resonance in Fig. 3.2 as pairing of momenta opposite of the Fermi surface and hence, a reminiscent of Cooper pairing. In the BCS limit $k_F a \to 0_-$ the Cooper resonance is located at $p_r = k_F$ and $P = 0$. On the BEC side the cross section is enhanced

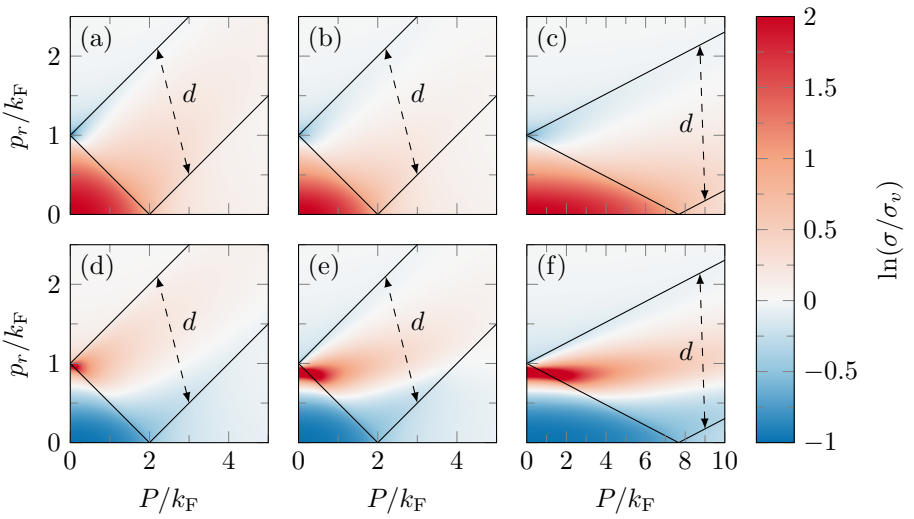

Figure 3.4: The cross section $\sigma(\boldsymbol{P}, P^2/2M + p_r^2/2m_r)$ relative to the vacuum cross section σ_v at $T = 0.01\,T_F$ and for $k_F a = 1$ ($k_F a = -1$) in the top (bottom) row, and (a,d) $k_F r_{eff} = 0$ and $m_\downarrow/m_\uparrow = 1$, (b,e) $k_F r_{eff} = -1.8$ and $m_\downarrow/m_\uparrow = 1$, and (c,f) $k_F r_{eff} = -1.8$ and $m_\downarrow/m_\uparrow = 6/40$. The area between the lines with a width d is the integration area for a polaron of momentum k_F. (Note that the drawn dashed line is at right angles with the solid lines, but the axes are not evenly scaled.)

at small momenta corresponding to small energies, as we would expect from inspecting Fig. 3.2 at $k_F a = -1$. Furthermore, we see again that introducing a narrow Feshbach resonance and mass imbalance only changes the quantitative behaviour along a single row in Fig. 3.4.

This quantitative change is however important, when calculating the scattering rate of the polaron as we will see in in the following section, and when we model the observed decoherence rate of Ref. [53] in Chapter 4. We can immediately see why this quantitative change is important by studying the integration region of Eq. (3.3) for the scattering rate of a polaron. If the momentum of the incoming polaron is p, the integration region for Eq. (3.3) is the area between the two lines $p_r = \frac{m_\downarrow}{M} P + p$ and $p_r = \frac{m_\downarrow}{M} P - p$ and above the line connecting the two points $(P = 0, p_r = p)$ and $(P = 2p, p_r = 0)$. We

show this integration area for $p = k_F$ in Fig. 3.4. The width of the integration area is

$$d = \frac{2p}{\sqrt{\left(\frac{m_\downarrow}{M}\right)^2 + 1}}. \tag{3.10}$$

Thus, an incoming polaron with zero momentum just samples the diagonal $P = p_r$, while the integration area grows wider with increasing momentum, but also miss the bottom left corner of the cross section as shown in Fig. 3.4. This behaviour is directly seen when calculating the polarons scattering rate in the following section. We note that the integrand in Eq. (3.3) in addition to the cross section is weighted by Fermi functions for the majority atoms, which ensures that atoms around the Fermi surface dominates for low temperatures.

3.3 Scattering Rate of the Fermi Polaron

Having analysed the scattering cross section σ for an interacting impurity in a Fermi sea in great detail with and without medium and effective range effects and as a function of energy, interaction strength, temperature, centre of mass and relative momentum, we now turn our attention to the scattering rate of the Fermi polaron. In this section we obtain the scattering rate of the Fermi polaron by averaging over all scattering events for the impurity in the Fermi sea Eq. (3.3). We will see how the scattering rate behaves as a function of the polarons momentum and the temperature of the system, and how the different cross sections influence scattering rate. Introducing medium effects, we introduce two competing effects for the scattering rate: Fermi blocking will limit the scattering rate at low temperatures and momenta, while the possibility of scattering through a Cooper resonance as discussed in the previous section can drastically enhance the scattering rate on the BCS side. An important effect when we model the decoherence rate of Ref. [53] in the following chapter.

We obtain the scattering rate for the Fermi polaron from Eq. (3.3) using the relevant cross section. Fig. 3.5 shows the scattering rate for

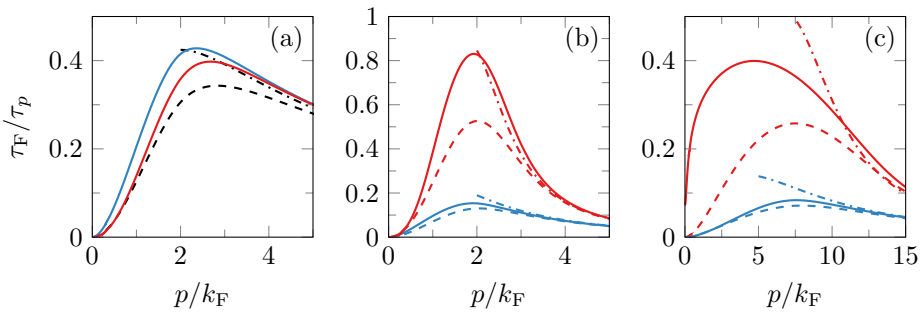

Figure 3.5: The scattering rate $1/\tau_p$ of a Fermi polaron with momentum p for $T = 0.01\,T_F$, $k_F a = 1$ (red) and $k_F a = -1$ (blue) and (a) $k_F r_{eff} = 0$, $m_\downarrow/m_\uparrow = 1$, (b) $k_F r_{eff} = -1.8$, $m_\downarrow/m_\uparrow = 1$, (c) $k_F r_{eff} = -1.8$, $m_\downarrow/m_\uparrow = 40/6$. The full lines are the scattering rates, while the dashed lines are the vacuum scattering rates and the dashdotted lines show the classical limits of the scattering rates. T_F is the Fermi temperature and $\tau_F = 1/\epsilon_F$ is the Fermi time.

$T = 0.01\,T_F$ and $k_F a = \pm 1$ as a function of the polarons incoming momentum for a broad and narrow resonance with mass balance and mass imbalance. We compare the scattering rate with the vacuum scattering rate obtained by using σ_v in Eq. (3.3). Note that the vacuum scattering length is symmetric with respect to $\pm a$ for a broad resonance, while there is no such symmetry for the narrow resonance.

For the broad resonance with equal mass Fig. 3.5(a), we see that medium effects enhance the scattering rate throughout, but the effects are at maximum on the order of a factor of 2 and largest on the BEC side. Introducing respectively a narrow Feshbach resonance along with the experimentally relevant masses Figs. 3.5(b-c), we see that the scattering rate is significantly increased on the BCS side up to a factor of 4 compared to the vacuum scattering rate. At the same time, we see that medium effects decline on the BEC side. These observations are consistent with the discussion of the cross section above, where we saw from Fig. 3.2 that the resonance shifted to the BCS side when introducing a narrow resonance and the relevant masses for the ^{40}K-^{6}Li system. Likewise, it is also consistent with the

discussion following Fig. 3.4, where we saw the Cooper resonance dominating a larger part of the integration area of Eq. (3.3), especially for the dominating momenta close to the Fermi surface.

We see from Fig. 3.5 that scattering events are frozen out by Pauli blocking for small momenta as expected. Interestingly, we see from Fig. 3.5(c) that the low p dependence of the scattering rate is changed by medium effects. It would be an interesting problem to examine this p dependence analytically in order to extract the power law, but this is beyond the scope of this thesis. The high p dependence of the scattering rate can, however, be determined analytically. For high momenta Fermi blocking becomes insignificant and we can set $f_{2\uparrow}(1-f_{4\uparrow}) \approx f_{2\uparrow}$ in Eq. (3.3). Furthermore, since the incoming momentum $\boldsymbol{p}$ completely dominates $\boldsymbol{p}_2$, we set the relative momentum to $\boldsymbol{p}_r \approx \frac{m_\uparrow}{M}\boldsymbol{p}$ making the cross section independent of $\boldsymbol{p}_2$ and the integral in Eq. (3.3) spherically symmetric. We can then obtain the classical scattering as[76]

$$\frac{1}{\tau_p} = \frac{4\pi n_\uparrow}{m_\downarrow} \frac{a^2 p}{\left(\frac{(m_\uparrow/M)^2 p^2 r_{\text{eff}}(a-a_{\text{bg}})-2}{(m_\uparrow/M)^2 p^2 r_{\text{eff}} a_{\text{bg}}(1-a_{\text{bg}}/a)-2}\right)^2 + \left(\frac{m_\uparrow}{M} a p\right)^2} \tag{3.11}$$

for $p \gg k_{\text{F}}, \sqrt{2m_\uparrow T}$. As we would expect, we see that the scattering rate approaches this value in Fig. 3.5.

In Fig. 3.6 we show the temperature dependence of the scattering rate for a zero momentum polaron at $k_{\text{F}}a = \pm 1$ under the same conditions for the cross section as for the momentum dependence. As for the momentum dependence we see that introducing medium effects enhance the scattering rate for the Fermi polaron compared to the vacuum scattering rate. Likewise, we also see that the largest enhancement of the scattering rate appears on the BEC side for a broad resonance and on the BCS side for a narrow resonance and the mass imbalanced case. Again, this is due to the shift of the Cooper resonance towards the BCS side.

We also see that the low T dependence of the scattering rate is changed by medium effects. This dependence is an interesting problem in itself, but is again beyond the scope of this thesis. As discussed above, the pairing correlations vanish at high temperatures

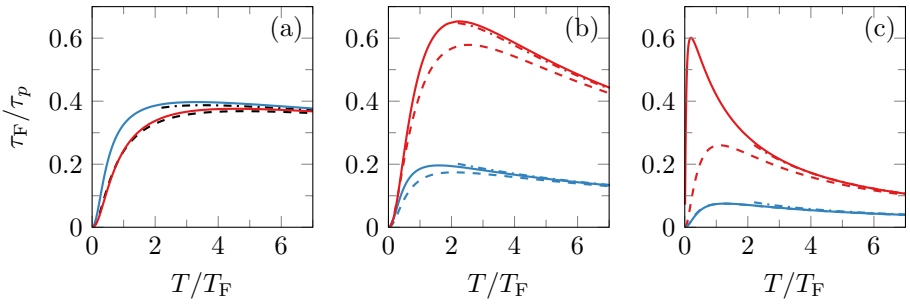

Figure 3.6: The scattering rate $1/\tau_p$ of a Fermi polaron with zero momentum as a function of temperature for $k_F a = 1$ (red) and $k_F a = -1$ (blue), and (a) $k_F r_{\text{eff}} = 0$, $m_\downarrow/m_\uparrow = 1$, (b) $k_F r_{\text{eff}} = -1.8$, $m_\downarrow/m_\uparrow = 1$, (c) $k_F r_{\text{eff}} = -1.8$, $m_\downarrow/m_\uparrow = 40/6$. The full lines are the scattering rates, while the dashed lines are the vacuum scattering rates and the dashdotted lines show the classical limits of the scattering rates. T_F is the Fermi temperature and $\tau_F = 1/\epsilon_F$ is the Fermi time.

$T \gg \epsilon_F$ and we reach the classical limit as seen in Fig. 3.6. In the limit of $T \gg \epsilon_F$ and $p \ll \sqrt{m_\downarrow^2 T/m_\uparrow}$, we can express the scattering rate of the Fermi polaron Eq. (3.3) as

$$\frac{1}{\tau_p} = 2n_\uparrow \sqrt{\frac{2T}{\pi m_\uparrow}}\bar{\sigma}\,, \tag{3.12}$$

where

$$\bar{\sigma} = 8\pi a^2 \int_0^\infty \mathrm{d}x \, \frac{x^3 e^{-x^2}}{\left(\frac{T r_{\text{eff}}(a-a_{\text{bg}})x^2 - 2T_a a^2}{T r_{\text{eff}} a_{\text{bg}}(1-a_{\text{bg}}/a)x^2 - 2T_a a^2}\right)^2 + \frac{T}{T_a}x^2} \tag{3.13}$$

is an effective cross section with $T_a = M/(2m_r m_\downarrow a^2)$. Finally, we note that for a broad resonance $r_{\text{eff}} = 0$, we can express the scattering rate in the weak and strong coupling limits as[76]

$$\frac{1}{\tau_p} = 4n_\uparrow \sqrt{\frac{2\pi}{m_\uparrow}} \times \begin{cases} 2a^2\sqrt{T} & \text{for} \quad T_a \gg T \\ \frac{m_\uparrow}{m_r^2}\frac{1}{\sqrt{T}} & \text{for} \quad T_a \ll T \end{cases}. \tag{3.14}$$

In conclusion we see that the scattering rate of a Fermi polaron is drastically enhanced at low temperatures and for momenta smaller than or comparable to the Fermi momentum of the majority atoms when including medium and finite range effects from the Feshbach resonance into the $\mathcal{T}$-matrix. We have seen that this enhancement originates from pair correlations as a reminiscence of the Cooper resonance in the population balanced system. Additionally, we have seen the importance of explicitly including the narrow Feshbach resonance as well as the mass imbalance in the cross section when doing quantitative calculations to compare with experiment. A similar increase in the scattering rate have been shown in population balanced systems, strongly affecting the damping of collective modes, the shear viscosity, and the spin diffusion constant.[88–93]

[88]S. Riedl et al. *Phys. Rev. A*, **78**: 053609, 2008.
[89]S. K. Baur et al. *Phys. Rev. A*, **87**: 043612, 2013.
[90]M. Urban et al. *J. Phys.: Conference Series*, **497**: 012028, 2014.
[91]G. M. Bruun and H. Smith. *Phys. Rev. A*, **72**: 043605, 2005.
[92]T. Enss et al. *Phys. Rev. A*, **86**: 013617, 2012.
[93]T. Enss. *Phys. Rev. A*, **88**: 033630, 2013.

CHAPTER

4 Decoherence of the Fermi Polaron

This chapter discussed work published in Refs. [52, 53], where we relate the scattering rate of the Fermi polaron to the experimentally observed decoherence of an impurity in a Fermi sea.

Having analysed the scattering rate of the Fermi polaron in great detail, we are now ready to relate this result to the decoherence rate of an impurity in a Fermi sea and compare quantitatively with an experiment performed by the group of R. Grimm at IQOQI in Innsbruck.[52,53] Hence, we will thermally average the polaron scattering rate obtained using the mass ratio and the cross section including effective range relevant for the experiment, where ^{40}K impurities are emerged in a ^{6}Li Fermi sea. Again, some parts of this work appeared in my Master's thesis, which will be cited accordingly.[76]

As discussed, the minority atoms in a two-component Fermi gas with a large population imbalance form quasiparticles coined Fermi polarons. The existence of quasiparticles have been confirmed by multiple experiments, but in this chapter we present the first experimental analysis of the minority atoms decoherence due to the scattering between quasiparticles and majority atoms in a three-dimensional

[52]R. S. Christensen and G. M. Bruun. *Phys. Rev. A*, **91**: 042702, 2015.

[53]M. Cetina et al. *Phys. Rev. Lett.*, **115**: 135302, 2015.

[76]R. S. Christensen. *Collision Rate of Polarons*. Master's Thesis. Aarhus University, Aug. 2013.

gas.[41–43,53] The decoherence rate is measured by atom spin-echo interferometry determining the coherence of a superposition of internal states in the minority atoms as discussed in Sections 2.4 and 2.5.[72,73]

In this chapter we present the overall characteristics and results from the experiment, but we focus on the theoretical modelling of the experiment relating the scattering rate of a single polaron discussed in the previous chapter to the experimentally measured decoherence rate of the impurity atoms, since this is the main contribution from the author. Hence, we focus on the decoherence rate for weak to moderate interaction strength within the valid range of Fermi liquid theory. The decoherence rate closer to unitarity has been discussed in more recent work by the same experimental group.[94]

4.1 MODELLING THE DECOHERENCE RATE

Experimentally, the Grimm group starts with a mixture of, typically, 3×10^5 ^{6}Li atoms and 1.5×10^4 ^{40}K atoms thermally equilibrated at a few hundred nanokelvin. At this temperature and with the applied trap settings the ^{6}Li majority atoms are degenerate, while the ^{40}K impurity atoms form a classical gas. For the remaining part of this chapter, we will refer to the ^{6}Li atoms as the majority atoms and the ^{40}K atoms as the minority atoms.

As discussed in Section 2.5 we can relate the experimental decoherence of a superposition of two internal states of the impurity atoms to the scattering rate of the Fermi polaron Eq. (2.42). In order to obtain the mean scattering rate of the polarons and hence the decoherence rate, we calculate the thermally averaged scattering

[41] A. Schirotzek et al. *Phys. Rev. Lett.*, **102**: 230402, 2009.
[42] C. Kohstall et al. *Nature*, **485**: 615–618, 2012.
[43] M. Koschorreck et al. *Nature*, **485**: 619–622, 2012.
[72] A. D. Cronin et al. *Rev. Mod. Phys.*, **81**: 1051–1129, 2009.
[73] M. Knap et al. *Phys. Rev. X*, **2**: 041020, 2012.
[94] M. Cetina et al. *Science*, **354**: 96–99, 2016.

rate[76]

$$\gamma_{\text{scat}} = \frac{1}{n_\downarrow} \int \frac{\mathrm{d}^3 p_1}{(2\pi)^3} f_{1\downarrow} \frac{1}{\tau_{p_1}}, \tag{4.1}$$

where the scattering rate for a polaron with momentum $\boldsymbol{p}_1$ is $1/\tau_{p_1}$, $f_{1\downarrow}$ is the Fermi distribution for the polarons and $n_\downarrow$ the density. The scattering rate is given by Eq. (3.1) and by inserting this, we have

$$\gamma_{\text{scat}} = \frac{2m_r}{(2\pi)^6 n_\downarrow} \int_0^\infty \mathrm{d}P\, P^2 \int_0^\infty \mathrm{d}p_r\, p_r^3 \int_{-1}^1 \mathrm{d}\cos\theta \int_{-1}^1 \mathrm{d}\cos\theta' \times W(12;34) f_{1\downarrow}[f_{2\uparrow}(1-f_{3\downarrow}-f_{4\uparrow})+f_{3\downarrow}f_{4\uparrow}], \tag{4.2}$$

where m_r is the reduced mass of the system, $\boldsymbol{P}$ is the total centre of mass momentum, $\boldsymbol{p}_r$ is the relative momentum, θ (θ') is the angle of the incoming (outgoing) relative momentum with respect to $\boldsymbol{P}$. $W(12;34)$ is the transition probability as discussed in Section 3.1, while $f_{p\sigma} = [e^{\beta(\epsilon_{p\sigma}-\mu_\sigma)}+1]^{-1}$ with $\beta = 1/T$ is the Fermi distribution function for an atom with kinetic energy $\epsilon_{p\sigma} = p^2/2m_\sigma$ and chemical potential μ_σ. At this level we see that we already have 4 convoluted integrals with even more appearing in the $\mathcal{T}$-matrix entering the transition probability W, making the computations numerically hard.

Input Parameters

In order to calculate the decoherence rate of the impurity atoms, we need a range of input parameters for Eq. (4.2) which are set by the experimental conditions. In total Eq. (4.2) depends on the following dimensionless quantities: $k_{\text{F}}a, T/\epsilon_{\text{F}}, k_{\text{F}}r_{\text{eff}}$, and $\bar{n}_\downarrow/\bar{n}_\uparrow$, where $\epsilon_{\text{F}} = k_{\text{F}}^2/2m_\uparrow = (6\pi^2\bar{n}_\uparrow)^{2/3}/2m_\uparrow$ is the average Fermi energy of the majority atoms sampled by the impurities, T is the temperature, r_{eff} is the effective range and $\bar{n}_\downarrow$ ($\bar{n}_\uparrow$) is the average impurity (majority) density sampled by the impurity atoms.

In Fig. 4.1 we show an example of the density profiles in the experimental setup using experimentally relevant quantities. The

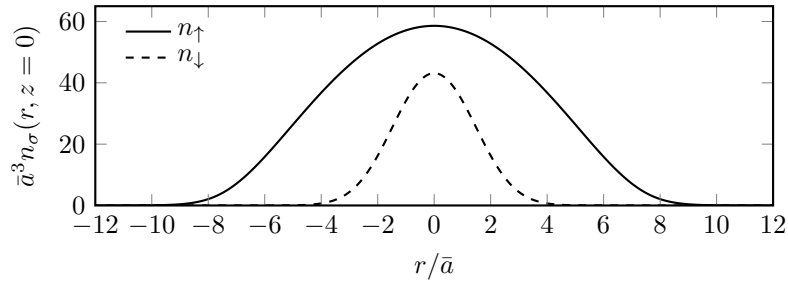

Figure 4.1: Typical densities of the minority spin-↓ atoms and the majority spin-↑ atoms for the radial (axial) distance $r = \sqrt{x^2+y^2}$ at $z = 0$. We have $\bar{a} = 1/(m_\uparrow(\omega_{r\uparrow}^2\omega_{z\uparrow})^{1/3})$, where $\omega_{r\sigma}$ ($\omega_{z\sigma}$) is the radial (axial) trapping frequency for the σ-atoms. The density profiles shown are for $T = 290\,\mathrm{nK}$, $\omega_{r,\uparrow} = 2\pi \times 632\,\mathrm{Hz}$, $\omega_{z,\uparrow} = 2\pi \times 80\,\mathrm{Hz}$, $\omega_{r,\downarrow} = 2\pi \times 395\,\mathrm{Hz}$, $\omega_{z,\downarrow} = 2\pi \times 50\,\mathrm{Hz}$, $N_\uparrow = 3 \times 10^5$, $N_\downarrow = 1.5 \times 10^4$, $m_\uparrow = 6.0\,\mathrm{u}$, and $m_\downarrow = 40\,\mathrm{u}$ with N_σ being the total number of σ-atoms.

density profile for the impurity atoms is perfectly Gaussian signalling a classical gas of impurity atoms.

Since, we do not experimentally obtain the ideal situation of a singly impurity in a Fermi sea, we in principle have to make Eq. (4.2) spatially dependent using locally determined Fermi energies and chemical potentials within the Thomas-Fermi approximation. This would constitute a substantial calculation where we would then average the local scattering rate across the full extension of the trap. An approach which is infeasible at the moment due to the number of convoluted integrals appearing.

We see, however, from Fig. 4.1 that the impurity atoms due to their smaller spatial extension only probe a central region of the majority atoms, where the local density distribution of the majority atoms is relatively flat. Thus, instead of averaging the local scattering rate or just use the peak value quantities for e.g. the Fermi energy at the center of the trap, we average all input parameters over the impurity cloud. Hence, we define e.g. the Fermi energy of the

majority atoms as the average over the impurity cloud

$$\epsilon_{\mathrm{F}} = \frac{1}{N_{\downarrow}} \int \mathrm{d}^3 r \, n_{\downarrow}(\boldsymbol{r}) E_{\uparrow}^{\mathrm{F}}(\boldsymbol{r}), \tag{4.3}$$

where $E_{\uparrow}^{\mathrm{F}}(\boldsymbol{r}) = (6\pi^2 n_{\uparrow}(\boldsymbol{r}))^{2/3}/2m_{\uparrow}$ is the local Fermi energy of the majority atoms, $n_{\sigma}(\boldsymbol{r})$ is the local density of the σ atoms obtained within the Thomas-Fermi approximation, and $N_{\downarrow}$ is the total number of impurity atoms.[7,95] $\bar{n}_{\uparrow}$ and $\bar{n}_{\downarrow}$ are defined in the same manner. The standard deviation of the local Fermi energy of the majority atoms with respect to the averaged value given by Eq. (4.3) is less than 10 % justifying the use of averaged quantities.[53]

Experimental Errors On the Input Parameters

As mentioned above, the scattering rate Eq. (4.2) depends on the 4 parameters: $k_{\mathrm{F}}a, T/\epsilon_{\mathrm{F}}, k_{\mathrm{F}}r_{\mathrm{eff}}$, and $\bar{n}_{\downarrow}/\bar{n}_{\uparrow}$, which are all associated with experimental uncertainties. We include these errors in our calculations and then only show the statistical errors from the experimental measurement of the decoherence as error bars, when we present our results in Figs. 4.3 and 4.4 in the following section. The errors introduced into the dimensionless input parameters originates from the calibration of the majority atom number, which introduces a systematic error in the Fermi energy ϵ_{F} and the associated Fermi momentum k_{F}, as well as the systematic error in a and r_{eff} arising from uncertainties in the determination of ΔB and B_0 characterising the Feshbach resonance.[53] Since the dimensionless input parameters all depend on the Fermi energy and e.g. both r_{eff} and a_{bg} depend on the characteristics of the Feshbach resonance, the input parameters are all correlated.

If we define our scattering rate $\gamma_{\mathrm{scat}}(\boldsymbol{u})$ Eq. (4.2) as a function an input vector

$$\boldsymbol{u} = \begin{pmatrix} T/T_{\mathrm{F}} & k_{\mathrm{F}}R^* & k_{\mathrm{F}}a_{\mathrm{bg}} & \bar{n}_{\downarrow}/\bar{n}_{\uparrow} \end{pmatrix}, \tag{4.4}$$

[7] S. Giorgini et al. *Rev. Mod. Phys.*, **80**: 1215–1274, 2008.

[95] M. Inguscio et al., eds. *Proceedings of the International School of Physics "Enrico Fermi", Course CLXIV, Ultra-cold Fermi Gases* IOS Press, 2007

where $R^* = -r_{\text{eff}}/2$, we express the mean values of the input parameters as

$$\boldsymbol{u}_0 = \begin{pmatrix} 0.16 & 0.93 & 0.022 & 0.27 \end{pmatrix}. \tag{4.5}$$

The associated errors on the parameters in $\boldsymbol{u}_0$ can then be expressed in a 1σ (standard deviation) covariance matrix[96]

$$\Sigma = \begin{array}{c} \\ T/T_{\text{F}} \\ k_{\text{F}}R^* \\ k_{\text{F}}a_{\text{bg}} \\ \bar{n}_\downarrow/\bar{n}_\uparrow \end{array} \begin{array}{c} \begin{array}{cccc} T/T_{\text{F}} & k_{\text{F}}R^* & k_{\text{F}}a_{\text{bg}} & \bar{n}_\downarrow/\bar{n}_\uparrow \end{array} \\ \begin{pmatrix} 1.9216 & -2.6784 & -0.063\,36 & 2.3328 \\ -2.6787 & 19.5682 & 0.277\,472 & -6.7797 \\ -0.0634 & 0.2775 & 0.006\,534 & -0.1604 \\ 2.3328 & -6.7797 & -0.160\,38 & 54.9049 \end{pmatrix} \end{array} \times 10^{-4}. \tag{4.6}$$

By assuming that all errors are Gaussian of nature, we can determine the orthogonal eigendirections $\boldsymbol{v}_n$ in the 4-parameter space $\boldsymbol{u}$, where the errors along the eigendirections are uncorrelated. The eigendirections are the eigenvectors of Σ and the variance σ_n^2 along these directions are given by the associated eigenvalues λ_n. We illustrate this concept for two parameters with correlated errors in Fig. 4.2.

We assume the scattering rate $\gamma_{\text{scat}}(\boldsymbol{u})$ to be well-behaved and smooth in a region around $\boldsymbol{u}_0$, and finally estimate the errors on our theory curves originating from the underlying experimental errors by calculating

$$\gamma_n = \gamma_{\text{scat}}(\boldsymbol{u}_n) \tag{4.7}$$

with $\boldsymbol{u}_n = \boldsymbol{u}_0 + \sigma_n \boldsymbol{v}_n$ and estimate the 1σ error by

$$\sigma_{\text{scat}} = \sqrt{\sum_{n=1}^{4} (\gamma_n - \gamma_0)^2}, \tag{4.8}$$

where $\gamma_0 = \gamma_{\text{scat}}(\boldsymbol{u}_0)$. Thus, we calculate γ_n, $n = 0, \ldots, 4$ for each value of $k_{\text{F}}a$.

[96] M. Cetina personal communication Apr. 9, 2015

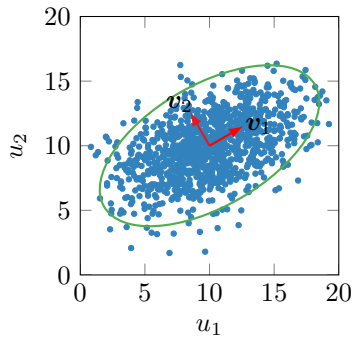

Figure 4.2: Illustration of Gaussian distributed correlated errors with two observables. The observables u_1 and u_2 have correlated errors, and the observed data is shown as blue dots. By determining the eigenvectors v_1 and v_2 and eigenvalues λ_1 and λ_2 of the associated covariance matrix, the errors along the directions v_1 and v_2 are uncorrelated with variances λ_1 and λ_2 respectively. The ellipse helps to illustrate the directions for the uncorrelated errors.

The input parameters Eq. (4.5) and the associated covariance matrix Eq. (4.6) shown here are used to calculate the curve including medium effects on the BCS side as well as the curve neglecting medium effects in Fig. 4.3. Completely analogous calculations have been made for the remaining theory curves in Figs. 4.3 and 4.4.

4.2 Results

As discussed, the observable quantity is not the scattering rate, but the associated decoherence rate determined through rf spectroscopy. We show the measured decoherence rate as a function of the interacting strength in Fig. 4.3. Along with the data points we show theory curves where the scattering rate has been calculated by Eq. (4.2) and related to the decoherence rate through Eq. (2.42). Note that the direct decay Γ is only included for $a > 0$, since the decay to the molecular state is only possible here.

We show the theory curves as lines associated with a shaded area. The lines are the decoherence rate calculated using the mean values

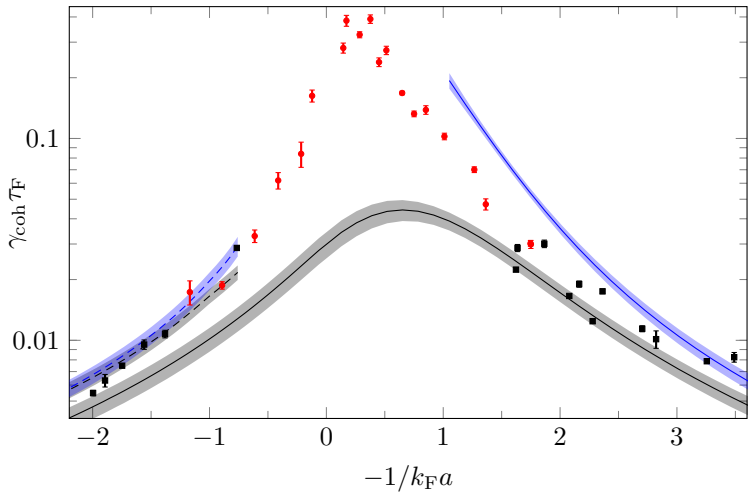

Figure 4.3: Decoherence rate in units of $1/\tau_{\mathrm{F}} = \epsilon_{\mathrm{F}}$ of ^{40}K impurities in a ^{6}Li Fermi sea as a function of the scattering length for an average temperature $T = 0.16\,\epsilon_{\mathrm{F}}$. The solid blue (black) line are the theory predictions for the decoherence rate with (without) medium corrections in the cross section. The dashed lines include corrections due to the decay of the polaron to a dimer. The shaded areas are the $1\,\sigma$ errors on the theory curves due to experimental uncertainties (see text). The red and black data points are measured with two different experimental techniques, see Ref. [53]

for the input parameters, while the shaded error show the standard deviation of the theory curves as given by Eq. (4.8). Hence, we show γ_0 for the theory curves and a shaded area between $\gamma_0 \pm \sigma_{\mathrm{scat}}$.

In Fig. 4.3 we show a curve (black, solid) neglecting all medium effects in the cross section, but including the effective range of the Feshbach resonance. Hence, we use the $\mathcal{T}$-matrix given by Eq. (3.5), but with the pair-propagator set equal to the vacuum pair-propagator Eq. (3.6). On the BCS side ($a < 0$) we show a curve (blue, solid) including medium effects from the surrounding Fermi sea on the scattering cross section for the impurity, i.e. the possibility of scattering through the Cooper resonance. In principle, we also include medium effects from the finite number of impurities, but since $T/T_{\mathrm{F}\downarrow} \sim 2.5$ these effects are negligible since the gas is classical. This is supported by the fact that the data does not show any clear dependence on $\bar{n}_\downarrow/\bar{n}_\uparrow$

across the range $0.17 \leq \bar{n}_\downarrow/\bar{n}_\uparrow \leq 0.43$ (not shown).[53] On the BEC side ($a > 0$) we show a curve (blue, dashed) which in addition to medium effects in scattering cross section include effects from the decay of the polaron into a lower lying dimer state of an impurity atom bound with a majority atom. The polaron decays into the dimer state at a rate Γ and as for the scattering rate, this contributes directly to the decoherence rate with $\Gamma/2$ as stated in Eq. (2.42). Furthermore, the decay into the dimer state releases energy and creates holes in the Fermi sea increasing the temperature to $T/T_\mathrm{F} = 0.20 \pm 0.01$ during the measurement time. The decay rate Γ was calculated and measured in Ref. [42] and we include this and the increased temperature for the dashed curves on the BEC side. Likewise, the black, dashed curve on the BEC side neglects medium effects in the cross section, but include the dimer decay as well as the increased temperature.

We see from Fig. 4.3 that the calculated decoherence rate agrees well with the experimental data for $-1/k_\mathrm{F}a \gtrsim 1.5$ and $-1/k_\mathrm{F}a \lesssim 1$. On the BEC we see excellent agreement, but on the BCS side it seems that including medium effects in the cross section overestimates the decoherence rate, while it is underestimated when medium effects are neglected. We do, however, obtain a reasonable quantitative agreement between theory and experiment, which confirms our interpretation of the decoherence rate as caused by scattering of well-defined quasiparticles for weak to moderate interactions. Closer to unitarity for $1/|k_\mathrm{F}a| < 1$ the quasiparticle picture breaks down and we do not expect the measured decoherence rate to agree with Fermi liquid theory.

Furthermore, we see a significant asymmetry in the decoherence rate around $-1/k_\mathrm{F}a = 0$, which is reproduced in the theory curves by the inclusion of the effective range from the Feshbach resonance. We found the inclusion of the effective range parameter to be very important in order to obtain quantitative agreement between theory and experiment.

As we discussed in the previous chapter, the inclusion of the effective range shifted the Cooper resonance towards the BCS side, where we saw large increases for the scattering rate. This effect is reproduced in Fig. 4.3, where medium effects in the cross section drastically enhance the decoherence rate, such that it seems to over-

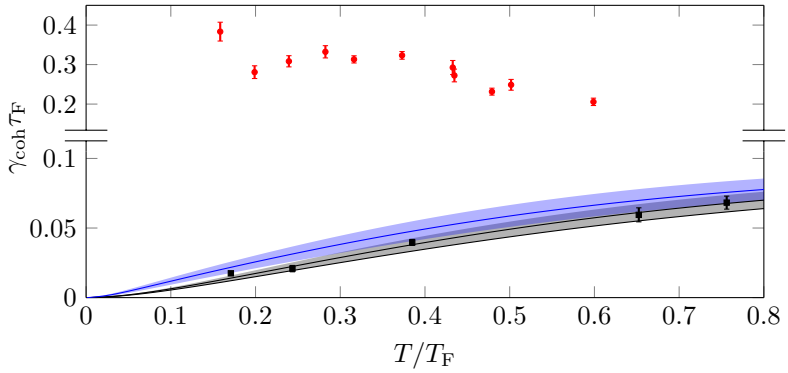

Figure 4.4: Decoherence rate in units of $1/\tau_{\mathrm{F}} = \epsilon_{\mathrm{F}}$ of ^{40}K impurities in a ^{6}Li Fermi sea as a function of the temperature for $-1/k_{\mathrm{F}}a = 2.4$, $k_{\mathrm{F}}R^{*} = 0.89$, $\bar{n}_{\downarrow}/\bar{n}_{\uparrow} = 0.3$ ($-1/k_{\mathrm{F}}a = 0.2$, $k_{\mathrm{F}}R^{*} = 0.94$, $\bar{n}_{\downarrow}/\bar{n}_{\uparrow} = 0.2$) black (red). The solid blue (black) line are the theory predictions for the decoherence rate with (without) medium corrections in the cross section at $-1/k_{\mathrm{F}}a = 2.4$. The shaded areas are the $1\,\sigma$ errors on the theory curves due to experimental uncertainties. The red and black data points are measured with two different experimental techniques, see Ref. [53]

estimate the effect of pair correlation on the BCS side.

In Fig. 4.4 we show the experimentally determined temperature dependence for the decoherence rate at $-1/k_{\mathrm{F}}a = 0.2$ and $-1/k_{\mathrm{F}}a = 2.4$ as well as two theory curves for $-1/k_{\mathrm{F}}a = 2.4$. The curves color and type are the same as above. Again, we see excellent agreement between theory and experiment outside the strongly interacting regime, confirming the interpretation of scattering of quasiparticles within Fermi liquid theory. The seemingly linear dependence on temperature for the decoherence rate originates from the relatively high mass difference of the impurity ^{40}K atoms with respect to the majority ^{6}Li atoms. The mass difference causes the scattering to resemble scattering by fixed impurities, similar to the situation in metals where electrons scattered by fixed nuclei leads the decoherence of nuclear spins known to be linearly dependent on temperature.[97]

[97] J. Korringa. *Physica*, **16**: 601–610, 1950.

In conclusion, we have throughout Chapters 3 and 4 applied the Boltzmann transport equation within Fermi liquid theory in order to describe the scattering of an impurity in a Fermi sea. We have interpreted this impurity as a quasiparticle coined the Fermi polaron and investigated the scattering cross section within the ladder approximation. We saw that the inclusion of finite range and medium effects for respectively the Feshbach resonance and the Fermi sea lead to large quantitatively changes of the cross section. As we saw in this chapter these quantitative changes are important for modelling the decoherence rate observed experimentally. Including finite range and medium effects, we a reasonable agreement between theory and experiment for weak to moderate interactions, which confirmed that the decoherence is dominated by quasiparticle scattering in this regime. Finally, we saw that the Fermi liquid picture of quasiparticle scattering breaks down close to unitarity as expected.[48]

For completeness, we refer to Ref. [94] for an interpretation of the measurements close to unitarity.

[48] P. Massignan et al. *Rep. Prog. Phys.*, **77**: 034401, 2014.

CHAPTER

5 Quasiparticle Properties of the Bose Polaron

This and the following chapter builds on work published in Refs. [44, 54] discussing an impurity in a Bose gas forming a quasiparticle; the Bose polaron. This chapter describes the theoretical work done on an ideal system with a single impurity in a Bose gas at zero temperature. The following chapter discusses the theoretical modelling of an experiment done at Aarhus University observing and measuring the energy shift of the Bose polaron.[44,54]

There has been a lot of theoretical interest in the Bose polaron in recent years. However, these theories were either based on the so-called Fröhlich model or on mean-field theory.[98–101] In this chapter, we show that the Fröhlich Hamiltonian, derived for the interaction between electrons and phonons in solid state systems, miss crucial physics for the Bose polaron beyond second order perturbation theory. Furthermore, we will employ the correct microscopic Hamiltonian for an impurity emerged in a Bose gas to obtain the energy, quasiparticle residue and effective mass of the Bose polaron perturbatively to third order in the Bose-impurity scattering length.[54]

[44] N. B. Jørgensen et al. *Phys. Rev. Lett.*, **117**: 055302, 2016.
[54] R. S. Christensen et al. *Phys. Rev. Lett.*, **115**: 160401, 2015.
[98] F. Grusdt et al. *Sci. Rep.*, **5**: 12124, 2015.
[99] W. Casteels and M. Wouters. *Phys. Rev. A*, **90**: 043602, 2014.
[100] H. Bei-Bing and W. Shao-Long. *Chin. Phys. Lett.*, **26**: 080302, 2009.
[101] H. Fröhlich et al. *Philos. Mag.*, **41**: 221–242, 1950.

The quasiparticle properties of the Bose polaron obtained within perturbation theory serve to increase understanding of the weakly interacting Bose polaron and to highlight differences from the Fröhlich polaron relevant for condensed matter systems. Moreover, since the results presented in this chapter are exact, they serve as an important benchmark for more complicated theories describing the Bose polaron.[102,103]

In this chapter we start by deriving the Feynman rules from the microscopic Hamiltonian describing an impurity in a Bose-Einstein condensate (BEC). We then do a perturbative expansion of the impurity self-energy in powers of the impurity-Bose scattering length in order to derive the quasiparticle properties perturbatively. Finally, we present our results and discuss how the mass ratio between the impurity and the majority atoms as well as the Bose-Bose scattering length within the Bose gas influence the quasiparticle properties of the Bose polaron.

5.1 HAMILTONIAN AND FEYNMAN RULES

The microscopic Hamiltonian for an impurity emerged in a Bose gas is

$$\begin{aligned}\mathscr{H} = &\sum_p \epsilon_p c_p^\dagger c_p + \sum_p \epsilon_p^{\mathrm{B}} a_p^\dagger a_p + \frac{1}{2\mathcal{V}} \sum_{p,p',q} V_{\mathrm{B}}(q) a_{p+q}^\dagger a_{p'-q}^\dagger a_{p'} a_p \\ &+ \frac{1}{\mathcal{V}} \sum_{p,p',q} V(q) c_{p+q}^\dagger a_{p'-q}^\dagger a_{p'} c_p \,, \end{aligned} \tag{5.1}$$

where c_p ($c_p^\dagger$) and a_p ($a_p^\dagger$) annihilates (creates) an impurity atom with kinetic energy $\epsilon_p = p^2/2m$ and a boson with kinetic energy $\epsilon_p^{\mathrm{B}} = p^2/2m_{\mathrm{B}}$ respectively. m (m_{B}) is the mass of the impurity (boson), while V (V_{B}) is the impurity-boson (boson-boson) scattering potential and $\mathcal{V}$ is the volume of the system. Completely analogously to what was done in Section 2.2, the two scattering potentials

[102] J. Levinsen et al. *Phys. Rev. Lett.*, **115**: 125302, 2015.
[103] Y. E. Shchadilova et al. *Phys. Rev. Lett.*, **117**: 113002, 2016.

are assumed short-ranged and related to the low-energy vacuum $\mathcal{T}$-matrices $\mathcal{T}_v = 2\pi a/m_r$ and $\mathcal{T}_{\rm B} = 4\pi a_{\rm B}/m_{\rm B}$ with a ($a_{\rm B}$) the impurity-boson (boson-boson) scattering length and $m_r = m m_{\rm B}/(m+m_{\rm B})$ the reduced mass.

At zero temperature the Bose gas forms a BEC, and assuming the bosons to be weakly interacting $n_0 a_{\rm B}^3 \ll 1$ with n_0 being the condensate density, we describe the BEC using Bogoliubov theory.[104] Hence, replacing $a_0, a_0^\dagger \to \sqrt{N_0}$ and performing the Bogoliubov transformation $a_{\boldsymbol{p}} = u_p \beta_{\boldsymbol{p}} + v_p^\dagger \beta_{-\boldsymbol{p}}^\dagger$, where N_0 is the number of atoms in the condensate and $v_p^2 = u_p^2 - 1 = \frac{1}{2}[E_p^{-1}(\epsilon_p^{\rm B} + n_0\mathcal{T}_{\rm B}) - 1]$ with $E_p = \sqrt{\epsilon_p^{\rm B}(\epsilon_p^{\rm B} + 2n_0\mathcal{T}_{\rm B})}$, we express the Hamiltonian Eq. (5.1) as

$$\begin{aligned}\mathscr{H} = \mathscr{H}_{\rm BEC} + \sum_{\boldsymbol{p}} (\epsilon_p + n_0\mathcal{T}_v) c_{\boldsymbol{p}}^\dagger c_{\boldsymbol{p}} + \frac{\mathcal{T}_v}{\mathcal{V}} \sum_{\boldsymbol{p},\boldsymbol{q},\boldsymbol{p}'\neq 0,\boldsymbol{q}} c_{\boldsymbol{p}+\boldsymbol{q}}^\dagger a_{\boldsymbol{p}'-\boldsymbol{q}}^\dagger a_{\boldsymbol{p}'} c_{\boldsymbol{p}} \\ + \frac{\sqrt{N_0}\mathcal{T}_v}{\mathcal{V}} \sum_{\boldsymbol{p},\boldsymbol{q}\neq 0} \left(c_{\boldsymbol{p}-\boldsymbol{q}}^\dagger c_{\boldsymbol{p}} a_{\boldsymbol{q}}^\dagger + c_{\boldsymbol{p}+\boldsymbol{q}}^\dagger c_{\boldsymbol{p}} a_{\boldsymbol{q}} \right)\end{aligned} \tag{5.2}$$

with

$$\mathscr{H}_{\rm BEC} = E_{\rm GP} + \sum_{\boldsymbol{p}\neq 0} E_p \beta_{\boldsymbol{p}}^\dagger \beta_{\boldsymbol{p}}\,, \tag{5.3}$$

$$E_{\rm GP} = \frac{N_0^2 \mathcal{T}_{\rm B}}{2\mathcal{V}} + \frac{1}{2}\sum_{\boldsymbol{p}\neq 0} (E_p - \epsilon^{\rm B} - n_0\mathcal{T}_{\rm B})\,, \tag{5.4}$$

and $\beta_{\boldsymbol{p}}$ ($\beta_{\boldsymbol{p}}^\dagger$) being the annihilation (creation) operator for a Bogoliubov mode with momentum $\boldsymbol{p}$ and energy E_p. Thus, term by term the Hamiltonian Eq. (5.3) describes the BEC through Bogoliubov theory, the impurity kinetic energy with a mean-field shift $n_0\mathcal{T}_v$ due to interactions with the BEC, the scattering of the impurity with a boson completely outside the condensate, and finally a scattering process where a boson is either put into or taken out of the condensate. We have ignored scattering between bosons completely out of

[104] N. N. Bogoliubov. *J. Phys.*, **11**: 23–32, 1947.

the condensate, since these terms are suppressed by least a factor of $(n_0 a_B^3)^{1/2}$ in the perturbation series.

We assume the system to be homogeneous and thus, define the imaginary time Green's functions in momentum space by[57,59,105]

$$\begin{aligned} G_{11}(\boldsymbol{p},\tau) &= -\left\langle \mathscr{T}\left\{a_p^\dagger(\tau)a_p(0)\right\}\right\rangle, \qquad G(\boldsymbol{p},\tau) = -\left\langle \mathscr{T}\left\{c_p^\dagger(\tau)c_p(0)\right\}\right\rangle, \\ G_{12}(\boldsymbol{p},\tau) &= -\left\langle \mathscr{T}\left\{a_{-p}(\tau)a_p(0)\right\}\right\rangle, \quad G_{21}(\boldsymbol{p},\tau) = -\left\langle \mathscr{T}\left\{a_p^\dagger(\tau)a_{-p}^\dagger(0)\right\}\right\rangle, \end{aligned} \tag{5.5}$$

where $\mathscr{T}$ is the time ordering operator with respect to the imaginary time τ. Here, G is the impurity's Green's function, G_{11} is the regular Bose Green's function and G_{12} and G_{21} are the two anomalous Bose Green's functions. Doing a Fourier transform to imaginary frequency, we have

$$G(\boldsymbol{p}, i\omega_\lambda) = \frac{1}{i\omega_\lambda - \epsilon_p} = \longrightarrow \tag{5.6}$$

$$G_{11}(\boldsymbol{p}, i\omega_N) = \frac{u_p^2}{i\omega_N - E_p} - \frac{v_p^2}{i\omega_N - E_p} = \rightsquigarrow\!\!\leftsquigarrow, \tag{5.7}$$

$$G_{12}(\boldsymbol{p}, i\omega_N) = \frac{u_p v_p}{i\omega_N + E_p} - \frac{u_p v_p}{i\omega_N - E_p} = \rightsquigarrow\!\!\rightsquigarrow, \tag{5.8}$$

$$G_{21}(\boldsymbol{p}, i\omega_N) = \frac{u_p v_p}{i\omega_N + E_p} - \frac{u_p v_p}{i\omega_N - E_p} = \leftsquigarrow\!\!\leftsquigarrow, \tag{5.9}$$

where $i\omega_N = i2sT$ with s an integer and T the temperature is a Bose Matsubara frequency, while $i\omega_\lambda$ is a Bose or Fermi Matsubara frequency depending on the nature of the impurity. The lines shown in Eqs. (5.6) to (5.9) are used for representing the respective Green's functions when drawing Feynman diagrams.

The Feynman rules associated with the Hamiltonian stated above are straightforward to derive using Wick's theorem:[57,59,105]

[57] A. Fetter and J. Walecka. *Quantum theory of many-particle systems*. McGraw-Hill, 1971.

[59] H. Bruus and K. Flensberg. *Many-Body Quantum Theory in Condensed Matter Physics: An Introduction*. Oxford University Press, 2004.

[105] A. P. Albus et al. *Phys. Rev. A*, **65**: 053607, 2002.

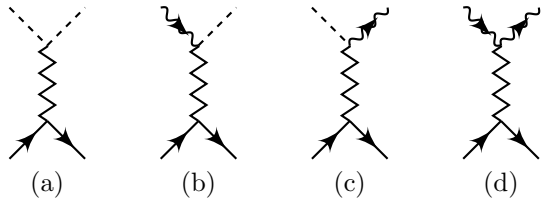

Figure 5.1: The 4 basic interaction vertices for drawing Feynman diagrams based on the Hamiltonian Eq. (5.2). The particle lines are given by Eqs. (5.6) and (5.7), while the dashed is a boson in the condensate and a zigzag line is the interaction $\mathcal{T}_v$. Note that (d) is the interaction vertex not contained in the Fröhlich model.

1. Draw all topologically distinct diagrams with n interaction lines and $2n+1$ directed particle lines satisfying that each interaction line is joined with an incoming and outgoing impurity line at one end and an incoming and outgoing boson line at the other end. The basic interactions are shown in Fig. 5.1.

2. Assign a direction to each line. Associate a momentum and a Matsubara frequency with each line and conserve each quantity at every vertex.

3. Associate a factor of $\sqrt{n_0}$ for a condensate line and the correct Green's function, given by Eqs. (5.6) to (5.9), for the remaining lines.

4. Integrate over the n independent momenta and Matsubara frequencies.

5. Assign a factor of $(-2\pi)^{-4n}(-1)^F(-1)^C$, where F is the number of closed fermion loops and C is the number of condensate factors n_0 appearing.

5.2 PERTURBATION THEORY FOR THE SELF-ENERGY

Having derived the Feynman rules for the system, we want to determine the self-energy of the impurity perturbatively to third order in the impurity-boson scattering length a. In this section, we state the general power series for the self-energy and evaluate the self-energy to second order as well as the pair-propagators appearing for the system. We also discuss the compliance to second order between the approach applied here and a perturbation theory using the Fröhlich Hamiltonian, before we in the following sections derive the self-energy and quasiparticle properties to third order.

As discussed in Section 2.3 the energy for a quasiparticle is determined by self-consistently solving Eq. (2.14):

$$\omega = \epsilon_p + \mathfrak{Re}[\Sigma(\boldsymbol{p}, \omega)], \tag{5.10}$$

for the energy ω, where Σ is the self-energy of the quasiparticle.

We want to determine the polaron energy E_{pol} perturbatively to third order in the scattering length a and hence, we do a diagrammatic expansion of Eq. (5.10) for small scattering lengths a to obtain a power series for the energy

$$\begin{aligned}\omega &\simeq \epsilon_p + \mathfrak{Re}[\Sigma_1(\boldsymbol{p}, \omega)] + \mathfrak{Re}[\Sigma_2(\boldsymbol{p}, \omega)] + \mathfrak{Re}[\Sigma_3(\boldsymbol{p}, \omega)] \\ &= \epsilon_p + \mathcal{T}_v \mathfrak{Re}[\tilde{\Sigma}_1(\boldsymbol{p}, \omega)] + \mathcal{T}_v^2 \mathfrak{Re}[\tilde{\Sigma}_2(\boldsymbol{p}, \omega)] + \mathcal{T}_v^3 \mathfrak{Re}[\tilde{\Sigma}_3(\boldsymbol{p}, \omega)],\end{aligned} \tag{5.11}$$

where Σ_n are self-energies of order a^n and $\tilde{\Sigma}_n$ are integrals to be determined by evaluating the self-energy Feynman diagrams of the corresponding order.

Self-Energy To Second Order And Pair-Propagators

To first order in the scattering length a, we have two diagrams for the self-energy which are easily evaluated

$$\Sigma_{1a} = \quad = n_0 \mathcal{T}_v, \qquad \Sigma_{1b} = \quad = n_{\text{exc}} \mathcal{T}_v, \tag{5.12}$$

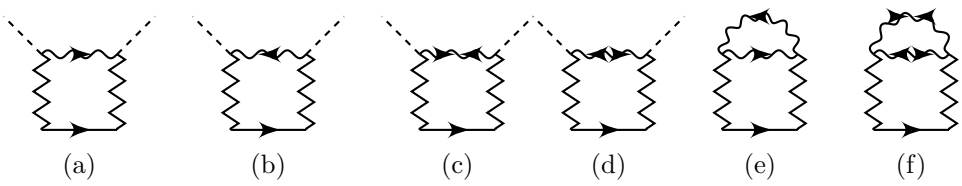

Figure 5.2: The second order self-energy diagrams for an impurity interacting with a Bose gas. The particle lines are given by Eqs. (5.6) to (5.9), while the dashed is a boson in the condensate and a zigzag line is the interaction $\mathcal{T}_v$.

where $n_{\rm exc} = -\frac{1}{\beta\mathcal{V}}\sum_{i\omega_N,\boldsymbol{q}} G_{11}(\boldsymbol{q}, i\omega_N) = \frac{8}{3\sqrt{\pi}}(n_0 a_{\rm B}^3)^{1/2}$ is the density of bosons excited out of the condensate due to the boson-boson interaction. We immediately recognize the sum of the two first order diagrams as simply the well-known mean-field shift $\Sigma_1 = (n_0 + n_{\rm exc})\mathcal{T}_v = n\mathcal{T}_v$.[55,57,59]

Every time we encounter a boson loop as the one in the Feynman diagram for Σ_{1b}, we obtain a factor of $n_{\rm exc} \propto (n_0 a_{\rm B}^3)^{1/2}$. Since, we assume $n_0 a_{\rm B}^3 \ll 1$ we will ignore all such terms for the self-energy. Note that this also corresponds to setting $n_0 = n$.

In Fig. 5.2 we show all self-energy diagrams for the impurity atom to second order. We ignore diagrams Figs. 5.2(e-f), since they contain a boson loop and are thus suppressed with a factor $(n_0 a_{\rm B}^3)^{1/2}$ compared to the remaining 2nd order diagrams. Evaluating the Feynman diagrams, we obtain for the four remaining 2nd order diagrams

$$\Sigma_{2a}(\boldsymbol{p}, i\omega_\lambda) = n_0 \mathcal{T}_v^2 \Pi_{11}(\boldsymbol{p}, i\omega_\lambda), \tag{5.13}$$
$$\Sigma_{2b}(\boldsymbol{p}, i\omega_\lambda) = n_0 \mathcal{T}_v^2 \Pi_{22}(\boldsymbol{p}, i\omega_\lambda), \tag{5.14}$$
$$\Sigma_{2c}(\boldsymbol{p}, i\omega_\lambda) = n_0 \mathcal{T}_v^2 \Pi_{12}(\boldsymbol{p}, i\omega_\lambda), \tag{5.15}$$
$$\Sigma_{2d}(\boldsymbol{p}, i\omega_\lambda) = n_0 \mathcal{T}_v^2 \Pi_{21}(\boldsymbol{p}, i\omega_\lambda), \tag{5.16}$$

[55] C. Pethick and H. Smith. *Bose-Einstein Condensation in Dilute Gases*. Cambridge University Press, 2002.

where

$$\begin{aligned}\Pi_{11}(\boldsymbol{p}, i\omega_\lambda) &= \frac{1}{\mathcal{V}}\sum_{\boldsymbol{q}}\Big[-\frac{1}{\beta}\sum_{i\omega_N} G_{11}(\boldsymbol{q}, i\omega_N)G(\boldsymbol{p}-\boldsymbol{q}, i\omega_\lambda - i\omega_N) + \frac{2m_r}{q^2}\Big] \\ &= \int\frac{\mathrm{d}^3 q}{(2\pi)^3}\Big[\frac{u_q^2(1+b(E_q))}{i\omega_\lambda - E_q - \epsilon_{p-q}} + \frac{v_q^2 b(E_q)}{i\omega_\lambda + E_q - \epsilon_{p-q}} + \frac{2m_r}{q^2}\Big],\end{aligned} \tag{5.17}$$

$$\begin{aligned}\Pi_{22}(\boldsymbol{p}, i\omega_\lambda) &= -\frac{1}{\beta}\sum_{i\omega_N}\frac{1}{\mathcal{V}}\sum_{\boldsymbol{q}} G_{11}(\boldsymbol{q}, i\omega_N)G(\boldsymbol{p}+\boldsymbol{q}, i\omega_\lambda + i\omega_N) \\ &= \int\frac{\mathrm{d}^3 q}{(2\pi)^3}\Big[\frac{v_q^2(1+b(E_q))}{i\omega_\lambda - E_q - \epsilon_{p-q}} + \frac{u_q^2 b(E_q)}{i\omega_\lambda + E_q - \epsilon_{p-q}}\Big],\end{aligned} \tag{5.18}$$

$$\begin{aligned}\Pi_{12}(\boldsymbol{p}, i\omega_\lambda) &= -\frac{1}{\beta}\sum_{i\omega_N}\frac{1}{\mathcal{V}}\sum_{\boldsymbol{q}} G_{12}(\boldsymbol{q}, i\omega_N)G(\boldsymbol{p}-\boldsymbol{q}, i\omega_\lambda - i\omega_N) \\ &= -\int\frac{\mathrm{d}^3 q}{(2\pi)^3} u_q v_q\Big[\frac{1+b(E_q)}{i\omega_\lambda - E_q - \epsilon_{p-q}} + \frac{b(E_q)}{i\omega_\lambda + E_q - \epsilon_{p-q}}\Big],\end{aligned} \tag{5.19}$$

where $b(E_q) = [e^{E_q/T}-1]^{-1}$ is the Bose distribution function, and we also have $\Pi_{21}(\boldsymbol{p}, i\omega_\lambda) = \Pi_{12}(\boldsymbol{p}, i\omega_\lambda)$. Again, the initial ultraviolet divergence of Π_{11} has been removed by relating the bare scattering potential V to the vacuum scattering matrix $\mathcal{T}_v$ as we did in Section 2.2.

Hence, the second order self-energy is given by

$$\begin{aligned}\Sigma_2(\boldsymbol{p}, i\omega_\lambda) &= n_0\mathcal{T}_v^2\big[\Pi_{11}(\boldsymbol{p}, i\omega_\lambda) + \Pi_{22}(\boldsymbol{p}, i\omega_\lambda) + 2\Pi_{12}(\boldsymbol{p}, i\omega_\lambda)\big] \\ &= n_0\mathcal{T}_v^2\int\frac{\mathrm{d}^3 q}{(2\pi)^3}\Big[\frac{\epsilon_q^{\mathrm{B}}}{E_q}\Big(\frac{1+b(E_q)}{i\omega_\lambda - E_q - \epsilon_{p-q}} + \frac{b(E_q)}{i\omega_\lambda - E_q - \epsilon_{p-q}}\Big) + \frac{2m_r}{q^2}\Big],\end{aligned} \tag{5.20}$$

since $u_q^2 + v_q^2 - 2u_q v_q = \epsilon_q^{\mathrm{B}}/E_q$.

When solving Eq. (5.47) for the polaron energy to second order in a, we put in the zero energy solution $\omega = 0$, since the term is

already of order a^2. Thus, since we consider the zero momentum polaron we need to determine $\mathfrak{Re}[\tilde{\Sigma}_2(0,0)]$ in order to determine the second order energy shift. The equation determining the polaron energy to order thus reads

$$E_{\text{pol}} = n\mathcal{T}_v + \Sigma(0,0). \tag{5.21}$$

Furthermore, we consider zero temperature where the number of thermally excited bosons is zero, i.e. $b = 0$. The pair-propagators Eqs. (5.17) to (5.19) can then be evaluated analytically, yielding

$$\Pi_{11}(0,0) = \frac{m_{\text{B}}}{\sqrt{2}\pi^2\xi}\frac{\alpha}{\alpha+1}\left[1+\frac{\alpha-1}{\alpha+1}f(\alpha)\right], \tag{5.22}$$

$$\Pi_{22}(0,0) = -\frac{m_{\text{B}}}{\sqrt{2}\pi^2\xi}\frac{\alpha}{\alpha-1}\left[1-f(\alpha)\right], \tag{5.23}$$

$$\Pi_{12}(0,0) = \frac{m_{\text{B}}}{\sqrt{2}\pi^2\xi}\frac{\alpha}{\alpha+1}f(\alpha), \tag{5.24}$$

where $\xi = 1/\sqrt{8\pi n_0 a_{\text{B}}}$ is the coherence length of the BEC, $\alpha = m/m_{\text{B}}$ is the mass-ratio, and

$$f(\alpha) = \sqrt{\frac{\alpha+1}{\alpha-1}}\tan^{-1}\left(\sqrt{\frac{\alpha-1}{\alpha+1}}\right) \tag{5.25}$$

with the definition $\sqrt{-1} = i$. We note that $f(\alpha)$ as well as the pair propagators Eqs. (5.22) to (5.24) are well-defined in the equal mass limit $\alpha \to 1$ where $f(1) = 1$ and

$$\Pi_{11}(0,0) = \frac{1}{2}\frac{m_{\text{B}}}{\sqrt{2}\pi^2\xi}, \tag{5.26}$$

$$\Pi_{22}(0,0) = -\frac{1}{6}\frac{m_{\text{B}}}{\sqrt{2}\pi^2\xi}, \tag{5.27}$$

$$\Pi_{12}(0,0) = \frac{1}{2}\frac{m_{\text{B}}}{\sqrt{2}\pi^2\xi}. \tag{5.28}$$

Having evaluated the pair-propagators, we can easily determine the second order self-energy Eq. (5.20) for zero momentum and energy.

The total energy shift of the polaron to second order is then

$$E_{\text{pol}} = \Sigma_1 + \Sigma_2(0,0) = \frac{2\pi n}{m_r} a + A(\alpha)\frac{2\pi n_0}{m_r}\frac{a^2}{\xi}$$
$$= \frac{2\pi n}{m_r} a\left[1 + A(\alpha)\frac{a}{\xi}\right], \tag{5.29}$$

where

$$A(\alpha) = \frac{2\sqrt{2}}{\pi}\frac{1}{1-\alpha}\left[1 - \frac{2\alpha^2}{1+\alpha} f(\alpha)\right] \tag{5.30}$$

with the equal mass limit $A(1) = \frac{8\sqrt{2}}{3\pi}$. Eq. (5.29) gives the polaron energy to second order in a. We see that the second order term is suppressed by a factor a/ξ with respect to the first order term, and we shall see that the corresponding factor for the third order term is a^2/ξ^2. This shows that the small parameter of the perturbation theory is a/ξ.

In Appendix A.3 we show that $\mathfrak{Im}[\Sigma]$ is zero at zero temperature and for $p \leq p_c = mc$ with $c = \sqrt{n_0 \mathcal{T}_B / m_B}$ the speed of sound in the BEC. Hence, since we consider the zero momentum polaron, the self-energies are all real and we will drop explicitly writing $\mathfrak{Re}$ for the remaining part of this chapter.

We briefly note that the purely real self-energy for a polaron at zero temperature and momentum $p \leq p_c$ is in agreement with Landau's criterion for superfluidity and corresponds to an undamped polaron with infinite lifetime as discussed in Section 2.3.[106] A polaron with a very small momentum does not have enough energy to excite a Bogoliubov mode in the BEC and is hence undamped, while a polaron of momentum $p \geq p_c$ experiences momentum relaxation by exciting a Bogoliubov mode carrying away some of the polarons initial energy.[99]

2nd Order Compliance With the Fröhlich Hamiltonian

The zero temperature, second order self-energy can equally be derived using the Fröhlich Hamiltonian describing the system as an

[106] L. Landau. *Phys. Rev.*, **60**: 356–358, 1941.

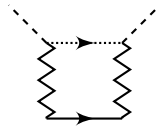

Figure 5.3: The second order self-energy diagram for an impurity interacting with BEC within the Fröhlich Hamiltonian. The full line is the propagator for the impurity, the dotted line is G_β, the dashed is a boson in the condensate and a zigzag line is the interaction $\mathcal{T}_v$.

impurity interacting with Bogoliubov modes in the BEC. We explicitly show this equality to second order perturbation between the two Hamiltonians in order to stress, where the Hamiltonians differ and the Fröhlich Hamiltonian fails to correctly describe an impurity in a Bose gas.

Ignoring the third term of the Hamiltonian Eq. (5.2) describing the scattering of the impurity with a boson completely out of the condensate and plugging in the Bogoliubov transformation, we can express the Hamiltonian as

$$\mathscr{H}_{\text{Fröh}} = \mathscr{H}_{\text{BEC}} + \sum_p (\epsilon_p + n_0 \mathcal{T}_v) c_p^\dagger c_p + \frac{\sqrt{N_0}\mathcal{T}_v}{\mathcal{V}} \sum_{p,q\neq 0} \sqrt{\frac{\epsilon_q^{\text{B}}}{E_q}} c_p^\dagger c_q \left(\beta_q^\dagger + \beta_{-q}\right)$$

which is the Fröhlich Hamiltonian (with the bare coupling replaced by $\mathcal{T}_v$) studied extensively throughout the literature.[101] It is the third term of Eq. (5.2) corresponding to the scattering vertex Fig. 5.1(d) of the impurity with a boson completely out of the condensate, which is ignored by the Fröhlich Hamiltonian.

However, since we ignore the second order contributions of these processes given by Figs. 5.2(e-f), the energy shift (as well as the remaining quasiparticle properties) to 2nd order, could just as well be calculated directly using the Fröhlich Hamiltonian. Introducing the Green's function for a Bogoliubov mode

$$G_\beta(\boldsymbol{p}, \tau) = -\left\langle \mathscr{T}\left\{\beta_p^\dagger(\tau)\beta_p(0)\right\}\right\rangle \tag{5.31}$$

with the Fourier transform $G_\beta(\boldsymbol{p}, i\omega_N) = [i\omega_N - E_p]^{-1}$, we can determine the self-energy from the diagram shown in Fig. 5.3, where

the dotted line corresponds to a propagating Bogoliubov mode. Evaluating the diagram, we get

$$\Sigma_2(\boldsymbol{p}, i\omega_\lambda) = n_0 \mathcal{T}_v^2 \int \frac{\mathrm{d}^3 q}{(2\pi)^3} \left[\frac{\epsilon_q^{\mathrm{B}}}{E_q} \left(\frac{1 + b(E_q)}{i\omega_\lambda - E_q - \epsilon_{p-q}} + \frac{b(E_q)}{i\omega_\lambda - E_q - \epsilon_{p-q}} \right) + \frac{2m_r}{q^2} \right],$$

again including the renormalization making the integral finite. We immediately see that this equation is equivalent to Eq. (5.20). Hence, to second order and at zero temperature our approach is equivalent to using the Fröhlich Hamiltonian and evaluating a Feynman diagram of the impurity interacting with a Bogoliubov mode. As mentioned above, this is because the second order terms neglected by the Fröhlich Hamiltonian are suppressed by a factor $(n_0 a_{\mathrm{B}}^3)^{1/2}$, and we therefore ignore these. The Fröhlich Hamiltonian has previously been used to determine the energy shift and effective mass of the polaron.[99,100] These results are in full agreement with the results presented in this thesis to second order.

The diagrams Figs. 5.2(e-f) or diagrams of third order, Fig. 5.4, can however not be reproduced using the Fröhlich Hamiltonian since the Fröhlich model does not contain the vertex shown in Fig. 5.1(d). The Fröhlich Hamiltonian is thus fundamentally wrong beyond zero temperature, second order perturbation theory for an impurity in a Bose gas.

5.3 ENERGY TO THIRD ORDER

We now turn our attention to the derivation of the Bose polaron energy to third order perturbation theory, where we show the third order self-energy Feynman diagrams in Fig. 5.4. The diagrams shown in Fig. 5.4(a) are second order diagrams with first order self-energy insertions for the polaron energy. The contribution from these diagrams are exactly cancelled by a third order term originating from inserting the first order energy shift into the second order self-energy Eq. (5.20). That is, to third order the equation for the

polaron energy Eq. (5.10) reads

$$E_{\rm pol} = n\mathcal{T}_v + \Sigma_2(0, n\mathcal{T}_v) + \Sigma_3(0,0) \tag{5.32}$$

where we have inserted the first order energy shift into the second order self-energy. One can show, as we sketch in Appendix A.2 that this equation is equivalent to

$$E_{\rm pol} = n\mathcal{T}_v + \Sigma_2(0,0) + \bar{\Sigma}_3(0,0) \tag{5.33}$$

where $\bar{\Sigma}_3$ is the third order self-energy with the diagrams Fig. 5.4(a) cancelled. As before we only consider diagrams to lowest order in $n_0 a_{\rm B}^3$ and ignore all diagrams of higher order, e.g. diagrams containing a boson loop.

Thus, we only consider the third order ladder diagrams shown in Fig. 5.4(b) and the crossed diagrams shown in Fig. 5.4(c), where we have introduced the effective Bose propagators

$$\begin{aligned} G_1(\boldsymbol{p}, i\omega_N) = G_2(\boldsymbol{p}, i\omega_N) &= G_{11}(\boldsymbol{p}, i\omega_N) + G_{12}(\boldsymbol{p}, i\omega_N) \\ &= \frac{u_p^2}{i\omega_N - E_p} - \frac{v_p^2}{i\omega_N - E_p} + \frac{u_p v_p}{i\omega_N + E_p} - \frac{u_p v_p}{i\omega_N - E_p}. \end{aligned} \tag{5.34}$$

Hence, inserting the effective propagators in Fig. 5.4(b), we obtain 8 diagrams with the standard Bose propagators Eqs. (5.7) to (5.9). Likewise, Fig. 5.4(c) can be expanded to 16 diagrams and we thus have 24 diagrams in total.

Going through the tedious evaluation of the diagrams Figs. 5.4(b-c), we end up with two third order self-energy terms

$$\begin{aligned} \Sigma_{3b}(\boldsymbol{p}, i\omega_\lambda) = n_0 \mathcal{T}_v^3 \Big[&\big(\Pi_{11}(\boldsymbol{p}, i\omega_\lambda) + \Pi_{12}(\boldsymbol{p}, i\omega_\lambda)\big)^2 \\ &+ \big(\Pi_{22}(\boldsymbol{p}, i\omega_\lambda) + \Pi_{12}(\boldsymbol{p}, i\omega_\lambda)\big)^2 \Big] \end{aligned} \tag{5.35}$$

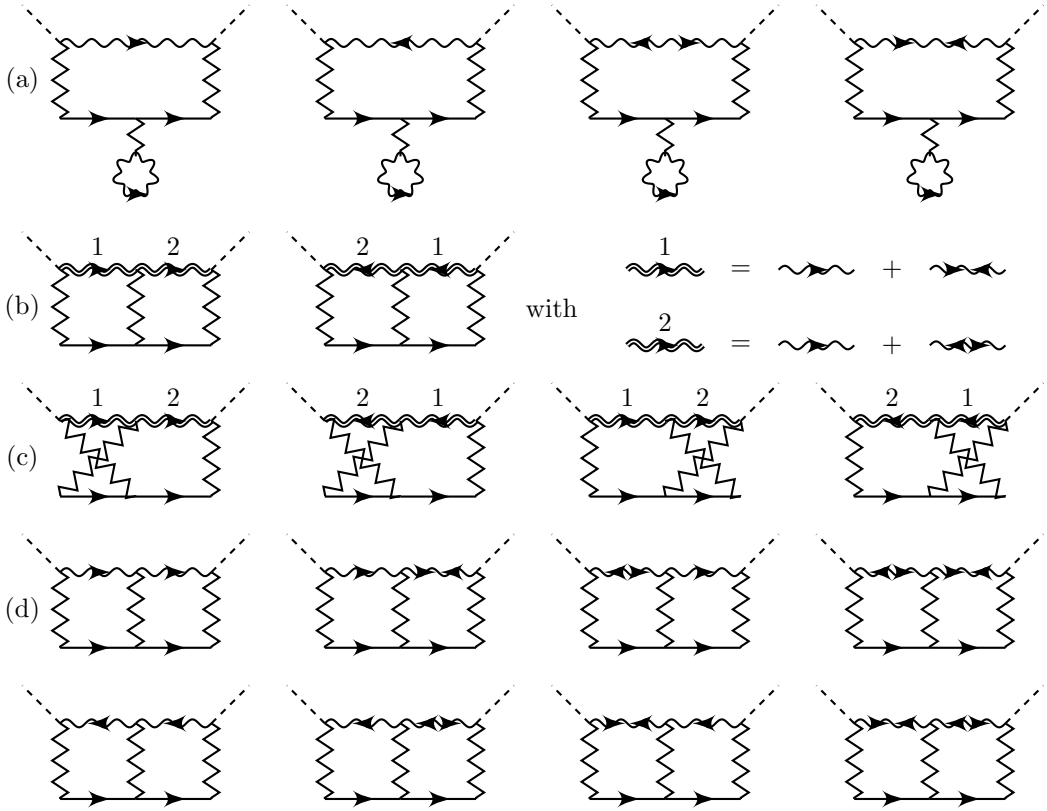

Figure 5.4: The third order self-energy diagrams for an impurity interacting with a Bose gas to lowest order in na_B^3. The particle lines are given by Eqs. (5.6) to (5.9), while the dashed is a boson in the condensate and a zigzag line is the interaction $\mathcal{T}_v$. Double lines are the effective propagators G_1 and G_2. By inserting G_1 and G_2 into the two diagrams in (b), the diagrams can be expanded to the 8 diagrams in (d).

from the ladder diagrams Fig. 5.4(b), and

$$\Sigma_{3c}(\boldsymbol{p}, i\omega_\lambda) = 2n_0\mathcal{T}_v^3 \times \int \frac{\mathrm{d}^3 q}{(2\pi)^3}\left[\frac{v_q^2 - u_q v_q}{i\omega_\lambda - E_q - \epsilon_{\boldsymbol{q}'}}\left(\Pi_{11}(\boldsymbol{q}', i\omega') + \Pi_{12}(\boldsymbol{q}', i\omega')\right) + \frac{u_q^2 - u_q v_q}{i\omega_\lambda - E_q - \epsilon_{\boldsymbol{q}'}}\left(\Pi_{22}(\boldsymbol{q}', i\omega') + \Pi_{12}(\boldsymbol{q}', i\omega')\right)\right] \tag{5.36}$$

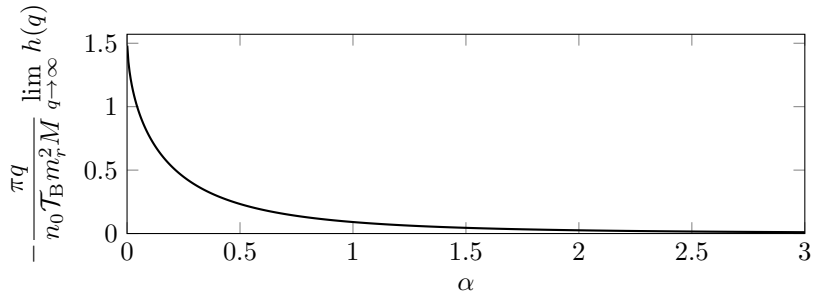

Figure 5.5: The $\lim_{q\to\infty} h(q)$ of Eq. (5.42) as a function of the mass ratio α. We see that it only asymptotically reaches zero for $\alpha \to \infty$.

from the crossed diagrams Fig. 5.4(c) with $\boldsymbol{q}' = \boldsymbol{p} + \boldsymbol{q}$ and $i\omega' = i\omega_\lambda - E_q$.

The zero momentum and energy pair-propagators are stated in Eqs. (5.22) to (5.24), while the remaining pair-propagators of finite momentum and energy appearing in Eq. (5.36) and derived in Appendix A.1, are

$$\Pi_{11}(\boldsymbol{q}, -E_q) = q m_B \frac{\alpha\sqrt{\alpha(2+\alpha)}}{2\pi(1+\alpha)^2}, \tag{5.37}$$

$$\Pi_{22}(\boldsymbol{q}, -E_q) \propto \frac{1}{q^2}, \qquad \text{(obtained numerically)} \tag{5.38}$$

$$\Pi_{12}(\boldsymbol{q}, -E_q) = \frac{1}{q}\frac{2m_B}{\xi^2}\frac{\alpha}{16\pi}\Big(\pi - 2\tanh^{-1}\big(\sqrt{\alpha(2+\alpha)}\big)\Big). \tag{5.39}$$

We now show that the third order crossed diagrams given by Σ_{3c} are in fact ultraviolet divergent. Initially, this came as a surprise, since we thought that by renormalising Π_{11} through 2-body physics, the theory would yield finite results order by order. However, noting that $u_q \to 1, v_q \to n_0 \mathcal{T}_B m_B / k^2$, and $E_q \to q^2/2m_B$ for $q \to \infty$, we

find that two terms of Eq. (5.36) are ultraviolet divergent, since

$$\lim_{q\to\infty}\frac{u_q v_q}{E_q+\epsilon_q}\Pi_{11}(\boldsymbol{q},-E_q)=\frac{n_0\mathcal{T}_{\mathrm{B}}m_r^2M}{\pi q^3}\frac{\sqrt{\alpha^2+2\alpha}}{(1+\alpha)^2}, \tag{5.40}$$

$$\lim_{q\to\infty}\frac{u_q^2}{E_q+\epsilon_q}\Pi_{12}(\boldsymbol{q},-E_q)=\frac{n_0\mathcal{T}_{\mathrm{B}}m_r^2M}{\pi q^3}\frac{(\pi-2\tan^{-1}\sqrt{\alpha^2+2\alpha})}{2}. \tag{5.41}$$

Thus, with the q^2 coming from the measure these terms in Eq. (5.36) diverges logarithmically for $q\to\infty$. Introducing

$$h(q)=q^2\frac{u_q v_q\Pi_{11}(\boldsymbol{q},-E_q)-u_q^2\Pi_{12}(\boldsymbol{q},-E_q)}{E_q+\epsilon_q}, \tag{5.42}$$

we show the relative behaviour of these divergences in Fig. 5.5 as a function of the mass ratio α. We see that the divergences never cancel for any finite value of the mass ratio α. Thus, Σ_{3_c} is ultraviolet divergent for all finite mass ratios.

We now analyse this divergence more carefully. First of all, all terms of Eqs. (5.35) and (5.36) are well-behaved at low momenta, where the boson dispersion become linear $E_p\sim\sqrt{n_0\mathcal{T}_{\mathrm{B}}/m_{\mathrm{B}}}p$. The natural scale where the integrals start to behave as stated in Eqs. (5.40) and (5.41) is $q\gtrsim 1/\xi$. Hence, we express Σ_3 using Eq. (5.42) as

$$\Sigma_3(0,0)=\frac{n_0\mathcal{T}_v^3}{\pi^2}\left[\int_0^\infty \mathrm{d}q\, h(q)-\int_{1/\xi}^\infty \mathrm{d}q\lim_{q\to\infty}h(q)+\int_{1/\xi}^\infty \mathrm{d}q\lim_{q\to\infty}h(q)\right]+\mathcal{O}(a^3), \tag{5.43}$$

where we have used that all the convergent terms of Σ_3 are of order $\mathcal{T}_v^3\sim\mathcal{O}(a^3)$. Now, the ultraviolet divergences for the first two terms of Eq. (5.43) cancel making these two terms finite and of order $\mathcal{O}(a^3)$. Thus, we have singled out the logarithmic diverging by writing

$$\Sigma_3(0,0)=\frac{n_0\mathcal{T}_v^3}{\pi^2}\int_{c_1/\xi}^\infty \mathrm{d}q\lim_{q\to\infty}h(q)+\mathcal{O}(a^3). \tag{5.44}$$

As mentioned, this divergence is not physical, but is a consequence of the fact that we have assumed constant scattering matrices $\mathcal{T}_{\mathrm{B}}$ and $\mathcal{T}_v$ in order to do perturbation theory. The true scattering matrices retaining the energy dependence shown in Eq. (2.7) behave as $1/q$ for $q \gtrsim 1/a_{\mathrm{B}}, 1/a$ respectively. Retaining this energy dependence for the scattering matrices, would introduce an ultraviolet cut-off in the integral of $q \sim 1/a$ for $\mathcal{T}_v$. Likewise retaining the energy dependence of $\mathcal{T}_{\mathrm{B}}$ would introduce a cut-off of $q \sim 1/a_{\mathrm{B}}$. Thus, retaining the energy dependence of the scattering matrices would make Σ_3 convergent. Hence, we introduce $1/a^*$ with $a^* = \max(a, a_{\mathrm{B}})$ as an upper cutoff for the remaining divergent integral and express Σ_3 as

$$\begin{aligned}\Sigma_3(0,0) &= \frac{n_0 \mathcal{T}_v^3}{\pi^2} \int_{1/\xi}^{1/a^*} \mathrm{d}q \lim_{q\to\infty} h(q) + \mathcal{O}(a^3) \\ &= B(\alpha)\frac{2\pi n_0}{m_r}\frac{a^3}{\xi^2}\ln\left(\frac{a^*}{\xi}\right) + \mathcal{O}(a^3), \end{aligned} \tag{5.45}$$

where

$$B(\alpha) = (1+\alpha)\left[1 - \frac{2}{\pi}\tan^{-1}\sqrt{\alpha^2+2\alpha}\right] - \frac{2\sqrt{\alpha^2+2\alpha}}{\pi(1+\alpha)}. \tag{5.46}$$

Thus, for $a > a_{\mathrm{B}}$ Σ_{3b} and the convergent terms of Σ_{3c} does not contribute to the order stated in Eq. (5.45), since they can be absorbed by a constant inside the logarithm.

Hence, we have solved Eq. (5.10) perturbatively to order $a^3\ln(a)$ and combining Eqs. (5.11), (5.29) and (5.45), we have for the zero momentum, zero temperature polaron in a BEC:

$$E_{\mathrm{pol}} = n_0 \frac{2\pi a}{m_r}\left[1 + A(\alpha)\frac{a}{\xi} + B(\alpha)\frac{a^2}{\xi^2}\ln\left(\frac{a^*}{\xi}\right)\right]. \tag{5.47}$$

We see that the natural expansion parameter beyond the first order energy shift is a/ξ, and we thus require $a/\xi \ll 1$ for our perturbation theory to be valid.

As stated above, the result to second order can equally be derived using the Fröhlich Hamiltonian, and our result is in full agreement

with this calculation.[99] The Fröhlich Hamiltonian does, however, not consider scattering events where both bosons are out of the condensate and, as we have seen here, these events lead to a third order logarithmic term. The Fröhlich Hamiltonian has been shown to lead to a fourth order logarithmic term, but fails in obtaining the third order logarithmic term, since it only generates even powers of a in a perturbation series.[98] Thus, the Fröhlich Hamiltonian completely misses the third order term and is thus fundamentally from for condensed matter systems.

Finally, we that setting $a = a_{\mathrm{B}}$ in Eq. (5.47), we obtain the same structure as for the energy of the weakly interacting Bose gas: schematically, $E \sim a\big(1+(na^3)^{1/2}+na^3\ln(na^3)+\mathcal{O}(na^3)\big)$ or by direct comparison, we have for the equal mass case $m = m_{\mathrm{B}}$:

$$E_{\mathrm{pol}} = \frac{4\pi na}{m}\Big[1+\frac{32}{3\sqrt{\pi}}(na^3)^{1/2}+4(\frac{2}{3}\pi-\sqrt{3})na^3\ln\big(na^3\big)+\mathcal{O}(na^3)\Big], \tag{5.48}$$

compared with the famous result for the energy of a weakly interacting Bose gas:[57,107–112]

$$\frac{E}{N} = \frac{2\pi na}{m}\Big[1+\frac{4}{5}\frac{32}{3\sqrt{\pi}}(na^3)^{1/2}+8(\frac{4}{3}\pi-\sqrt{3})na^3\ln\big(na^3\big)+\mathcal{O}(na^3)\Big]. \tag{5.49}$$

This illustrates the complexity of our calculation: Eq. (5.49) represents state-of-the-art of the perturbation theory for a weakly interacting Bose gas, as it goes one order beyond the celebrated Lee-Huang-Yang result and obtains the energy to the same order as Wu and Sawada.[57,107–112]

[107] T. D. Lee and C. N. Yang. *Phys. Rev.*, **105**: 1119–1120, 1957.
[108] T. D. Lee et al. *Phys. Rev.*, **106**: 1135–1145, 1957.
[109] K. A. Brueckner and K. Sawada. *Phys. Rev.*, **106**: 1117–1127, 1957.
[110] T. T. Wu. *Phys. Rev.*, **115**: 1390–1404, 1959.
[111] K. Sawada. *Phys. Rev.*, **116**: 1344–1358, 1959.
[112] N. M. Hugenholtz and D. Pines. *Phys. Rev.*, **116**: 489–506, 1959.

5.4 Quasiparticle Residue

Having obtained the energy up to and including third order in a, we will in addition to the energy also determine the quasiparticle residue and the effective mass for the Bose polaron. As we will see these results are well-defined and convergent to third order and hence, all the diagrams of Figs. 5.4(b-c) are explicitly included. The following derivation becomes rather technical, but we end with expressions for the quasiparticle residue and the effective mass given by Eqs. (5.59) and (5.69).

The quasiparticle residue for a zero momentum polaron was introduced in Section 2.3 and defined by Eq. (2.16)

$$Z^{-1} = 1 - \partial_\omega \big(\Sigma(0,\omega)\big)\Big|_{\omega = E_{\text{pol}}}. \tag{5.50}$$

We immediately see that the first order energy shift $n\mathcal{T}_v$ is independent of energy and hence, does not contribute to the quasiparticle residue. Furthermore, there is a third order contribution from inserting the first order energy shift into Σ_2, but this again cancels with the contribution from evaluating the diagrams shown in Fig. 5.4(a), see Appendix A.2. Thus, in order to determine the quasiparticle residue, we include the second order Figs. 5.2(a-d) as well as the third order ladder and crossed diagrams Figs. 5.4(b-c) in the self-energy Σ. We then end up with

$$Z^{-1} = 1 - \partial_\omega \big(\Sigma_2(0,\omega) + \Sigma_{3b}(0,\omega) + \Sigma_{3c}(0,\omega)\big)\Big|_{\omega=0}, \tag{5.51}$$

where Σ_2, Σ_{3b}, and Σ_{3c} are given by Eqs. (5.20), (5.35) and (5.36).

As can be seen from Eqs. (5.20) and (5.35), the quantities $\partial_\omega(\Pi_{11} + \Pi_{12})|_{(p,\omega)=(0,0)}$ and $\partial_\omega(\Pi_{22} + \Pi_{12})|_{(p,\omega)=(0,0)}$ appear multiple times, when evaluating $\partial_\omega(\Sigma_2 + \Sigma_{3b})|_{(p,\omega)=(0,0)}$. These quantities can be

determined analytically yielding

$$\partial_\omega\big(\Pi_{11}(0,\omega)+\Pi_{12}(0,\omega)\big)\Big|_{\omega=0} = -\int\frac{\mathrm{d}^3q}{(2\pi)^3}\frac{u_q^2-u_qv_q}{(E_q+\epsilon_q)^2}$$
$$= -\frac{m_\mathrm{B}\xi}{\sqrt{2}\pi^2}\frac{\alpha}{\alpha+1}\left[1+\frac{2\alpha}{\alpha+1}f(\alpha)\right], \tag{5.52}$$
$$\partial_\omega\big(\Pi_{22}(0,\omega)+\Pi_{12}(0,\omega)\big)\Big|_{\omega=0} = -\int\frac{\mathrm{d}^3q}{(2\pi)^3}\frac{v_q^2-u_qv_q}{(E_q+\epsilon_q)^2}$$
$$= -\frac{m_\mathrm{B}\xi}{\sqrt{2}\pi^2}\frac{\alpha}{\alpha-1}\left[1-\frac{2\alpha}{\alpha+1}f(\alpha)\right], \tag{5.53}$$

where $f(\alpha)$ is given by Eq. (5.25). Again, one has to take the $\alpha\to 1$ limit of the equations above, in order to obtain correct and meaningful results in the equal mass case.

Using these results, we obtain for the second order contribution to the quasiparticle residue

$$\partial_\omega\Sigma_2(0,\omega)\Big|_{\omega=0} = -\frac{1}{\sqrt{2}\pi}\frac{a^2}{a_\mathrm{B}\xi}\frac{\alpha+1}{\alpha-1}\left[1-\frac{2}{\alpha+1}f(\alpha)\right]. \tag{5.54}$$

Likewise, from taking the partial derivative of Eq. (5.35), we obtain

$$\partial_\omega\Sigma_{3b}(0,\omega)\Big|_{\omega=0} = \frac{1}{\pi^2}\frac{a^3}{a_\mathrm{B}\xi^2}\frac{\alpha+1}{\alpha}\left\{\left(\frac{\alpha+1}{\alpha-1}\right)^2\left[1-\frac{2\alpha}{\alpha+1}f(\alpha)\right]^2 - \left[1+\frac{2\alpha}{\alpha+1}f(\alpha)\right]^2\right\}. \tag{5.55}$$

Finally, we need to evaluate the partial derivative of the self-energy from the third order crossed diagram Eq. (5.36). This derivative evaluated at $\omega=0$ cannot be evaluated analytically, but has to be evaluated numerically for different mass ratios. The contribution from the third order crossed diagrams to the quasiparticle residue is given by

$$\partial_\omega\Sigma_{3c}(0,\omega)\Big|_{\omega=0} = \frac{1}{2\pi^2}\frac{a^3}{a_\mathrm{B}\xi^2}\left(\frac{\alpha+1}{\alpha}\right)^3 I_\omega(\alpha) \tag{5.56}$$

with

$$
\begin{aligned}
I_\omega(\alpha) = \int_0^\infty \mathrm{d}k \Bigg\{ & \\
& \frac{k^2 \mathscr{E}_k^{(-)}}{(\mathscr{E}_k + k^2/\alpha)^2} \int_0^\infty \mathrm{d}q \int_{-1}^1 \mathrm{d}t \left[\frac{q^2 \mathscr{E}_q^{(+)}}{\mathscr{E}_k + \mathscr{E}_q + (k^2+q^2-2kqt)/\alpha} - \frac{2\alpha}{1+\alpha} \right] \\
& + \frac{k^2 \mathscr{E}_k^{(-)}}{\mathscr{E}_k + k^2/\alpha} \int_0^\infty \mathrm{d}q \int_{-1}^1 \mathrm{d}t \, \frac{q^2 \mathscr{E}_q^{(+)}}{[\mathscr{E}_k + \mathscr{E}_q + (k^2+q^2-2kqt)/\alpha]^2} \\
& + \frac{k^2 \mathscr{E}_k^{(+)}}{(\mathscr{E}_k + k^2/\alpha)^2} \int_0^\infty \mathrm{d}q \int_{-1}^1 \mathrm{d}t \, \frac{q^2 \mathscr{E}_q^{(-)}}{\mathscr{E}_k + \mathscr{E}_q + (k^2+q^2-2kqt)/\alpha} \\
& + \frac{k^2 \mathscr{E}_k^{(+)}}{\mathscr{E}_k + k^2/\alpha} \int_0^\infty \mathrm{d}q \int_{-1}^1 \mathrm{d}t \, \frac{q^2 \mathscr{E}_q^{(-)}}{[\mathscr{E}_k + \mathscr{E}_q + (k^2+q^2-2kqt)/\alpha]^2} \Bigg\},
\end{aligned}
\tag{5.57}
$$

a dimensionless integral, and

$$
\mathscr{E}_p = \sqrt{p^2(p^2+1)}, \qquad \mathscr{E}_p^{(\pm)} = \frac{p^2 \pm \mathscr{E}_p}{\mathscr{E}_p}. \tag{5.58}
$$

Inserting these results into Eq. (5.51), we end up with

$$
Z^{-1} = 1 + C(\alpha) \frac{a^2}{a_\mathrm{B} \xi} + D(\alpha) \frac{a^3}{a_\mathrm{B} \xi^2}, \tag{5.59}
$$

where

$$
C(\alpha) = \frac{1}{\sqrt{2}\pi} \frac{\alpha+1}{\alpha-1} \left[1 - \frac{2}{\alpha} f(\alpha) \right], \tag{5.60}
$$

$$
\begin{aligned}
D(\alpha) = {} & \frac{\alpha+1}{\pi^2 \alpha} \left\{ \left(\frac{\alpha+1}{\alpha-1} \right)^2 \left[1 - \frac{2\alpha}{\alpha+1} f(\alpha) \right]^2 - \left[1 + \frac{2\alpha}{\alpha+1} f(\alpha) \right]^2 \right\} \\
& - \frac{1}{2\pi^2} \left(\frac{\alpha+1}{\alpha} \right)^3 I_\omega(\alpha).
\end{aligned}
\tag{5.61}
$$

Eq. (5.59) gives the quasiparticle residue of the polaron to third order in a. We see that contrary to the energy, the third order term for

the residue is finite and does not contain a logarithmic divergence. Eq. (5.59) leads to an important result: We immediately see that in order for the polaron to be well-defined, $Z \simeq 1$ we need $a^2/a_B\xi \ll 1$. Hence, this is an additional constraint along with $a/\xi \ll 1$ appearing in the energy for our perturbation theory.

5.5 EFFECTIVE MASS

The effective mass for a zero momentum polaron was also introduced in Section 2.3 and is defined by Eq. (2.17)

$$\frac{m}{m^*} = Z\Big(1 + 2m\,\partial_{p^2}\mathfrak{Re}[\Sigma(\boldsymbol{p}, E_{\text{pol}})]\Big|_{p=0}\Big). \tag{5.62}$$

Again, we have a cancellation of the third order diagrams Fig. 5.4(a) due to first order energy insertions in the second order self-energy.

The steps for obtaining the effective mass of the polaron are completely analogous to calculation of the residue, and we end up with the effective mass given by

$$\frac{m}{m^*} = Z\Big(1 + 2m\,\partial_{p^2}\big(\Sigma_2(\boldsymbol{p},0) + \Sigma_{3b}(\boldsymbol{p},0) + \Sigma_{3c}(\boldsymbol{p},0)\big)\Big|_{p=0}\Big). \tag{5.63}$$

Again, we start by stating

$$\begin{aligned}\partial_{p^2}\big(\Pi_{11}(\boldsymbol{p},0) + \Pi_{12}(\boldsymbol{p},0)\big)\Big|_{p=0} &= \int_0^\infty \mathrm{d}q\, \frac{k^2}{(2\pi)^2 m}\frac{u_q^2 - u_q v_q}{(E_q + \epsilon_q)^3}\Big[E_q - \frac{\epsilon_q}{3}\Big] \\ &= \frac{m_B\xi}{6\sqrt{2}\pi^2}\frac{1}{(\alpha+1)^2(\alpha-1)}\Big[3\alpha^2 - 4\alpha - 1 + \frac{2\alpha(3\alpha^2 - 2\alpha + 1)}{\alpha+1} f(\alpha)\Big],\end{aligned} \tag{5.64}$$

$$\begin{aligned}\partial_{p^2}\big(\Pi_{22}(\boldsymbol{p},0) + \Pi_{12}(\boldsymbol{p},0)\big)\Big|_{p=0} &= \int_0^\infty \mathrm{d}q\, \frac{k^2}{(2\pi)^2 m}\frac{v_q^2 - u_q v_q}{(E_q + \epsilon_q)^3}\Big[E_q - \frac{\epsilon_q}{3}\Big] \\ &= \frac{m_B\xi}{6\sqrt{2}\pi^2}\frac{1}{(\alpha+1)(\alpha-1)^2}\Big[3\alpha^2 + 4\alpha - 1 + \frac{2\alpha(3\alpha^2 + 2\alpha + 1)}{\alpha+1} f(\alpha)\Big],\end{aligned} \tag{5.65}$$

which appears in Σ_2 and Σ_{3b}. Again, we have to take the $\alpha \to 1$ limit in order to get the correct results for the equal mass case.

Continuing, the contributions to the effective mass from the second order and third order ladder diagrams are given by

$$2m\,\partial_{p^2}\Sigma_2(\boldsymbol{p},0)\Big|_{p=0} = \frac{1}{\sqrt{2}\pi}\frac{a^2}{a_B\xi}\frac{1}{(\alpha-1)^2}\left[1+\alpha^2-\frac{2(5\alpha^2+1)}{3(\alpha+1)}f(\alpha)\right],$$
$$2m\,\partial_{p^2}\Sigma_{3b}(\boldsymbol{p},0)\Big|_{p=0} = \frac{4}{3\pi^2}\frac{a^3}{a_B\xi^2}$$
$$\times\,\frac{(\alpha+1)^2(5\alpha^2+1)-2\alpha^2 f(\alpha)[3(\alpha+1)(\alpha^2+3)-4(2\alpha^2+1)f(\alpha)]}{(\alpha-1)^3(\alpha+1)^2}. \tag{5.66}$$

Again, the contribution from the third order crossed diagrams cannot be calculated analytically, but is given by

$$2m\,\partial_{p^2}\Sigma_{3c}(\boldsymbol{p},0)\Big|_{p=0} = \frac{1}{6\pi^2}\frac{a^3}{a_B\xi^2}\left(\frac{\alpha+1}{\alpha}\right)^3 I_{p^2}(\alpha) \tag{5.67}$$

with

$$
\begin{aligned}
I_{p^2}(\alpha) = \int_0^\infty \mathrm{d}k \Bigg\{ & \\
& \frac{4k^3}{\alpha(\mathscr{E}_k + k^2/\alpha)^2} \int_0^\infty \mathrm{d}q \int_{-1}^1 \mathrm{d}t \, \frac{q^2(k - qt)\left(\mathscr{E}_k^{(-)}\mathscr{E}_q^{(+)} + \mathscr{E}_k^{(+)}\mathscr{E}_q^{(-)}\right)}{[\mathscr{E}_k + \mathscr{E}_q + (k^2 - 2kqt + q^2)/\alpha]^2} \\
& - \frac{k^2[3\mathscr{E}_k - k^2/\alpha]}{[\mathscr{E}_k + k^2/\alpha]^3} \int_0^\infty \mathrm{d}q \int_{-1}^1 \mathrm{d}t \Bigg[\frac{q^2\mathscr{E}_k^{(-)}\mathscr{E}_q^{(+)} + q^2\mathscr{E}_k^{(+)}\mathscr{E}_q^{(-)}}{\mathscr{E}_k + \mathscr{E}_q + (k^2 - 2kqt + q^2)/\alpha} \\
& \qquad\qquad - \frac{2\alpha\mathscr{E}_k^{(-)}}{\alpha + 1} \Bigg] \\
& + \frac{k^2}{\mathscr{E}_k + k^2/\alpha} \int_0^\infty \mathrm{d}q \int_{-1}^1 \mathrm{d}t \, \frac{q^2\left[\frac{k^2}{\alpha} + \left(\frac{2qt}{k} - 3\right)\left(\mathscr{E}_k + \mathscr{E}_q + \frac{q^2}{\alpha}\right)\right]}{[\mathscr{E}_k + \mathscr{E}_q + (k^2 - 2kqt + q^2)/\alpha]^3} \\
& \qquad\qquad \times \left(\mathscr{E}_k^{(-)}\mathscr{E}_q^{(+)} + \mathscr{E}_k^{(+)}\mathscr{E}_q^{(-)}\right) \Bigg\}.
\end{aligned}
\tag{5.68}
$$

Inserting this along with Eq. (5.59) into Eq. (5.63) and keeping terms up to third order, we end up with

$$
\frac{m^*}{m} = 1 + F(\alpha)\frac{a^2}{a_\mathrm{B}\xi} + G(\alpha)\frac{a^3}{a_\mathrm{B}\xi^2}, \tag{5.69}
$$

where

$$
\begin{aligned}
F(\alpha) &= -\frac{\sqrt{2}}{3\pi}\frac{3(\alpha+1) - 2(\alpha^2+2)f(\alpha)}{(\alpha+1)(\alpha-1)^2}, \\
G(\alpha) &= -\frac{1}{2\pi^2}\left(\frac{\alpha+1}{\alpha}\right)^3\left(I_\omega(\alpha) + \frac{1}{3}I_{p^2}(\alpha)\right) \\
&\quad + \frac{8}{3\pi^2}\left[\frac{\alpha^2+2}{(\alpha-1)^3} - \frac{3(\alpha+1)(3\alpha^2+1)f(\alpha) - 2\alpha^2(\alpha^2+5)[f(\alpha)]^2}{(\alpha+1)^2(\alpha-1)^3}\right].
\end{aligned}
\tag{5.70}
$$

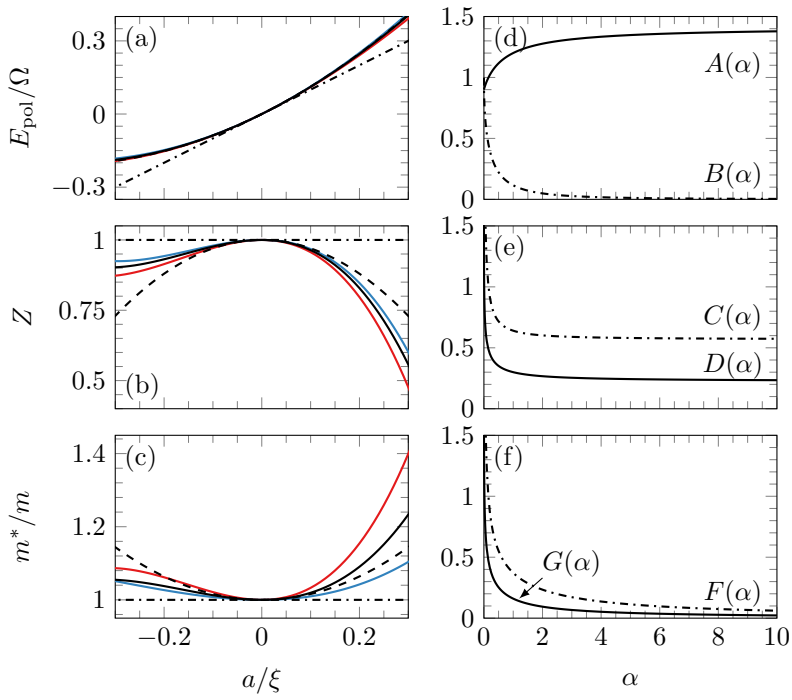

Figure 5.6: (left) The polaron energy E_{pol}, quasiparticle residue Z, and effective mass m^* as given by Eqs. (5.47), (5.59) and (5.69) for $a_{\mathrm{B}}/\xi = 0.1$ and $\Omega = 2\pi n\xi/m_r$. We show the first order term (dash-dotted), second order (dashed), and third order (solid) for equal masses (black). For $\alpha = 39/87$ (red) and $\alpha = 87/39$ (blue), we only show the third order result. (right) The relevant second and third order expansion coefficients $A(\alpha), \ldots, G(\alpha)$.

5.6 Quasiparticle Properties To Third Order

By systematically evaluating the 4 second order and 24 third order Feynman diagrams, we have successfully determined the energy, quasiparticle residue and effective mass of an interacting impurity emerged in a BEC, the Bose polaron up to third order in a. Our results, summarised by Eqs. (5.47), (5.59) and (5.69), are exact to third order and serve as an important benchmark for more complicated theories for the Bose polaron in the perturbative regime.

	$A(\alpha)$	$B(\alpha)$	$C(\alpha)$	$D(\alpha)$	$F(\alpha)$	$G(\alpha)$
$\alpha \to 0$	$\frac{2\sqrt{2}}{\pi}$	1	∞	∞	∞	∞
$\alpha = 1$	$\frac{8\sqrt{2}}{3\pi}$	$\frac{2}{3} - \frac{\sqrt{3}}{\pi}$	$\frac{2\sqrt{2}}{3\pi}$	$\frac{64}{9\pi^2} - 0.080$	$\frac{16\sqrt{2}}{45\pi}$	$\frac{448}{135\pi^2} - 0.059$
$\alpha \to \infty$	$\sqrt{2}$	0	$\frac{1}{\sqrt{2}\pi}$	$\frac{2}{\pi} - 0.068$	0	0

Table 5.1: Limiting values of the expansion coefficients for the energy, residue and effective mass.

Deriving the quasiparticle properties, we see two conditions enter for the validity of our perturbation theory. First off, the natural expansion parameter beyond the mean field shift for the energy is a/ξ, while it is $a^2/a_B\xi$ for the quasiparticle residue and the effective mass. Hence, we require both these parameters to be small in order to have a well-defined polaron with quasiparticle properties given by Eqs. (5.47), (5.59), (5.69) and (5.71).

In Figs. 5.6(a-c) we show our perturbative results for $a_B = 0.1\,\xi$ and different mass ratios, and we show the expansion coefficients $A(\alpha), \ldots, F(\alpha)$ as a function of the mass ratio $\alpha = m/m_B$ in Figs. 5.6(d-f).

Considering the energy of the polaron in Fig. 5.6(a) as well as the expansion coefficients $A(\alpha)$ and $B(\alpha)$ in Fig. 5.6(d), we have $E < 0$ ($E > 0$) for $a < 0$ ($a > 0$) corresponding to the attractive (repulsive) branch of the polaron energy. We see that beyond a mass ratio of $\alpha \sim 2$ the relative strength of the second and third order term are more or less constant compared with the mean field shift. We also see that except for a very light impurity $\alpha \ll 1$, the second order term completely dominates the third order term, even for $a \sim \xi$. In fact, the third order coefficient $B(\alpha)$ tends to zero for a very heavy impurity $\alpha \to \infty$ as seen in Table 5.1.

For the quasiparticle residue Z shown in Fig. 5.6(b), we see that the third order term plays a much larger role increasing (decreasing) the residue for the attractive (repulsive) polaron with respect to the second order residue. The same behaviour is seen in Fig. 5.6(e), where we see that the third order expansion coefficient $D(\alpha)$ dominates the

second order coefficient $C(\alpha)$ for all mass ratios. Finally, we again see that for impurities heavier than $\alpha \sim 2$, the expansion coefficients $C(\alpha)$ and $D(\alpha)$ are more or less constant yielding a finite value for $\alpha \to \infty$ as seen in Table 5.1.

For the effective mass shown in Fig. 5.6(c) the story is more or less the same, except that the third order term now decreases (increases) the effective mass of the attractive (repulsive) polaron with respect to the second order residue. The third order expansion coefficient dominates the second order coefficient for all mass ratios, but both $F(\alpha)$ and $G(\alpha)$ shown in Fig. 5.6(f) tends to zero for $\alpha \to \infty$. Hence, for a very heavy impurity the effective mass is simply equal to the bare mass of the impurity m.

We note that in limit of very light impurities $\alpha \to 0$, the expansion coefficients for the residue and effective mass $C(\alpha), \ldots, G(\alpha)$ all diverge, signalling a breakdown of perturbation theory. In this limit the majority atoms in the BEC are much heavier than the impurity atom, and it would be interesting to compare this with the problem of a mobile impurity interacting with static scatterers.[113,114]

From Figs. 5.6(d-f) it seems that we quickly reach a universal regime beyond $\alpha \sim 2-3$, where the relative weight of the second and third order does not change. Finally, we see that varying a/ξ changes the slope of the quasiparticle residue and effective mass in Figs. 5.6(b-c), but the results are qualitatively the same.

We see from Eqs. (5.59) and (5.69) as well as Fig. 5.6 that the second order shift for the quasiparticle residue and the effective mass is symmetric with respect to the sign of the scattering length a, whereas the third order term is asymmetric. Hence, if a measurement of the quasiparticle residue or the effective mass was realised this could provide crucial information for a quantitative comparison of the perturbation theory at different orders.

In addition to the quasiparticle properties determined above, the final property characterising the Bose polaron is the lifetime. As discussed, the polaron is stable for small momenta less than the critical momentum $p_c = mc$ with $c = \sqrt{n_0 \mathcal{T}_B / m_B}$ being the speed of sound

[113] P. W. Anderson. *Phys. Rev. Lett.*, **18**: 1049–1051, 1967.
[114] J. Kondo. *Progr. Theor. Phys.*, **32**: 37, 1964.

in the BEC, since it does not have energy to excite a Bogoliubov mode. To second order, we have rederived the lifetime of the Bose polaron in Appendix A.3[99]

$$\begin{aligned}\frac{1}{\tau_{p\geq p_c}} &= n_0 \mathcal{T}_v (1+\alpha)\frac{a}{\xi}\xi p \\ &\quad\times\left[g(\xi p)\sqrt{[g(\xi p)]^2+2}-2\sinh^{-1}\left(\frac{g(\xi p)}{\sqrt{2}}\right)\right] \\ &\overset{p-p_c\ll p_c}{=} n_0 \mathcal{T}_v \frac{4\sqrt{2}}{3\pi^2}(1+\alpha)\frac{a}{\xi}\frac{(\xi p-\xi p_c)^3}{\xi p_c}, \end{aligned} \tag{5.71}$$

where the second line applies for $p \geq p_c$ and $p - p_c \ll p_c$ and

$$g(x) = \frac{2\sqrt{2}}{1-\alpha^2}\left(x - \frac{\alpha}{\sqrt{2}}\sqrt{1-\alpha^2+2x^2}\right). \tag{5.72}$$

Impurity In an Ideal BEC

For an ideal BEC ($a_{\mathrm{B}} \to 0$), we have $\xi \to \infty$ and thus $a/\xi \to 0$. Hence, for an ideal BEC Eq. (5.47) signals that there are no corrections to mean field energy up to third order for an impurity in an ideal BEC. However, for an ideal BEC we also have $a^2/a_{\mathrm{B}}\xi \propto a_{\mathrm{B}}^{-1/2} \to \infty$ and thus, Eq. (5.59) indicates that $Z = 0$ and we have no well-defined polaron for an ideal BEC. Hence, our perturbation theory breaks down for an ideal BEC, which can also be seen by directly investigating our perturbative diagrams: For an ideal BEC, we have $u_p = 1$ and $v_p = 0$ and hence, only the regular Green's function $G_{11}(\boldsymbol{p}, i\omega_N) = 1/(i\omega_N - \epsilon_p^{\mathrm{B}})$ survive. It follows that only Π_{11} survives and reduces to the vacuum pair-propagator Eq. (3.6)

$$\Pi_{11}^{(0)}(\boldsymbol{p},\omega) = -i\frac{m_r^{3/2}}{\sqrt{2}\pi}\sqrt{\omega - \frac{p^2}{2M}}. \tag{5.73}$$

Thus, the self-energy to second order is then given by

$$\Sigma_2^{(0)}(\boldsymbol{p},\omega) = -i n_0 \mathcal{T}_v^2 \frac{m_r^{3/2}}{\sqrt{2}\pi}\sqrt{\omega - \frac{p^2}{2M}}. \tag{5.74}$$

We see directly that the $\sqrt{\omega}$ dependence of the self-energy means that the quasiparticle residue $Z \propto \left(\partial_\omega \Sigma\right)^{-1}$ vanishes at zero energy and momentum. At the same time, we have $\Pi_{11}^{(0)}(0,0) = 0$ and thus, all second and third order diagrams shown Figs. 5.2 and 5.4 are zero, since they either contain $\Pi_{11}^{(0)}$ or the reverse or anomalous propagators Π_{22} and Π_{12} which both vanish for an ideal BEC. This argument is in full agreement with taking the limit $\xi \to \infty$ of Eqs. (5.22) to (5.24).

Physically, this breakdown of perturbation theory occurs, since the energy of the impurity is right at the threshold of the particle-hole continuum of the BEC. Thus, equivalently, Landau's critical velocity $c = \sqrt{n_0 \mathcal{T}_B / m_B}$ goes to zero, and the zero energy polaron decays instantly by exciting the BEC. Thus, it is at the moment completely unknown whether a well-defined polaron exists in an ideal BEC.

Experimental Realisation of the Bose Polaron

As we will discuss in the following chapter, the Bose polaron has recently been realised experimentally, where the energy of the polaron has been measured in parallel works at Aarhus University, Denmark and at JILA, Colorado.[44,45] We have already discussed how to measure the energy through rf spectroscopy in Section 2.5.

The quasiparticle residue has been measured experimentally for the Fermi polaron, since it directly manifests itself in the Rabi frequency when doing Rabi flipping between the non-interacting and interacting impurity state.[42] Determining the quasiparticle residue of the Fermi polaron through Rabi flipping was possible due to an excellent overlap between the impurity and majority atoms, where the impurity atoms probed a central, approximately homogeneous part of the majority atoms as shown in Fig. 4.1. In principle, it should be possible to measure the quasiparticle residue in the same way for the Bose polaron, but for various reasons this is not possible with the current experimental realisations. At JILA, the impurity fermions

[45] M.-G. Hu et al. *Phys. Rev. Lett.*, **117**: 055301, 2016.
[42] C. Kohstall et al. *Nature*, **485**: 615–618, 2012.

probe a non-homogeneous BEC distribution, while the experiment at Aarhus University uses a single component BEC and then creates impurities by flipping some of the atoms to a different internal state as discussed in Section 2.5. This yields a perfect overlap between the impurity and majority atoms in the Aarhus experiment, excellent for measuring the energy shift of the polaron, but by continuously applying a resonant laser field, we would "Rabi flip" the whole cloud driving all of the majority atoms into the impurity state. Finally, measuring the effective mass and the lifetime of the Bose polaron would require the creation of polarons in a well-defined momentum state with finite momentum, or a clever way of averaging the theory in order to compare them with experiments. The creation of polarons with well-defined finite momentum poses a big experimental challenge, where none of the current experiments are able to do so. A possibility could be to use a setup with two Bose-Einstein condensates, where one of the condensates acts as impurity atoms and is excited to finite momentum. This, however, still poses a great experimental challenge and would also require a substantial amount of work for comparison between theory and experiment.

CHAPTER

6 Observation of the Bose Polaron

This chapter discusses how to relate the Bose polaron perturbation theory to the experimental observation of the Bose polaron at Aarhus University. As the previous chapter it builds on work published in Refs. [44, 54]. As mentioned, the work on the Bose polaron is contained completely within the PhD and does not draw on any work done in my Master's thesis.[76]

Recently, the Bose polaron, an interacting impurity in a Bose-Einstein condensate (BEC), was observed for the first time in parallel works at Aarhus University, Denmark and JILA, Colorado.[44,45] Various theoretical treatments of the Bose polaron have been put forward, but in this chapter we focus on relating the perturbation theory discussed in the previous chapter to the observed signal in the Aarhus Experiment.[54,98–100,102,103]

[76] R. S. Christensen. *Collision Rate of Polarons*. Master's Thesis. Aarhus University, Aug. 2013.

[44] N. B. Jørgensen et al. *Phys. Rev. Lett.*, **117**: 055302, 2016.

[45] M.-G. Hu et al. *Phys. Rev. Lett.*, **117**: 055301, 2016.

[54] R. S. Christensen et al. *Phys. Rev. Lett.*, **115**: 160401, 2015.

[98] F. Grusdt et al. *Sci. Rep.*, **5**: 12124, 2015.

[99] W. Casteels and M. Wouters. *Phys. Rev. A*, **90**: 043602, 2014.

[100] H. Bei-Bing and W. Shao-Long. *Chin. Phys. Lett.*, **26**: 080302, 2009.

[102] J. Levinsen et al. *Phys. Rev. Lett.*, **115**: 125302, 2015.

[103] Y. E. Shchadilova et al. *Phys. Rev. Lett.*, **117**: 113002, 2016.

As discussed in Section 2.5 rf spectroscopy directly probes the spectral function of the impurity atom. In this chapter we derive the expected spectral function starting from our perturbation theory and then relate this to the experimentally measured signal.

As mentioned, the Aarhus experiment starts with a single component BEC and then flips some of the atoms into the impurity state. Thus, the impurity atoms are also bosonic of nature. In the following we refer to majority atoms as bosons, while we refer to the minority atoms as impurities, since their quantum statistics does not matter in the limit of a lower concentration.

The objective of this chapter is twofold. We will provide an interpretation of the experimentally measured signal and justify that it really is a Bose polaron we observe. Secondly, we investigate whether we can experimentally observe effects beyond mean-field, but within our third order perturbation theory. Hence, does third order perturbation theory model the experiment significantly better than first order perturbation theory?

6.1 PARAMETERS OF THE AARHUS EXPERIMENT

Experimentally, the energy of a single Bose polaron in a homogeneous Bose-Einstein condensate (BEC) is not directly observable due to a number of reasons. For instance, the signal from a single impurity atom would be too weak to distinguish from experimental noise, a BEC in a trap is not homogeneous, the experiment is not performed at zero temperature, and so on. The signal obtained from rf spectroscopy does not simply probe the polaron, but probes the full spectral function including all possible excitations of the system as discussed in Section 2.5. Finally, the rf probe has a finite Fourier width which broadens the signal from the spectral function as shown in Fig. 2.7. As we will see below, including the spectral function beyond the polaron peak as well as the finite width of the rf pulse and the density inhomogeneity due to the trapping potential is important for interpreting the experimentally observed signal.

As discussed, the Aarhus experiment starts with a single BEC and then flips some of the atoms into a different hyperfine state, which

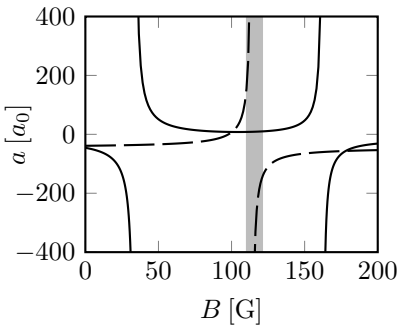

Figure 6.1: Feshbach resonance structure of the relevant states in ^{39}K for the Aarhus experiment. The full line is the scattering length a_{B} for the scattering in between atoms in the $|1\rangle$ state, while the dashed line is the scattering length a between atoms in states $|1\rangle$ and $|2\rangle$. The shaded area indicates the area, where measurements are performed.

then acts as the impurity state. The initial harmonically trapped BEC consists of ^{39}K atoms in the $|1\rangle = |F = 1, m_F = -1\rangle$ state, while the impurity state is $|2\rangle = |1, 0\rangle$, where F and m_F are the quantum numbers for the hyperfine levels in the atom. The structure of the Feshbach resonances for the relevant states is shown in Fig. 6.1.[44] We see from the figure that the Bose-Bose scattering length a_{B} is more or less constant within the experimental range, whereas the impurity-Bose scattering length a can be varied by orders of magnitude due to the presence of a Feshbach resonance at $B = 113.8\,\mathrm{G}$. This is extremely useful for studying the Bose polaron, as a can be varied while a_{B} is kept approximately constant.

In Table 6.1 we show the parameters for the Aarhus experiment.[44] Since the number of atoms fluctuates between experimental runs and the Bose-Bose scattering length changes slightly when the Bose-Impurity scattering length a is changed, we show averaged quantities in Table 6.1. Since the impurity atoms are initially flipped from the BEC, we have a perfect spatial overlap between the impurities and the majority atoms in the BEC. In order to quantify the interaction strength, we define a BEC density averaged over the majority atoms

as

$$\langle n_0 \rangle_{\text{trap}} = \frac{1}{N} \int \mathrm{d}^3 r \left(n(\boldsymbol{r}) \right)^2 = \frac{4\sqrt{2 m_{\text{B}} \mu}}{105 N \pi a_{\text{B}}^2} \left(\frac{\mu}{\bar{\omega}} \right)^3 , \tag{6.1}$$

where N is the total number of atoms initially in the BEC, $\bar{\omega} = (\omega_x \omega_y \omega_z)^{1/3}$ is the geometric mean of the trapping frequencies, and $n(\boldsymbol{r}) = (\mu - V_{\text{trap}}(\boldsymbol{r}))/\mathcal{T}_{\text{B}}$ is the local density of the BEC in the trap within the Thomas-Fermi approximation with

$$\mu = \frac{\bar{\omega}}{2} \left(15 N a_{\text{B}} \sqrt{m_{\text{B}} \bar{\omega}} \right)^{2/5} \tag{6.2}$$

the chemical potential for the bosons and $V_{\text{trap}}(\boldsymbol{r})$ the trapping potential.[55,115] Inspired by the Fermi wave number, we define $k_n = (6\pi^2 \langle n_0 \rangle_{\text{trap}})^{1/3}$ and $E_n = k_n^2 / 2 m_{\text{B}}$, which we use as units of momentum and energy respectively. Finally, we note that the temperature of the Bose gas is $T = 0.6\, \mathrm{T}_c$, where T_c is the critical temperature of the BEC. However, since the condensate fraction in a harmonic trapping potential is $N_0/N = [1 - (T/T_c)^3]$, we still have about 80 % of the bosons in the BEC.

6.2 SPECTRAL SIGNAL FROM PERTURBATION THEORY

In this section we model the experimental signal and discuss how to extract the energy of the polaron from the signal. We start from our perturbation theory discussed in the previous chapter, and relate the ideal rf spectroscopy discussed in Section 2.5 to the experimental setting, where inhomogeneity and spectral width of the rf probe broadens the obtained signal.

For reference we state the polaron energy and quasiparticle residue within third order perturbation theory in terms of the local

[55] C. Pethick and H. Smith. *Bose-Einstein Condensation in Dilute Gases*. Cambridge University Press, 2002.

[115] F. Dalfovo et al. *Rev. Mod. Phys.*, **71**: 463–512, 1999.

$\langle N \rangle$	$= (1.88 \pm 0.28) \times 10^4$	$\langle n_0 \rangle_{\text{trap}}$	$= (2.27 \pm 0.14) \times 10^{20}\,\text{m}^{-3}$
T	$= 160\,\text{nK}$	T/T_c	$= 0.6$
$\bar{\omega}$	$= 1.14 \times 10^3\,\text{s}^{-1}$	$\bar{\omega}/E_n$	$= 2.48 \times 10^{-3}$
FWHM_{rf}	$= 10\,\text{kHz}$	σ_{rf}/E_n	$= 0.0804$
$\langle a_{\text{B}} \rangle$	$= (8.62 \pm 0.43)\,a_0$	$k_n \langle a_{\text{B}} \rangle$	$= 0.011$
$\langle \mu \rangle / E_n$	$= 8.05 \times 10^{-3}$	$k_n \xi$	$= 14.7$

Table 6.1: Experimental values for the Bose polaron experiment at Aarhus University.[44] $\langle N \rangle$ is the average number of atoms initially in the BEC for all experimental runs, $\langle n_0 \rangle_{\text{trap}}$ is the trap averaged density as given by Eq. (6.1), T is the temperature, T_c is the critical temperature of Bose-Einstein condensation, $\bar{\omega} = (\omega_x \omega_y \omega_z)^{1/3}$ is the geometric mean of the trapping frequencies, FWHM_{rf} is the full width at half maximum of the 100 μs square rf pulse in frequency space, $\sigma_{\text{rf}} = \text{FWHM}_{\text{rf}}/2\sqrt{2\ln 2}$, $\langle a_{\text{B}} \rangle$ is the mean Bose-Bose scattering length averaged over all experimental runs, $\langle \mu \rangle$ is the mean chemical potential of the BEC within the Thomas-Fermi approximation, while $\xi = (8\pi \langle n_0 \rangle_{\text{trap}} \langle a_{\text{B}} \rangle)^{-1/2}$. $k_n = (6\pi^2 \langle n_0 \rangle_{\text{trap}})^{1/3}$ and $E_n = k_n^2 / 2m_{\text{B}}$. The errors shown are the $1\,\sigma$ standard deviations.

density of the BEC. Re-expressing Eqs. (5.47) and (5.59) we have

$$E_{\text{pol}}(\boldsymbol{r}) = \mathcal{T}_v n(\boldsymbol{r}) \Big[1 + A(\alpha) \sqrt{8\pi n(\boldsymbol{r}) a_{\text{B}}}\, a + B(\alpha) 8\pi n(\boldsymbol{r}) a_{\text{B}} a^2 \ln\!\Big(\sqrt{8\pi n(\boldsymbol{r}) a_{\text{B}}}\, a^* \Big) \Big], \quad (6.3)$$

$$\big(Z(\boldsymbol{r}) \big)^{-1} = 1 + C(\alpha) \sqrt{\frac{8\pi n(\boldsymbol{r})}{a_{\text{B}}}}\, a^2 + D(\alpha) 8\pi n(\boldsymbol{r}) a^3 . \quad (6.4)$$

In the following, we use the local density approximation, where Eqs. (6.3) and (6.4) are assumed to give the polaron and quasiparticle residue locally at the position $\boldsymbol{r}$ in the trap.

As discussed in Section 2.5, the experimentally measured signal is a loss signal, where 30 % of the atoms initially in the BEC are lost at the resonance frequency. Since a single impurity recombines with two majority atoms and are lost, this corresponds to initially having 10 % of the atoms in the impurity state. The experimental signal from the rf spectroscopy is broadened due to non-homogeneity and

the finite width of the rf pulse. Furthermore the rf spectroscopy does not solely probe the polaron state, but probes the full spectral function including excitations above (and below for the repulsive polaron) the polaron state. In this section, we discuss the magnitude of these effects and how to compare our perturbative theory with the experiment.

Broadening Due to Trap And Finite Width RF Pulse

Assuming a perfect rf probe in frequency space with spectral function $\mathcal{A}_{\mathrm{rf}}(\omega) = \delta(\omega)$, we still expect a broadening of the obtained signal due density non-homogeneity of the BEC in the trapping potential. Hence, we expect the energy shift for a polaron to be largest at the center of trap, where the density is highest, while we expect the energy shift to go to zero, as the polaron approaches the edge of the BEC. Assuming a perfect rf probe and a polaron with unit quasiparticle residue and completely well-defined energy E_{pol}, such that the spectral function is $A_{\mathrm{pol}}(\omega) = 2\pi\delta(\omega - E_{\mathrm{pol}})$, we expect a signal

$$\begin{aligned} I_\delta(\omega) &= \frac{1}{N}\int \mathrm{d}^3 r\, n(\boldsymbol{r}) \frac{1}{2\pi}\int_{-\infty}^{\infty} \mathrm{d}\omega'\, \delta(\omega') 2\pi\delta\big(\omega - \omega' - E_{\mathrm{pol}}(\boldsymbol{r})\big) \\ &= \frac{1}{N}\int \mathrm{d}^3 r\, n(\boldsymbol{r})\delta\big(\omega - E_{\mathrm{pol}}(\boldsymbol{r})\big). \end{aligned} \tag{6.5}$$

In Eq. (6.5), we simply average the spectral response of the polaron over the whole BEC. We have chosen the normalisation of our line shape $I_\delta(\omega)$ such that $\int_{-\infty}^{\infty} \mathrm{d}\omega I_\delta(\omega) = 1$. In the weak-coupling regime where $E_{\mathrm{pol}}(\boldsymbol{r}) = n(\boldsymbol{r})\mathcal{T}_v$, we obtain for the line shape

$$I_{\mathrm{MF}}(\omega) = \frac{15}{4}\frac{1}{|\omega_0|}\frac{\omega}{\omega_0}\sqrt{1 - \frac{\omega}{\omega_0}}, \quad \text{for} \quad 0 \leq \frac{\omega}{\omega_0} \leq 1 \tag{6.6}$$

with $\omega = \mu\mathcal{T}_v/\mathcal{T}_{\mathrm{B}}$.

As mentioned, we do not have a perfect rf probe experimentally, but a square pulse of length $100\,\mu\mathrm{s}$. In frequency space this approximately corresponds to a Gaussian pulse with full width at

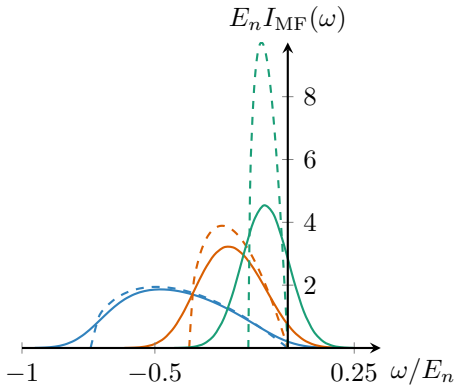

Figure 6.2: The expected line shape for probing a polaron in a Thomas-Fermi distributed BEC in the mean-field regime. We show the expected line shape with perfect resolution Eq. (6.6) (dashed) and for a Gaussian rf pulse with $\mathrm{FWHM}_{\mathrm{rf}} = 10\,\mathrm{kHz}$ (solid). The Gaussian rf pulse is given by Eq. (6.8) with $E_{\mathrm{pol}}(\boldsymbol{r}) = n(\boldsymbol{r})\mathcal{T}_v$. The experimental values are given in Table 6.1, and $1/k_n a = -1$ (green), $1/k_n a = -2$ (red), and $1/k_n a = -5$ (blue). The area under each curve integrates to 1.

half maximum (FWHM) 10 kHz and thus, a spectral function given by

$$\mathcal{A}_{\mathrm{rf}}(\omega) = \frac{1}{\sqrt{2\pi\sigma_{\mathrm{rf}}^2}} e^{-\frac{\omega^2}{2\sigma_{\mathrm{rf}}^2}}, \tag{6.7}$$

where $\sigma_{\mathrm{rf}} = \mathrm{FWHM}/2\sqrt{2\ln 2}$. Introducing the Gaussian rf probe while we still assume a polaron of unit residue, we expect an experimental signal of the form

$$I_{\mathrm{rf}}(\omega) = \frac{1}{N}\int \mathrm{d}^3 r\, n(\boldsymbol{r}) \frac{1}{\sqrt{2\pi\sigma_{\mathrm{rf}}^2}} e^{-\frac{(\omega - E_{\mathrm{pol}}(\boldsymbol{r}))^2}{2\sigma_{\mathrm{rf}}^2}}. \tag{6.8}$$

In Fig. 6.2 we show the expected line shape of the experimental signal for a perfect polaron with unit residue for respectively a perfect and a Gaussian rf probe for different interaction strengths. When we ignore the Fourier width of the rf probe, the signal extends from a

maximum energy shift corresponding to an impurity in the center of the cloud to zero frequency corresponding to an impurity at the edge of the BEC. As we see from Fig. 6.2 and Eq. (6.6) the line shape ignoring the Fourier width of the rf probe scale as $\propto \omega\sqrt{1-\omega/\omega_0}$ (in the weak-coupling regime) and thus, have a rather sharp cutoff for the maximal energy shift at the center of the trap.

This sharp feature would be a nice way of obtaining the energy shift at the center of the trap experimentally, which could then be compared with theory. However, when the finite Fourier width of the rf probe is included this feature vanishes as the signal is dominated by the finite width of the rf probe as seen in the figure. Thus, we cannot directly obtain the energy shift of the polaron at the center of the trap and compare with theory.

Polaron Energy From Line Shape

Since the Aarhus experiment have perfect spatial overlap between the impurities and the BEC, we can define the averaged energy shift of the polaron as

$$\langle E_{\mathrm{pol}}\rangle = \int_{-\infty}^{\infty} \mathrm{d}\omega\, \omega I(\omega) \tag{6.9}$$

with $I(\omega)$ the resulting line shape after convolution of the polaron spectral function with the rf probes spectral function and trap averaging. Assuming a polaron with unit residue and a perfect rf probe we insert $I_\delta(\omega)$ Eq. (6.5) along with the polaron energy to third order Eq. (5.47) to obtain

$$\begin{aligned}\langle E_{\mathrm{pol}}\rangle &= \int_{-\infty}^{\infty} \mathrm{d}\omega\, \omega I_\delta(\omega) = \frac{1}{N}\int n(\boldsymbol{r}) E_{\mathrm{pol}}(\boldsymbol{r}) \\ &= \frac{4}{7}\mu\frac{\mathcal{T}_v}{\mathcal{T}_{\mathrm{B}}}\Bigg[1+\frac{525\pi}{2048}A(\alpha)\sqrt{2m_{\mathrm{B}}\mu}\,a \\ &\qquad -\frac{4}{3}B(\alpha)m_{\mathrm{B}}\mu\, a^2\Big(\frac{1097}{1260}-\log\big(2\sqrt{2m_{\mathrm{B}}\mu}a^*\big)\Big)\Bigg].\end{aligned} \tag{6.10}$$

Comparing the averaged mean field energy shift (the first term above) with the homogeneous mean field result $E_{\mathrm{pol}}^{\mathrm{MF}} = n\mathcal{T}_v$, we have

$$\frac{E_{\mathrm{pol}}^{\mathrm{MF}}}{\langle E_{\mathrm{pol}}^{\mathrm{MF}}\rangle} = \frac{n\mathcal{T}_v}{\frac{4}{7}\mu\frac{\mathcal{T}_v}{\mathcal{T}_{\mathrm{B}}}} = \frac{7}{3\pi}\frac{k_n a_{\mathrm{B}}}{\mu/E_n} \approx 1.01\,, \tag{6.11}$$

where we have plugged in the averaged quantities $k_n\langle a_{\mathrm{B}}\rangle$ and $\langle\mu\rangle/E_n$ from Table 6.1. Hence, the average polaron energy is very close to the value obtained by simply inserting the average density $\langle n_0\rangle_{\mathrm{trap}}$ into Eq. (6.3). Up to third order we still numerically obtain $E_{\mathrm{pol}} \approx \langle E_{\mathrm{pol}}\rangle$ (not shown) except very close to unitarity.

Experimentally, a Gaussian is fitted to the loss signal and the polaron detuning or energy shift $\Delta = \omega_{\mathrm{rf}} - \omega_0$ is determined as the center of the fitted Gaussian. Here, ω_0 is the transition frequency in the absence of interactions as discussed in Section 2.4 and ω_{rf} the frequency of the rf probe. The fitted Gaussian thus corresponds to a fitted line shape $I(\omega)$, since the rf pulse probes the spectral function. For a Gaussian line shape the average energy as given by Eq. (6.9) simply corresponds to the center of the Gaussian.

As we will we see in Fig. 6.5, the line shape obtained from theory is not necessarily symmetric, and in order to compare quantitatively with the experiment, we fit a Gaussian to the theoretical line shape and extract the polaron energy from the fit.

Line Shape From Perturbation Theory

The simplest way of obtaining a line shape from theory is to assume a perfect polaron with unit quasiparticle residue and then plug the density dependent third order energy shift into Eq. (6.8). Hence, we assume a polaron with a δ-function spectral function, where the experimental signal is then broadened due to density inhomogeneity and the finite width of the rf probe.

However, by investigating the quasiparticle residue within third order perturbation theory, we can see that the assumption of a quasiparticle with unit residue is rather bad even for weak to moderate interactions in the Aarhus experiment. We show the quasiparticle

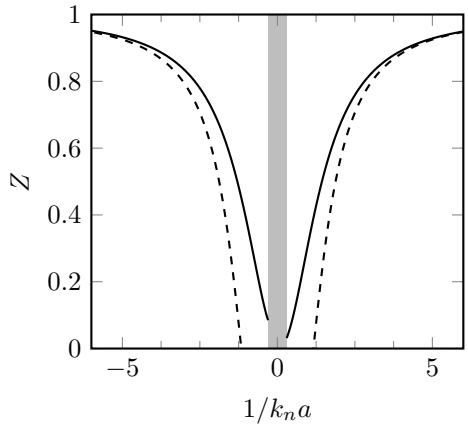

Figure 6.3: The quasiparticle residue obtained from the analytic expression Eq. (5.59) (full) and from the spectral function including the many-body continuum Eq. (6.16) (dashed). Both results use the averaged experimental parameters in Table 6.1.

residue assuming a homogeneous gas Eq. (5.59) using the averaged experimental parameters in Fig. 6.3. Here, we see that the residue quickly drops, since $a^2/a_B\xi \approx 6.2(k_n a)^2$ grows quickly with increasing $k_n a$ making the quasiparticle residue small. Hence, the spectral weight of the polaron δ-function part of the spectral function quickly declines as we approach unitarity. It follows that, we need to include the remaining part of the spectral function within our perturbative method to model the experiment.

As discussed in Section 2.3, we expect the full spectral function to consist of a quasiparticle peak resembling a δ-function with integrated weight Z as well as a many-body continuum part of different excitations with total integrated weight $1-Z$. The many-body continuum consists of a range of different excitations of the system, the most simple being an impurity atom travelling with momentum $\boldsymbol{p}$ plus a Bogoliubov mode with momentum $-\boldsymbol{p}$. If we hadn't shifted the energy of the impurity Green's function, the many-body continuums would start at $\omega = 0$, since this is the minimum energy required to create an impurity plus a Bogoliubov mode travelling in opposite directions. Physically, however, the many-body continuum

necessarily starts at the polaron energy, since a Bogoliubov mode can be excited with arbitrarily small energy and momentum. The simplest possible way to estimate this continuum is within second order perturbation theory, where we obtain a finite imaginary part of the self-energy. In order to ensure that the continuum of excitations starts right above the polaron peak, we shift the impurity Green's function inside the second order self-energy terms with the polaron energy such that we have $G(i\omega_\lambda) = [i\omega_\lambda - E_{\rm pol}]^{-1}$ for the zero momentum polaron. Plugging this Green's function into the second order diagrams Figs. 5.2(a-d) and setting $\mathfrak{Re}[\Sigma(\omega - E_{\rm pol})] \simeq E_{\rm pol}$ in agreement with our perturbative approach, we have for the full spectral function

$$A(\omega) \simeq 2\pi Z \delta(\omega - E_{\rm pol}) - \frac{2\mathfrak{Im}[\Sigma(\omega - E_{\rm pol})]}{(\omega - E_{\rm pol})^2 + (\mathfrak{Im}[\Sigma(\omega - E_{\rm pol})])^2} \tag{6.12}$$

with

$$\mathfrak{Im}[\Sigma(\omega)] = -\Theta(\omega) \frac{mn\mathcal{T}_v^2 \sqrt{mn\mathcal{T}_{\rm B}}}{4\pi} \frac{(\omega/n\mathcal{T}_{\rm B})^3}{(1+\omega/n\mathcal{T}_{\rm B})^{5/2}}, \tag{6.13}$$

which applies for the equal mass case $m = m_{\rm B}$ relevant for the Aarhus experiment. $\Theta(\omega)$ is the Heaviside step function and for details of the derivation we refer to Appendix A.4. Plugging Eq. (6.13) into Eq. (6.12), we obtain for the spectral function

$$A(\omega) = 2\pi Z \delta(\omega - E_{\rm pol}) - \Theta(\omega) A_{\rm exc}(\omega - E_{\rm pol}), \tag{6.14}$$

where, expressing $A_{\rm exc}$ in the experimentally relevant units of E_n and k_n, we have

$$A_{\rm exc}(\omega) = \frac{2}{E_n} \frac{\frac{2\sqrt{2}(k_n a)^2}{3\pi} \frac{(\omega/E_n)^3}{(4k_n a_{\rm B}/3\pi + \omega/E_n)^{5/2}}}{(\omega/E_n)^2 + \left(\frac{2\sqrt{2}(k_n a)^2}{3\pi} \frac{(\omega/E_n)^3}{(4k_n a_{\rm B}/3\pi + \omega/E_n)^{5/2}} \right)^2}. \tag{6.15}$$

In Fig. 6.4 we show the spectral function for 3 different interaction strengths. In the figure we have illustrated the δ-function peak as a

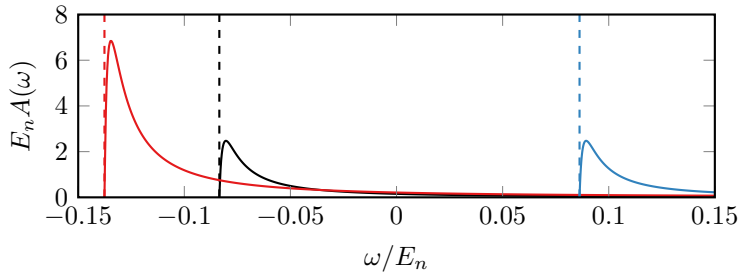

Figure 6.4: The spectral function including the many-body continuum within second order perturbation theory for $1/k_n a = -3$ (red), $1/k_n a = -5$ (black), and $1/k_n a = 5$ (blue). We have shifted the many-body continuum from zero energy to the polaron peak at E_{pol} as seen in Eq. (6.12).

dashed line, while the full lines are the many-body continuum above the polaron peak. We also see from Eq. (6.14) that the spectral weight of the continuum decreases as $\omega^{-3/2}$ for large energy $\omega \gg n\mathcal{T}_{\text{B}}$.

We require the spectral function to be normalised as given by Eq. (2.27), hence $\frac{1}{2\pi}\int_{-\infty}^{\infty} \mathrm{d}\omega A(\omega) = 1$. By plugging in Eq. (6.14), we could then define the quasiparticle residue Z through

$$1 - Z = \frac{1}{2\pi}\int_{-E_{\text{pol}}}^{\infty} \mathrm{d}\hat{\omega}\, A_{\text{exc}}(\hat{\omega}). \tag{6.16}$$

Hence, require the integrated spectral weight of the continuum to be $1-Z$. However, this way of calculating the quasiparticle residue Z yields a value inconsistent with the perturbative expression Eq. (5.59) as seen in Fig. 6.3. To fix this we rescale the weight of the continuum, such that our spectral function is correctly normalised. Hence, we express our spectral function as

$$A_{\text{con}}(\omega) = 2\pi Z\delta(\omega - E_{\text{pol}}) - \Theta(\omega)\tilde{A}_{\text{exc}}(\omega - E_{\text{pol}}, Z), \tag{6.17}$$

where

$$\tilde{A}_{\text{exc}}(\omega, Z) = \frac{1-Z}{\int_0^{\infty} \frac{\mathrm{d}\omega'}{2\pi} A_{\text{exc}}(\omega')} A_{\text{exc}}(\omega). \tag{6.18}$$

Thus, we use our perturbative result for the quasiparticle residue as the spectral weight of the polaron peak and then rescale the weight of the continuum such that the total weight of the spectral function integrates to 1. This ensures that the weight of the quasiparticle peak is correct as long as the third order perturbation theory is valid. The remaining spectral weight is then put into the many-body continuum.

We now have two ways of acquiring a theoretical line shape to compare with the experimental signal. The simplest way is to assume that the polaron has unit quasiparticle residue, convolute the polarons spectral function with the Gaussian spectral function of the rf probe and then finally average this result over the BEC. This method was discussed at the beginning of this section leading to a line shape given by Eq. (6.8). The second way is to include the many-body continuum within second order perturbation theory as derived above leading to the spectral function Eq. (6.17). We then convolute this spectral function with the Gaussian spectral function of the rf probe and average over the BEC ending up with a line shape given by

$$\begin{aligned} I_{\mathrm{con}}(\omega) &= \frac{1}{N}\int \mathrm{d}^3 r\, n(\boldsymbol{r}) \frac{1}{2\pi}\int_{-\infty}^{\infty} \mathrm{d}\omega' A_{\mathrm{con}}(\omega')\mathcal{A}_{\mathrm{rf}}(\omega-\omega') \\ &= \frac{1}{N}\int \mathrm{d}^3 r\, n(\boldsymbol{r}) \frac{Z(\boldsymbol{r})}{\sqrt{2\pi\sigma_{\mathrm{rf}}^2}} e^{-\frac{(\omega-E_{\mathrm{pol}}(\boldsymbol{r}))^2}{2\sigma_{\mathrm{rf}}^2}} \\ &\quad -\frac{1}{N}\int \mathrm{d}^3 r \frac{n(\boldsymbol{r})}{2\pi}\int_0^{\infty} \mathrm{d}\omega' \tilde{A}_{\mathrm{exc}}\big(\omega'-E_{\mathrm{pol}}(\boldsymbol{r}), Z(\boldsymbol{r})\big) \frac{e^{-\frac{(\omega-\omega')^2}{2\sigma_{\mathrm{rf}}^2}}}{\sqrt{2\pi\sigma_{\mathrm{rf}}^2}}, \end{aligned} \tag{6.19}$$

where $E_{\mathrm{pol}}(\boldsymbol{r})$ and $Z(\boldsymbol{r})$ are given within third order perturbation theory by respectively Eqs. (6.3) and (6.4), and the line shape is normalised such that $\int_{-\infty}^{\infty} \mathrm{d}\omega I_{\mathrm{con}}(\omega) = 1$.

As discussed, we finally extract the polaron energy by fitting a Gaussian to the line shapes given by Eqs. (6.5) and (6.19).

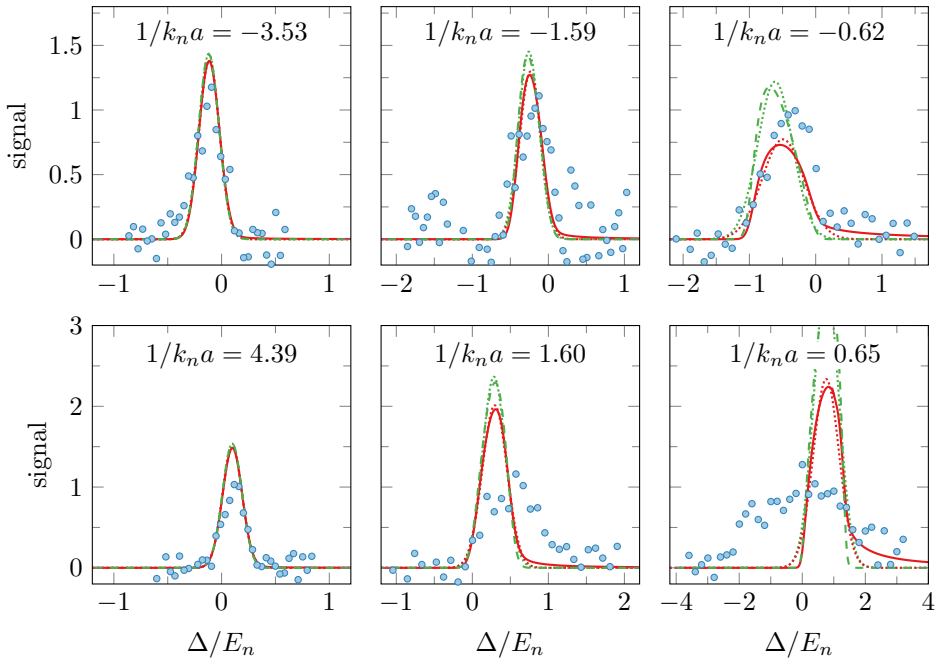

Figure 6.5: The raw spectral signal for the probing of impurities in the BEC at different interaction strengths along with the theoretical line shapes (full) assuming a perfect polaron with unit residue Eq. (6.5) (green) and including the many-body continuum Eq. (6.19) (red). The dotted lines are Gaussian fits to the theoretical line shapes.

6.3 RESULTS

Having derived the expected line shapes from perturbation theory, we are ready to compare with the Aarhus experiment. We start by comparing the line shapes directly with the experimentally obtained data in Fig. 6.5.[44] As discussed in Section 2.5 the experimental signal is normalised such that 30 % of the atoms initially in the BEC are lost at the resonance frequency for the polaron state. Hence, 10 % of the atoms initially in the BEC are transferred to the polaron state and are then lost through three-body recombination. In order to compare theory with experiment, we show the raw experimental data and then normalise the theoretical line shapes, such that the integrated

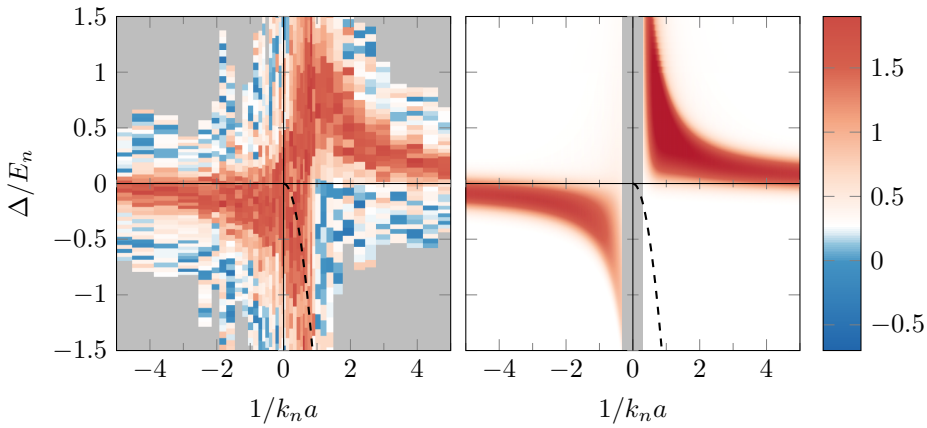

Figure 6.6: The spectral response of the impurity in the BEC. The false color plots show the experimental response (left) and the response calculated from perturbation theory including the many-body continuum (right) for different values of the detuning Δ and the interaction strength $1/k_n a$. The experimental spectrum is normalised such that its peak value is the same for all interaction strengths, while the theoretical spectrum is normalised such that the total spectral weight is the same as for the experimental spectrum.

spectral weight is the same as for the experimental spectrum.

We see from Fig. 6.5 that our theory curves agree well with the experimental data for weak interactions. This is a strong indication that the Aarhus group really sees a well-defined polaron. For stronger interactions the theoretical curves agrees reasonable well with the attractive polaron ($a < 0$), but not with the observed signal from the repulsive polaron ($a > 0$). Comparing the two theory curves, we see that the line shape including the many-body continuum Eq. (6.19) obtains a tail at higher energies, and that the peak of the fitted Gaussian is shifted a bit towards higher energies. Finally, we also see that the method of extracting the polaron energy by fitting a Gaussian to the theoretical line shapes seems to be reasonable, since the fitted Gaussians agree reasonable well with the theory curves.

In Figs. 6.6 and 6.7 we show the experimental spectrum along with the theoretical spectrum including the many-body continuum

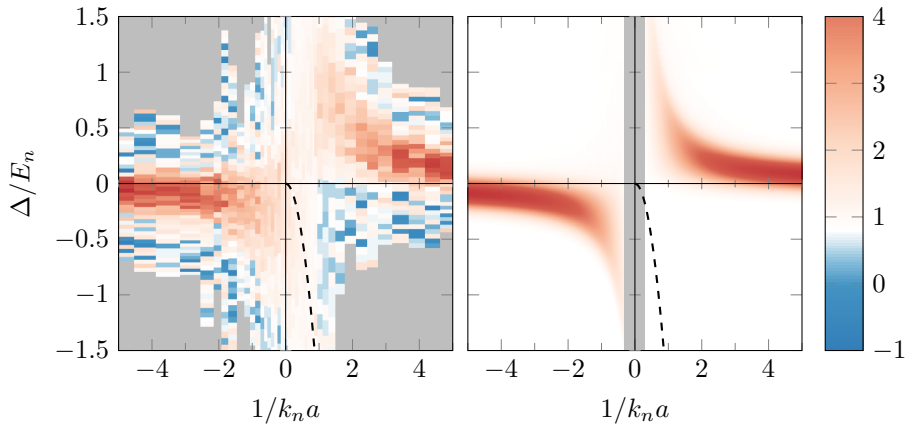

Figure 6.7: The spectral response for the impurity in the BEC. The false color plots show the experimental response (left) and the response calculated from perturbation theory including the many-body continuum (right) for different values of the detuning Δ and the interaction strength $1/k_n a$. Both spectra are normalised such that the integrated spectral weight is 1 for all interaction strengths.

obtained from Eq. (6.19) as a function of the inverse interaction strength. The figures differ just by the choice of normalisation. In Fig. 6.6 we use the experimental normalisation, where we show the raw signal obtained when the peak loss at the resonance frequency is kept constant at 30 % for all interaction strengths. The theory spectrum is then normalised such that the frequency integrated weight is the same as for the experimental spectrum. Hence, the frequency integrated weight varies with the interaction strength, but the height of the Gaussian fitted to the experimental spectrum is constant. In Fig. 6.7 we show exactly the same data, but here the spectra is scaled such that frequency integrated weight is 1 for all interaction strengths. This illustrates more clearly how the spectral weight of the many-body continuum dominates the polaron peak at strong interactions. Figs. 6.6 and 6.7 show that our perturbation theory reproduces the observed spectral response rather well for weak coupling. This kind of agreement was used as a strong argument for concluding that a well-defined Bose polaron was indeed observed for the first time.

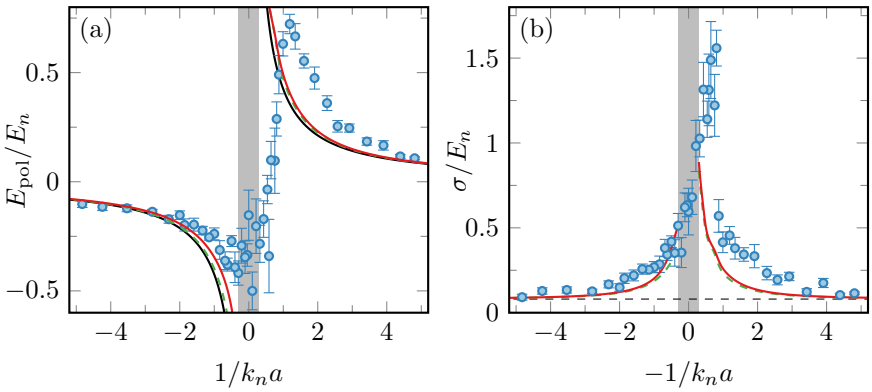

Figure 6.8: (a) The polaron energy E_{pol} and (b) the width σ of the impurity spectrum extracted from Gaussian fits to the experimental spectrum (blue points), the theoretical line shape assuming a perfect polaron with unit residue (green,dashed), and the theoretical line shape including the many-body continuum (red). The black line in (a) is the mean-field shift for an impurity in a homogeneous BEC.

For stronger interactions, the agreement is less good as expected.

Finally, we show in Fig. 6.8(a) the polaron energy extracted from Gaussian fits to the experimental as well as the theoretical spectra, while Fig. 6.8(b) shows the width of the fitted Gaussian. In Fig. 6.8(a) we also show the mean-field shift of a polaron in a homogeneous gas. Again, we see a good agreement between theory and experiment for weak to moderate interactions, while the agreement breaks down for stronger interactions as expected. Furthermore, we see that including second and third perturbation theory slightly improves the agreement between theory and experiment, but the effects aren't large.

Discussion And Conclusion

In Figs. 6.6 to 6.8, we saw a good agreement between theory and experiment for weak to moderate interactions, while the agreement broke down for stronger interactions as expected. We stress that by applying perturbation theory all the way into $1/k_n a = \pm 0.3$,

we have clearly entered a region where the perturbation theory is not valid. Even so, we see that perturbation theory captures the essence of the experimentally measured signal. We thus interpret the measured signal at weak interactions, as a well-defined polaron peak broadened by trapping effects and the finite resolution of the rf probe. For stronger interactions the signal grows wider due to excitations of the system in the many-body continuum as clearly seen in Fig. 6.7.

A weakness of our perturbation theory is that we model the polaron as the ground state of the system, which is not true for positive scattering length. As for the Fermi polaron, the impurity can at positive scattering lengths pair up with a majority boson to form a dimer at lower energies as indicated in Figs. 6.6 and 6.7. The experimental spectrum in Fig. 6.6 clearly has a significant part of the spectral weight at negative energies for $0 < 1/k_n a < 1$. An effect not captured at all in the theoretical spectrum of Fig. 6.6. Likewise, we see from Fig. 6.8 that the quantitative agreement between theory and experiment is reasonable for $1/k_n a \geq 3$ and $1/k_n a \leq -1$ for the polaron energy as well as the width of the fitted Gaussian. As mentioned already, this agreement for the width of the Gaussian strongly supports the interpretation that the signal in this regime arises from a polaron peak in spectral function, which is then widened due to the finite resolution of the rf probe as well as density inhomogeneity introduced by the trapping potential.

Finally, we see in Fig. 6.8(a) that including the many-body continuum for the theoretical spectral function does increase the energy of the polaron, but the effects are small compared to the homogeneous mean-field shift. Since the BEC is weakly interacting, the coherence length is long and we $k_n \xi \sim 15$ for this system, as stated in Table 6.1. Thus, even for relatively strong interactions $k_n a \sim 1$, our expansion parameter for the perturbative energy $a/\xi \sim 1/15$ is very small. A small expansion parameter is important for the validity of our perturbative theory, but being too small makes it difficult to distinguish between first and third order perturbation theory. Furthermore, the second expansion parameter appearing for the quasiparticle residue is $a/a_B \sim k_n a/0.011$, which grows large even for weak to moderate interactions. This means that the quasiparticle residue quickly drops

as we saw in Fig. 6.3. Hence, the experimental parameters of the Aarhus experiment are not the best suitable for verifying our third order perturbation theory, since it is difficult to distinguish the third order energy shift from the mean-field shift. Furthermore, the experiment is neither suitable for measuring the quasiparticle residue or effective mass as discussed at the end of the previous chapter.

We see from Eq. (6.2) that the chemical potential of the BEC scales with $a_{\mathrm{B}}^{2/5}$ and thus, the averaged density Eq. (6.1) scales with $a_{\mathrm{B}}^{-3/5}$ and k_n with $a_{\mathrm{B}}^{-1/5}$. Since $\xi \propto (na_{\mathrm{B}})^{-1/2}$ we have $k_n\xi \propto a_{\mathrm{B}}^{-2/5}$, $a/\xi \propto (k_n a)a_{\mathrm{B}}^{2/5}$, and $a/a_{\mathrm{B}} \propto (k_n a)a_{\mathrm{B}}^{-4/5}$. Since the two perturbative expansion parameters a/ξ and a/a_{B} scale differently with a_{B} it should in principle be possible to find a more suitable system for confirming the perturbation theory beyond mean field experimentally.

We end this chapter by concluding that there is a good agreement between our perturbative model for the Bose polaron and the observed signal. This provides a crucial argument for showing that the Bose polaron is indeed observed in the experiment. Thus, the Aarhus group has successfully probed the Bose polaron; a quasiparticle formed when an impurity is interacting with the BEC. For strong interactions, we motivated that the signal arises from excitations in the many-body continuum, but do not obtain quantitative agreement. For a better understanding and interpretation of the observed signal closer to unitarity, we refer to Refs. [44, 102, 103].

Furthermore, the experimental setup of the Aarhus experiment does not allow for a quantitative comparison of the Bose polaron energy at different orders of the perturbation theory, neither does it allow for the measurement of the quasiparticle residue or the effective mass. We conclude that including third order perturbation theory slightly improves the agreement between theory and experiment, but we do not have a quantitative comparison confirming our perturbative expansion of the energy.

CHAPTER

7 Conclusion And Outlook

Throughout this thesis we have considered interacting impurities in ultracold gases of fermionic or bosonic nature. We have seen how the impurities form quasiparticles coined polarons in the weak to moderate interaction regime. Our focus has been on developing robust theories for a better understanding of these systems as well as the quantitative modelling of specific experiments. We introduced the core theoretical concepts for modelling an interacting impurity in an ultracold gas, as well as the experimental method of radio frequency spectroscopy. Importantly, we have seen how radio frequency spectroscopy links directly to the spectral function, and how we can extract properties such as the decoherence rate and energy of the impurities using this method.

In the first half of this thesis, we focused on obtaining the scattering rate for an impurity emerged in a Fermi sea, the Fermi polaron. We calculated the scattering rate within Fermi liquid theory using the semi-classical Boltzmann transport equation. We saw how medium effects could significantly enhance the scattering rate due to the possibility of scattering through a Cooper resonance. Furthermore, we saw how including finite range effects for a ^{6}Li–^{40}K system relevant for an experiment performed by the group of R. Grimm quantitatively changed the obtained scattering rate significantly. The inclusion of finite range and medium effects proved crucial for the

quantitative modelling of the observed decoherence rate in the experiment performed by R. Grimm's group. Including these effects we successfully modelled the observed decoherence rate, proving it to be dominated by quasiparticle scattering for weak to moderate interactions.

The second half of the thesis focused on an interacting impurity emerged in a Bose-Einstein condensate, the Bose polaron. Here, we systematically expanded the energy, quasiparticle residue and effective mass perturbatively. We achieved exact results to third order in the impurity-Bose scattering length, results which will serve as benchmarks for more complicated theories. These results, which are state-of-the-art for the Bose polaron in condensed matter physics, proved that the Fröhlich model misses crucial physics and is fundamentally wrong beyond second order, zero temperature perturbation theory for this system. In the final chapter we successfully modelled the observed spectrum for impurities in Bose-Einstein condensate obtained by the group of J. Arlt at Aarhus University. We presented the first ever experimental observation of the Bose polaron and modelled the observed spectral response from the impurities, confirming that the interacting impurities in a Bose-Einstein condensate really do form quasiparticles.

Besides the results obtained, the work of this thesis has opened up a range of new questions, i.e. do a quasiparticle exist for an impurity in an ideal Bose-Einstein condensate? At the present moment joint theoretical and experimental work at Aarhus University looks into the temperature dependence of the Bose polaron's energy shift. In addition to this, it would be interesting to realise and model the Bose polaron in different condensed matter systems in order to determine the quasiparticle residue or quantitatively confirm differences between the orders of the perturbation theory.

APPENDIX

A Details

A.1 PAIR-PROPAGATORS OF FINITE MOMENTUM AND ENERGY

The regular pair-propagator at zero temperature is given by (see Eq. (5.17))

$$\begin{aligned}
\Pi_{11}(\boldsymbol{p},-E_p) &= \int\frac{\mathrm{d}^3q}{(2\pi)^3}\Big[\frac{\epsilon_q^{\mathrm{B}}+n_0\mathcal{T}_{\mathrm{B}}+E_q}{2E_q}\frac{1}{-E_p-E_q-\epsilon_{p-q}}+\frac{2m_r}{q^2}\Big]\\
&= -\frac{(4m_{\mathrm{B}}n_0\mathcal{T}_{\mathrm{B}})^{3/2}}{(2\pi)^2 2n_0\mathcal{T}_{\mathrm{B}}}\int_0^\infty\mathrm{d}q\,q^2\int_{-1}^1\mathrm{d}\cos\theta\Bigg[\\
&\qquad\frac{q^2+\frac{1}{2}+\sqrt{q^2(q^2+1)}}{(2\sqrt{q^2(q^2+1)})(\sqrt{p^2(p^2+1)}+\sqrt{q^2(q^2+1)}+\frac{p^2+q^2}{\alpha}+\frac{2pq}{\alpha}\cos\theta)}-\frac{\alpha}{1+\alpha}\frac{1}{q^2}\Bigg]\\
&= -\frac{\sqrt{2}m_{\mathrm{B}}}{(2\pi)^2\xi}\int_0^\infty\mathrm{d}q\Bigg[\\
&\qquad q\frac{q^2+\frac{1}{2}+\sqrt{q^2(q^2+1)}}{\sqrt{q^2+1}}\frac{\alpha}{2pq}\ln\left|\frac{\sqrt{p^2(p^2+1)}+\sqrt{q^2(q^2+1)}+\frac{(p+q)^2}{\alpha}}{\sqrt{p^2(p^2+1)}+\sqrt{q^2(q^2+1)}+\frac{(p-q)^2}{\alpha}}\right|-\frac{4\alpha}{1+\alpha}\Bigg]\\
&\overset{z=q/p}{=} -\frac{\sqrt{2}m_{\mathrm{B}}\alpha p}{(2\pi)^2\xi}\int_0^\infty\mathrm{d}q\Bigg[\\
&\qquad\frac{z^2+\frac{1}{2k^2}+z\sqrt{z^2+1/p^2}}{z\sqrt{z^2+1/p^2}}\ln\left|\frac{\sqrt{1+1/p^2}+z\sqrt{z^2+1/p^2}+\frac{(1+z)^2}{\alpha}}{\sqrt{1+1/p^2}+z\sqrt{z^2+1/p^2}+\frac{(1-z)^2}{\alpha}}\right|-\frac{4}{1+\alpha}\Bigg].
\end{aligned}$$

We approximate for $p \to \infty$ such that $z = \frac{q}{p} \gg \frac{1}{p}$ and $\sqrt{z^2 + 1/p^2} \approx z$. Hence,

$$\lim_{p\to\infty} \Pi_{11}(\boldsymbol{p}, -E_p) = -\frac{\sqrt{2} m_B \alpha p}{(2\pi)^2 \xi} \int_0^\infty \mathrm{d}z \left[z \ln \left| \frac{1 + z^2 + \frac{1+z^2}{\alpha}}{1 + z^2 + \frac{1-z^2}{\alpha}} \right| - \frac{4}{1+\alpha} \right]$$
$$= p m_B \frac{\alpha \sqrt{\alpha(2+\alpha)}}{2\pi(1+\alpha)^2}.$$

The calculation for $\Pi_{12}(\boldsymbol{p}, -E_p)$ is analogue, and we end up with

$$\lim_{p\to\infty} \Pi_{12}(\boldsymbol{p}, -E_p) = \frac{m_B \alpha}{8\pi \xi^2 p} \left(\pi - 2 \tan^{-1} \sqrt{\alpha(2+\alpha)} \right) \tag{A.1}$$

where we have used that

$$\int_0^\infty \mathrm{d}z \, z \ln \left| \frac{1 + z^2 + \frac{1+z^2}{\alpha}}{1 + z^2 + \frac{1-z^2}{\alpha}} \right| = \pi \left(\pi - 2 \tan^{-1} \sqrt{\alpha(2+\alpha)} \right). \tag{A.2}$$

The approximations made obtaining these results are equivalent to neglecting the and approximating $E_{p/q} \to \epsilon_{p/q}$.

A.2 Cancellation of Σ_{3a}

When solving the energy perturbatively to third order in Eq. (5.11) for the zero momentum polaron, we formally have to evaluate

$$\omega = n_0 \mathcal{T}_v + \mathcal{T}_v^2 \mathfrak{Re}[\tilde{\Sigma}_2(0, n_0 \mathcal{T}_v)] + \mathcal{T}_v^3 \mathfrak{Re}[\tilde{\Sigma}_3(0,0)] \tag{A.3}$$

where we have inserted the first order energy-shift into the second order self-energy. As an example we now evaluate the first diagram in Fig. 5.4(a), which yields

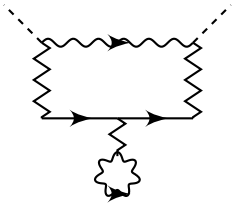

$$= n_0^2 \mathcal{T}_v^3 \int \frac{\mathrm{d}^3 p}{(2\pi)^3} \frac{u_p^2}{(\omega - E_p - \epsilon_p)}. \tag{A.4}$$

Likewise, inserting the first order energy shift into the diagram Fig. 5.2(a) and expanding to third order, we obtain

$$\Sigma_{2a}(0, n_0\mathcal{T}_v) = n_0\mathcal{T}_v^2 \int \frac{\mathrm{d}^3 p}{(2\pi)^3} \frac{u_p^2}{n_0\mathcal{T}_v - E_p - \epsilon_p} \approx -n_0\mathcal{T}_v^2 \int \frac{\mathrm{d}^3 p}{(2\pi)^3} \frac{u_p^2}{E_p + \epsilon_p} \Big(1 + \frac{n_0\mathcal{T}_v}{E_p + \epsilon_p}\Big). \tag{A.5}$$

Hence, we see that the third order term of Eq. (A.5) exactly cancels Eq. (A.4) with $\omega = 0$. Completely analogous calculations cancels the remaining third order diagrams in Fig. 5.4(a).

A.3 LIFETIME OF THE BOSE POLARON

We evaluate the imaginary part of the second order self-energy for finite momentum in order to determine the polaron lifetime τ through $1/\tau = -2\mathfrak{Im}\Sigma$. Starting from Eq. (5.20) and doing analytic continuation, we obtain for the imaginary part

$$\begin{aligned}\mathfrak{Im}[\Sigma_2(\epsilon_p, \boldsymbol{p})] &= -\pi n_0\mathcal{T}_v^2 \int \frac{\mathrm{d}^3 q}{(2\pi)^3} \frac{\epsilon_q^{\mathrm{B}}}{E_q} \delta\big(\epsilon_q - E_q - \epsilon_{p-q}\big) \\ &= -2\pi n_0 m_{\mathrm{B}} \mathcal{T}_v^2 (m_{\mathrm{B}} n_0 \mathcal{T}_{\mathrm{B}})^{1/2} \mathfrak{Im}[\tilde{\Sigma}_2(k)] \\ &= -2\sqrt{2}\pi^2 n_0 \mathcal{T}_v \frac{1+\alpha}{\alpha} \frac{a}{\xi} \mathfrak{Im}[\tilde{\Sigma}_2(k)],\end{aligned} \tag{A.6}$$

where $\mathfrak{Im}[\tilde{\Sigma}_2(k)]$ is a dimensionless integral with $k = p/\sqrt{m_{\mathrm{B}} n_0 \mathcal{T}_{\mathrm{B}}} = \sqrt{2}\xi\, p$ given by

$$\mathfrak{Im}[\tilde{\Sigma}_2(k)] = \int \frac{\mathrm{d}^3 q}{(2\pi)^3} \frac{q^2}{\sqrt{q^2(q^2+4)}} \times \delta\big(2\frac{pk}{\alpha}\cos\theta - (\sqrt{q^2(q^2+4)} + \frac{q^2}{\alpha})\big). \tag{A.7}$$

From the δ-function, we can read off the constraint $k \geq k_c = \alpha \Leftrightarrow p \geq p_c = mc$ with $c = \sqrt{n_0\mathcal{T}_{\mathrm{B}}/m_{\mathrm{B}}}$ the speed of sound in the BEC.

We can also determine an upper limit for the dimensionless integration variable from the δ-function, namely

$$q_{\max}(k) = \frac{2}{1-\alpha^2}\left(k - \alpha\sqrt{1-\alpha^2+k^2}\right). \tag{A.8}$$

Thus

$$\begin{aligned}\mathfrak{Im}[\tilde{\Sigma}_2(k)] &= \frac{\alpha}{2(2\pi)^2 k}\int_0^{q_{\max}(k)} \mathrm{d}q\, \frac{q^3}{\sqrt{q^2(q^2+4)}} \\ &= \frac{\alpha}{2(2\pi)^2 k}\left[\frac{1}{2}q_{\max}(k)\sqrt{[q_{\max}(k)]^2+4} - 2\sinh^{-1}\left(\frac{q_{\max}(k)}{2}\right)\right].\end{aligned}$$

Inserting into Eq. (A.6), we obtain

$$\begin{aligned}\mathfrak{Im}[\Sigma_2(\epsilon_p, \boldsymbol{p})] &= -n_0 \mathcal{T}_v \frac{1+\alpha}{2}\frac{a}{\xi}\xi p \\ &\times\left[\frac{1}{2}q_{\max}(\sqrt{2}\xi p)\sqrt{[q_{\max}(\sqrt{2}\xi p)]^2+4} - 2\sinh^{-1}\left(\frac{q_{\max}(\sqrt{2}\xi p)}{2}\right)\right].\end{aligned}$$

Taking $k = k_c + \delta$ with δ small, we have $q_{\max}(k) \approx 2\delta$, and we obtain for Appendix A.3 to lowest order in δ:

$$\mathfrak{Im}[\tilde{\Sigma}_2(k)] \approx \frac{\alpha}{6\pi^2}\frac{\delta^3}{k_c} = \frac{\alpha}{6\pi^2}\frac{(k-k_c)^3}{k_c}. \tag{A.9}$$

Inserting back into Eq. (A.6), we finally obtain

$$\mathfrak{Im}[\Sigma_2(\epsilon_p, \boldsymbol{p})] = -\frac{n_0}{3\pi^2}\frac{m\mathcal{T}_v^2}{\sqrt{m_B n_0 \mathcal{T}_B}}\frac{(p-p_c)^3}{p_c} \tag{A.10}$$

or for the lifetime

$$\frac{1}{\tau_{p\gtrsim p_c}} = \frac{2n_0}{3\pi^2}\frac{m\mathcal{T}_v^2}{\sqrt{m_B n_0 \mathcal{T}_B}}\frac{(p-p_c)^3}{p_c} \tag{A.11}$$

A.4 $\mathfrak{Im}[\Sigma(\omega, E_{\rm pol})]$

Using $G(i\omega_\lambda) = [i\omega_\lambda - E_{\rm pol}]^{-1}$ in the second order diagrams Figs. 5.2(a-d), we obtain imaginary part of the self-energy:

$$\mathfrak{Im}[\Sigma(\omega, E_{\rm pol})] = -\pi n_0 \mathcal{T}_v^2 \int \frac{\mathrm{d}^3 q}{(2\pi)^3} \frac{\epsilon_q^{\rm B}}{E_q} \delta(\omega - E_{\rm pol} - \epsilon_q - E_q), \tag{A.12}$$

which we calculate in the equal mass case setting $m = m_{\rm B}$ and hence $\epsilon_q^{\rm B} = \epsilon_q$. We see that we obtain a finite imaginary part for $\hat{\omega} = \omega - E_{\rm pol} > 0$ and thus, as discussed in the main text that the continuum of excitations lies above $E_{\rm pol}$.

Rewriting the δ-function in Eq. (A.12) and solving for ϵ_q, we have

$$0 = \hat{\omega} - \epsilon_q - E_q \Leftrightarrow \epsilon_q = \frac{\hat{\omega}^2}{2(\hat{\omega} + n_0 \mathcal{T}_{\rm B})}, \tag{A.13}$$

$$\delta(\hat{\omega} - \epsilon_q - E_q) = \frac{\delta\left(\epsilon_q - \frac{\hat{\omega}^2}{2(\hat{\omega} + n_0 \mathcal{T}_{\rm B})}\right)}{1 + \frac{\epsilon_q + n_0 \mathcal{T}_{\rm B}}{E_q}} \tag{A.14}$$

and we get for the imaginary part of the self-energy

$$\begin{aligned}
\mathfrak{Im}\big[\Sigma(\hat{\omega})\big] &= -\frac{n_0 \mathcal{T}_v^2}{2\pi} \int_0^\infty \mathrm{d}q\, q^2 \frac{\epsilon_q}{E_q} \delta(\hat{\omega} - \epsilon_q - E_q) \\
&= -\frac{n_0 \mathcal{T}_v^2}{2\pi} \sqrt{\frac{m}{2}} \int_0^\infty \frac{\mathrm{d}\epsilon_q}{\sqrt{\epsilon_q}} 2m\epsilon_q \frac{\epsilon_q}{E_q} \frac{\delta\left(\epsilon_q - \frac{\hat{\omega}^2}{2(\hat{\omega} + n_0 \mathcal{T}_{\rm B})}\right)}{1 + \frac{\epsilon_q + n_0 \mathcal{T}_{\rm B}}{E_q}} \\
&= -\frac{m n_0 \mathcal{T}_v^2 \sqrt{m n_0 \mathcal{T}_{\rm B}}}{4\pi} \frac{(\hat{\omega}/n_0 \mathcal{T}_{\rm B})^3}{(1 + \hat{\omega}/n_0 \mathcal{T}_{\rm B})^{5/2}}.
\end{aligned} \tag{A.15}$$

Changing to dimensionless units in terms of $E_n = k_n^2/2m$, $k_n = (6\pi^2 n_0)^{1/3}$, we have

$$\frac{\mathfrak{Im}[\Sigma(\hat{\omega})]}{E_n} = -\frac{4(k_n a)^2}{3\pi} \sqrt{\frac{2k_n a_{\rm B}}{3\pi}} \frac{(\hat{\omega}/n_0 \mathcal{T}_{\rm B})^3}{(1 + \hat{\omega}/n_0 \mathcal{T}_{\rm B})^{5/2}}, \tag{A.16}$$

with $\hat{\omega} = \omega - E_{\mathrm{pol}}$, where we also note that

$$\frac{\hat{\omega}}{n_0 \mathcal{T}_{\mathrm{B}}} = \frac{3\pi\hat{\omega}/E_n}{4k_n a_{\mathrm{B}}}\,. \tag{A.17}$$

Bibliography

[1] S. N. Bose. Plancks Gesetz und Lichtquantenhypothese. *Zeitschrift für Physik*, **26**: 178–181, 1924. DOI: 10.1007/BF01327326. (see p. 1)

[2] A. Einstein. *Quantentheorie des einatomigen idealen Gases*. Akademie der Wissenshaften, in Kommission bei W. de Gruyter, 1924. (see p. 1)

[3] E. Fermi. Zur Quantelung des idealen einatomigen Gases. *Zeitschrift für Physik*, **36**: 902–912, 1926. DOI: 10.1007/BF01400221 Reprinted in: ed. Emilo Segrè, *The Collected Papers of Enrico Fermi. vol. 1. Italy, 1921-1938*, (University of Chicago Press, 1962). (see p. 1)

[4] E. Fermi. Sulla quantizzazione del gas perfetto monoatomico. *Rendiconti Lincei*, **3**: 145–149, 1926. Reprinted in: ed. Emilo Segrè, *The Collected Papers of Enrico Fermi. vol. 1. Italy, 1921-1938*, (University of Chicago Press, 1962). (see p. 1)

[5] P. A. M. Dirac. On the Theory of Quantum Mechanics. *Proceedings of the Royal Society of London A*, **112**: 661–677, 1926. DOI: 10.1098/rspa.1926.0133. (see p. 1)

[6] W. Pauli. Über den Zusammenhang des Abschlusses der Elektronengruppen im Atom mit der Komplexstruktur der

Spektren. *Zeitschrift für Physik*, **31**: 765–783, 1925. DOI: 10.1007/BF02980631. (see p. 1)

[7] S. Giorgini, L. P. Pitaevskii, and S. Stringari. Theory of ultracold atomic Fermi gases. *Reviews of Modern Physics*, **80**: 1215–1274, 2008. DOI: 10.1103/RevModPhys.80.1215. (see pp. 1, 55)

[8] K. B. Davis, M. .-.-O. Mewes, M. R. Andrews, N. J. van Druten, D. S. Durfee, D. M. Kurn, and W. Ketterle. Bose-Einstein Condensation in a Gas of Sodium Atoms. *Physical Review Letters*, **75**: 3969–3973, 1995. DOI: 10.1103/PhysRevLett.75.3969. (see p. 2)

[9] M. H. Anderson, J. R. Ensher, M. R. Matthews, C. E. Wieman, and E. A. Cornell. Observation of Bose-Einstein Condensation in a Dilute Atomic Vapor. *Science*, **269**: 198–201, 1995. DOI: 10.1126/science.269.5221.198. (see p. 2)

[10] C. C. Bradley, C. A. Sackett, J. J. Tollett, and R. G. Hulet. Evidence of Bose-Einstein Condensation in an Atomic Gas with Attractive Interactions. *Physical Review Letters*, **75**: 1687–1690, 1995. DOI: 10.1103/PhysRevLett.75.1687. (see p. 2)

[11] B. DeMarco and D. S. Jin. Onset of Fermi Degeneracy in a Trapped Atomic Gas. *Science*, **285**: 1703–1706, 1999. DOI: 10.1126/science.285.5434.1703. (see p. 2)

[12] F. Schreck, L. Khaykovich, K. L. Corwin, G. Ferrari, T. Bourdel, J. Cubizolles, and C. Salomon. Quasipure Bose-Einstein Condensate Immersed in a Fermi Sea. *Physical Review Letters*, **87**: 080403, 2001. DOI: 10.1103/PhysRevLett.87.080403. (see p. 2)

[13] A. G. Truscott, K. E. Strecker, W. I. McAlexander, G. B. Partridge, and R. G. Hulet. Observation of Fermi Pressure in a Gas of Trapped Atoms. *Science*, **291**: 2570–2572, 2001. DOI: 10.1126/science.1059318. (see p. 2)

[14] J. Bardeen. Wave Functions for Superconducting Electrons. *Physical Review*, **80**: 567–574, 1950. DOI: 10.1103/PhysRev.80.567. (see p. 2)

[15] J. Bardeen, L. N. Cooper, and J. R. Schrieffer. Theory of Superconductivity. *Physical Review*, **108**: 1175–1204, 1957. DOI: 10.1103/PhysRev.108.1175. (see p. 2)

[16] L. N. Cooper. Bound Electron Pairs in a Degenerate Fermi Gas. *Physical Review*, **104**: 1189–1190, 1956. DOI: 10.1103/PhysRev.104.1189. (see p. 2)

[17] C. A. Regal, M. Greiner, and D. S. Jin. Observation of Resonance Condensation of Fermionic Atom Pairs. *Physical Review Letters*, **92**: 040403, 2004. DOI: 10.1103/PhysRevLett.92.040403. (see p. 2)

[18] M. W. Zwierlein, J. R. Abo-Shaeer, A. Schirotzek, C. H. Schunck, and W. Ketterle. Vortices and superfluidity in a strongly interacting Fermi gas. *Nature*, **435**: 1047–1051, 2005. DOI: 10.1038/nature03858. (see p. 2)

[19] I. Bloch, J. Dalibard, and W. Zwerger. Many-body physics with ultracold gases. *Reviews of Modern Physics*, **80**: 885–964, 2008. DOI: 10.1103/RevModPhys.80.885. (see p. 2)

[20] L. D. Landau and V. Ginzburg. On the theory of superconductivity. *Journal of Experimental and Theoretical Physics*, **20**: 1064, 1950. (see p. 2)

[21] H. Feshbach. A unified theory of nuclear reactions. II. *Annals of Physics*, **19**: 287–313, 1962. DOI: 10.1016/0003-4916(62)90221-X. (see p. 3)

[22] W. C. Stwalley. Stability of Spin-Aligned Hydrogen at Low Temperatures and High Magnetic Fields: New Field-Dependent Scattering Resonances and Predissociations. *Physical Review Letters*, **37**: 1628–1631, 1976. DOI: 10.1103/PhysRevLett.37.1628. (see p. 3)

[23] S. Inouye, M. R. Andrews, J. Stenger, H.-J. Miesner, D. M. Stamper-Kurn, and W. Ketterle. Observation of Feshbach resonances in a Bose-Einstein condensate. *Nature*, **392**: 151–154, 1998. DOI: 10.1038/32354. (see p. 3)

[24] C. Chin, R. Grimm, P. Julienne, and E. Tiesinga. Feshbach resonances in ultracold gases. *Reviews of Modern Physics*, **82**: 1225–1286, 2010. DOI: 10.1103/RevModPhys.82.1225. (see pp. 3, 7–9)

[25] G. B. Partridge, W. Li, R. I. Kamar, Y.-a. Liao, and R. G. Hulet. Pairing and Phase Separation in a Polarized Fermi Gas. *Science*, **311**: 503–505, 2006. DOI: 10.1126/science.1122876. (see p. 3)

[26] M. W. Zwierlein, A. Schirotzek, C. H. Schunck, and W. Ketterle. Fermionic Superfluidity with Imbalanced Spin Populations. *Science*, **311**: 492–496, 2006. DOI: 10.1126/science.1122318. (see p. 3)

[27] F. Chevy and C. Mora. Ultra-cold polarized Fermi gases. *Reports on Progress in Physics*, **73**: 112401, 2010. (see p. 3)

[28] K. Gubbels and H. Stoof. Imbalanced Fermi gases at unitarity. *Physics Reports*, **525**: Imbalanced Fermi Gases at Unitarity, 255–313, 2013. DOI: http://dx.doi.org/10.1016/j.physrep.2012.11.004. (see p. 3)

[29] A. P. Chikkatur, A. Görlitz, D. M. Stamper-Kurn, S. Inouye, S. Gupta, and W. Ketterle. Suppression and Enhancement of Impurity Scattering in a Bose-Einstein Condensate. *Physical Review Letters*, **85**: 483–486, 2000. DOI: 10.1103/PhysRevLett.85.483. (see p. 3)

[30] N. Spethmann, F. Kindermann, S. John, C. Weber, D. Meschede, and A. Widera. Dynamics of Single Neutral Impurity Atoms Immersed in an Ultracold Gas. *Physical Review Letters*, **109**: 235301, 2012. DOI: 10.1103/PhysRevLett.109.235301. (see p. 3)

[31] L. D. Landau. *Physikalische Zeitschrift der Sowjetunion*, **3**: 644, 1933. (see pp. 3, 12)

[32] S. I. Pekar. *Zhurnal Eksperimental'noi i Teoreticheskoi Fiziki (Journal of Experimental and Theoretical Physics)*, **16**: 335, 1946. (see pp. 3, 12)

[33] L. D. Landau and S. I. Pekar. *Physikalische Zeitschrift der Sowjetunion*, **18**: 419, 1948. (see p. 3)

[34] M. E. Gershenson, V. Podzorov, and A. F. Morpurgo. Colloquium. *Reviews of Modern Physics*, **78**: 973–989, 2006. DOI: 10.1103/RevModPhys.78.973. (see p. 3)

[35] G. Baym and C. Pethick. *Landau Fermi-Liquid Theory: Concepts and Applications*. Wiley, 1991. (see pp. 3, 37)

[36] R. Bishop. On the ground state of an impurity in a dilute fermi gas. *Annals of Physics*, **78**: 391–420, 1973. DOI: http://dx.doi.org/10.1016/0003-4916(73)90265-0. (see p. 3)

[37] E. Dagotto. Correlated electrons in high-temperature superconductors. *Reviews of Modern Physics*, **66**: 763–840, 1994. DOI: 10.1103/RevModPhys.66.763. (see p. 3)

[38] S. Chatrchyan et al. Observation of a new boson at a mass of 125 GeV with the {CMS} experiment at the {LHC}. *Physics Letters B*, **716**: 30, 2012. DOI: 10.1016/j.physletb.2012.08.021. (see p. 4)

[39] G. Aad et al. Observation of a new particle in the search for the Standard Model Higgs boson with the {ATLAS} detector at the {LHC}. *Physics Letters B*, **716**: 1, 2012. DOI: 10.1016/j.physletb.2012.08.020. (see p. 4)

[40] P. W. Higgs. Broken Symmetries and the Masses of Gauge Bosons. *Physical Review Letters*, **13**: 508–509, 1964. DOI: 10.1103/PhysRevLett.13.508. (see p. 4)

[41] A. Schirotzek, C.-H. Wu, A. Sommer, and M. W. Zwierlein. Observation of Fermi Polarons in a Tunable Fermi Liquid of Ultracold Atoms. *Physical Review Letters*, **102**: 230402, 2009. DOI: 10.1103/PhysRevLett.102.230402. (see pp. 4, 36, 52)

[42] C. Kohstall et al. Metastability and coherence of repulsive polarons in a strongly interacting Fermi mixture. *Nature*, **485**: 615–618, 2012. DOI: 10.1038/nature11065. (see pp. 4, 36, 52, 59, 91)

[43] M. Koschorreck, D. Pertot, E. Vogt, B. Fröhlich, M. Feld, and M. Köhl. Attractive and repulsive Fermi polarons in two dimensions. *Nature*, **485**: 619–622, 2012. DOI: 10.1038/nature11151. (see pp. 4, 36, 52)

[44] N. B. Jørgensen et al. Observation of Attractive and Repulsive Polarons in a Bose-Einstein Condensate. *Physical Review Letters*, **117**: 055302, 2016. DOI: 10.1103/PhysRevLett.117.055302. (see pp. 4, 5, 18, 27, 63, 91, 93, 95, 97, 106, 111)

[45] M.-G. Hu, M. J. Van de Graaff, D. Kedar, J. P. Corson, E. A. Cornell, and D. S. Jin. Bose Polarons in the Strongly Interacting Regime. *Physical Review Letters*, **117**: 055301, 2016. DOI: 10.1103/PhysRevLett.117.055301. (see pp. 4, 91, 93)

[46] F. Scazza et al. Repulsive Fermi Polarons in a Resonant Mixture of Ultracold ^{6}Li Atoms. *Physical Review Letters*, **118**: 083602, 2017. DOI: 10.1103/PhysRevLett.118.083602. (see p. 4)

[47] F. Chevy. Universal phase diagram of a strongly interacting Fermi gas with unbalanced spin populations. *Physical Review A*, **74**: 063628, 2006. DOI: 10.1103/PhysRevA.74.063628. (see pp. 4, 17, 36)

[48] P. Massignan, M. Zaccanti, and G. M. Bruun. Polarons, dressed molecules and itinerant ferromagnetism in ultracold Fermi gases. *Reports on Progress in Physics*, **77**: 034401, 2014. DOI: 10.1088/0034-4885/77/3/034401. (see pp. 4, 17, 36, 40, 61)

[49] J. Tempere, W. Casteels, M. K. Oberthaler, S. Knoop, E. Timmermans, and J. T. Devreese. Feynman path-integral treatment of the BEC-impurity polaron. *Physical Review B*, **80**: 184504, 2009. DOI: 10.1103/PhysRevB.80.184504. (see p. 4)

[50] S. P. Rath and R. Schmidt. Field-theoretical study of the Bose polaron. *Physical Review A*, **88**: 053632, 2013. DOI: 10.1103/PhysRevA.88.053632. (see p. 4)

[51] F. M. Cucchietti and E. Timmermans. Strong-Coupling Polarons in Dilute Gas Bose-Einstein Condensates. *Physical Review Letters*, **96**: 210401, 2006. DOI: 10.1103/PhysRevLett.96.210401. (see p. 4)

[52] R. S. Christensen and G. M. Bruun. Quasiparticle scattering rate in a strongly polarized Fermi mixture. *Physical Review A*, **91**: 042702, 2015. DOI: 10.1103/PhysRevA.91.042702. (see pp. 5, 35, 51)

[53] M. Cetina, M. Jag, R. S. Lous, J. T. M. Walraven, R. Grimm, R. S. Christensen, and G. M. Bruun. Decoherence of Impurities in a Fermi Sea of Ultracold Atoms. *Physical Review Letters*, **115**: 135302, 2015. DOI: 10.1103/PhysRevLett.115.135302. (see pp. 5, 35, 36, 38, 40, 44, 45, 51, 52, 55, 58–60)

[54] R. S. Christensen, J. Levinsen, and G. M. Bruun. Quasiparticle Properties of a Mobile Impurity in a Bose-Einstein Condensate. *Physical Review Letters*, **115**: 160401, 2015. DOI: 10.1103/PhysRevLett.115.160401. (see pp. 5, 63, 93)

[55] C. Pethick and H. Smith. *Bose-Einstein Condensation in Dilute Gases*. Cambridge University Press, 2002. (see pp. 7–9, 37, 39, 69, 96)

[56] W. Ketterle and Z. M. W. "Making, probing and understanding ultracold Fermi gases" in: *Proceedings of the International School of Physics "Enrico Fermi", Course CLXIV, Ultra-cold Fermi Gases*. ed. by M. Inguscio, W. Ketterle, and C. Salomon IOS Press, 2007. pp. 95–287 (see pp. 7, 25)

[57] A. Fetter and J. Walecka. *Quantum theory of many-particle systems*. McGraw-Hill, 1971. (see pp. 8, 10, 11, 13, 66, 69, 80)

[58] G. Mahan. *Many-Particle Physics*. Plenum Press, 1990. (see pp. 8, 10, 13)

[59] H. Bruus and K. Flensberg. *Many-Body Quantum Theory in Condensed Matter Physics: An Introduction*. Oxford University Press, 2004. (see pp. 8, 10, 13, 17, 37, 66, 69)

[60] A. J. Moerdijk, B. J. Verhaar, and A. Axelsson. Resonances in ultracold collisions of ^{6}Li, ^{7}Li, and ^{23}Na. *Physical Review A*, **51**: 4852–4861, 1995. DOI: 10.1103/PhysRevA.51.4852. (see p. 8)

[61] Z. Lan and C. Lobo. A Single Impurity in an Ideal Atomic Fermi Gas: Current Understanding and Some Open Problems. *Journal of the Indian Institute of Science*, 2014. (see p. 17)

[62] D. A. Steck *Quantum and Atom Optics* available online at http://steck.us/teaching (revision 0.11.5, 27 November 2016) (see pp. 19, 20, 24, 25, 27)

[63] Glosser.ca available online at https://commons.wikimedia.org/wiki/File:Bloch_Sphere.svg (see p. 21)

[64] F. Bloch. Nuclear Induction. *Physical Review*, **70**: 460–474, 1946. DOI: 10.1103/PhysRev.70.460. (see p. 22)

[65] F. Arecchi and R. Bonifacio. Theory of Optical Maser Amplifiers. *IEEE Journal of Quantum Electronics*, **1**: 169–178, 1965. DOI: 10.1109/JQE.1965.1072212. (see p. 22)

[66] M. A. Nielsen and I. L. Chuang. *Quantum Computation and Quantum Information*. Cambridge University Press, 2000. (see p. 23)

[67] M. Cetina, M. Jag, and R. Lous *Measurements of Polaron Coherence by Spin Echo* personal communication Feb. 17, 2014 (see pp. 24, 25, 30)

[68] G. M. Bruun *Ramsey and Spin Echo Spectroscopy and Many-Body Correlations* personal communication May 11, 2015 (see pp. 25, 28)

[69] M. W. Zwierlein, Z. Hadzibabic, S. Gupta, and W. Ketterle. Spectroscopic Insensitivity to Cold Collisions in a Two-State Mixture of Fermions. *Physical Review Letters*, **91**: 250404, 2003. DOI: 10.1103/PhysRevLett.91.250404. (see p. 25)

[70] B. D. Esry, C. H. Greene, and J. P. Burke. Recombination of Three Atoms in the Ultracold Limit. *Physical Review Letters*, **83**: 1751–1754, 1999. DOI: 10.1103/PhysRevLett.83.1751. (see p. 27)

[71] E. Nielsen and J. H. Macek. Low-Energy Recombination of Identical Bosons by Three-Body Collisions. *Physical Review Letters*, **83**: 1566–1569, 1999. DOI: 10.1103/PhysRevLett.83.1566. (see p. 27)

[72] A. D. Cronin, J. Schmiedmayer, and D. E. Pritchard. Optics and interferometry with atoms and molecules. *Reviews of Modern Physics*, **81**: 1051–1129, 2009. DOI: 10.1103/RevModPhys.81.1051. (see pp. 31, 52)

[73] M. Knap, A. Shashi, Y. Nishida, A. Imambekov, D. A. Abanin, and E. Demler. Time-Dependent Impurity in Ultracold Fermions: Orthogonality Catastrophe and Beyond. *Physical Review X*, **2**: 041020, 2012. DOI: 10.1103/PhysRevX.2.041020. (see pp. 31, 52)

[74] G. W. Morley available online at https://commons.wikimedia.org/wiki/File:GWM_HahnEchoDecay.gif (see p. 33)

[75] G. W. Morley available online at https://commons.wikimedia.org/wiki/File:GWM_HahnEcho.gif (see p. 33)

[76] R. S. Christensen. *Collision Rate of Polarons*. Master's Thesis. Aarhus University, Aug. 2013. (see pp. 35, 37, 39, 47, 48, 51, 53, 93)

[77] C. Lobo, A. Recati, S. Giorgini, and S. Stringari. Normal State of a Polarized Fermi Gas at Unitarity. *Physical Review Letters*, **97**: 200403, 2006. DOI: 10.1103/PhysRevLett.97.200403. (see p. 36)

[78] M. Punk, P. T. Dumitrescu, and W. Zwerger. Polaron-to-molecule transition in a strongly imbalanced Fermi gas. *Physical Review A*, **80**: 053605, 2009. DOI: 10.1103/PhysRevA.80.053605. (see p. 36)

[79] N. Prokof'ev and B. Svistunov. Fermi-polaron problem: Diagrammatic Monte Carlo method for divergent sign-alternating series. *Physical Review B*, **77**: 020408, 2008. DOI: 10.1103/PhysRevB.77.020408. (see p. 36)

[80] C. J. M. Mathy, M. M. Parish, and D. A. Huse. Trimers, Molecules, and Polarons in Mass-Imbalanced Atomic Fermi Gases. *Physical Review Letters*, **106**: 166404, 2011. DOI: 10.1103/PhysRevLett.106.166404. (see p. 36)

[81] G. M. Bruun, A. Recati, C. J. Pethick, H. Smith, and S. Stringari. Collisional Properties of a Polarized Fermi Gas with Resonant Interactions. *Physical Review Letters*, **100**: 240406, 2008. DOI: 10.1103/PhysRevLett.100.240406. (see p. 36)

[82] C. Trefzger and Y. Castin. Energy, decay rate, and effective masses for a moving polaron in a Fermi sea: Explicit results in the weakly attractive limit. *Europhysics Letters*, **104**: 50005, 2013. DOI: 10.1209/0295-5075/104/50005. (see p. 36)

[83] C. Trefzger and Y. Castin. Self-energy of an impurity in an ideal Fermi gas to second order in the interaction strength. *Physical Review A*, **90**: 033619, 2014. DOI: 10.1103/PhysRevA.90.033619. (see p. 36)

[84] Z. Lan, G. M. Bruun, and C. Lobo. Quasiparticle Lifetime in Ultracold Fermionic Mixtures with Density and Mass Imbalance. *Physical Review Letters*, **111**: 145301, 2013. DOI: 10.1103/PhysRevLett.111.145301. (see p. 36)

[85] J. J. Kinnunen. Hartree shift in unitary Fermi gases. *Physical Review A*, **85**: 012701, 2012. DOI: 10.1103/PhysRevA.85.012701. (see p. 36)

[86] Y. Nishida. Probing strongly interacting atomic gases with energetic atoms. *Physical Review A*, **85**: 053643, 2012. DOI: 10.1103/PhysRevA.85.053643. (see p. 36)

[87] G. M. Bruun, A. D. Jackson, and E. E. Kolomeitsev. Multichannel scattering and Feshbach resonances: Effective theory, phenomenology, and many-body effects. *Physical Review A*, **71**: 052713, 2005. DOI: 10.1103/PhysRevA.71.052713. (see p. 39)

[88] S. Riedl et al. Collective oscillations of a Fermi gas in the unitarity limit: Temperature effects and the role of pair correlations. *Physical Review A*, **78**: 053609, 2008. DOI: 10.1103/PhysRevA.78.053609. (see p. 49)

[89] S. K. Baur, E. Vogt, M. Köhl, and G. M. Bruun. Collective modes of a two-dimensional spin-1/2 Fermi gas in a harmonic trap. *Physical Review A*, **87**: 043612, 2013. DOI: 10.1103/PhysRevA.87.043612. (see p. 49)

[90] M. Urban, S. Chiacchiera, D. Davesne, T. Enss, and P.-A. Pantel. Collective modes of three- and two-dimensional trapped Fermi gases in the normal phase. *Journal of Physics: Conference Series*, **497**: 012028, 2014. DOI: 10.1088/1742-6596/497/1/012028. (see p. 49)

[91] G. M. Bruun and H. Smith. Viscosity and thermal relaxation for a resonantly interacting Fermi gas. *Physical Review A*, **72**: 043605, 2005. DOI: 10.1103/PhysRevA.72.043605. (see p. 49)

[92] T. Enss, C. Küppersbusch, and L. Fritz. Shear viscosity and spin diffusion in a two-dimensional Fermi gas. *Physical Review A*, **86**: 013617, 2012. DOI: 10.1103/PhysRevA.86.013617. (see p. 49)

[93] T. Enss. Transverse spin diffusion in strongly interacting Fermi gases. *Physical Review A*, **88**: 033630, 2013. DOI: 10.1103/PhysRevA.88.033630. (see p. 49)

[94] M. Cetina et al. Ultrafast many-body interferometry of impurities coupled to a Fermi sea. *Science*, **354**: 96–99, 2016. DOI: 10.1126/science.aaf5134. (see pp. 52, 61)

[95] M. Inguscio, W. Ketterle, and C. Salomon, eds. *Proceedings of the International School of Physics "Enrico Fermi", Course CLXIV, Ultra-cold Fermi Gases* IOS Press, 2007 (see p. 55)

[96] M. Cetina personal communication Apr. 9, 2015 (see p. 56)

[97] J. Korringa. Nuclear magnetic relaxation and resonnance line shift in metals. *Physica*, **16**: 601–610, 1950. DOI: http://dx.doi.org/10.1016/0031-8914(50)90105-4. (see p. 60)

[98] F. Grusdt, Y. E. Shchadilova, A. N. Rubtsov, and E. Demler. Renormalization group approach to the Fröhlich polaron model: application to impurity-BEC problem. *Scientific Reports*, **5**: 12124, 2015. DOI: 10.1038/srep12124. (see pp. 63, 80, 93)

[99] W. Casteels and M. Wouters. Polaron formation in the vicinity of a narrow Feshbach resonance. *Physical Review A*, **90**: 043602, 2014. DOI: 10.1103/PhysRevA.90.043602. (see pp. 63, 72, 74, 80, 90, 93)

[100] H. Bei-Bing and W. Shao-Long. Polaron in Bose–Einstein–Condensation System. *Chinese Physics Letters*, **26**: 080302, 2009. DOI: 10.1088/0256-307X/26/8/080302. (see pp. 63, 74, 93)

[101] H. Fröhlich, H. Pelzer, and S. Zienau. XX. Properties of slow electrons in polar materials. *The London, Edinburgh, and Dublin Philosophical Magazine and Journal of Science*, **41**: 221–242, 1950. DOI: 10.1080/14786445008521794. (see pp. 63, 73)

[102] J. Levinsen, M. M. Parish, and G. M. Bruun. Impurity in a Bose-Einstein Condensate and the Efimov Effect. *Physical Review Letters*, **115**: 125302, 2015. DOI: 10.1103/PhysRevLett.115.125302. (see pp. 64, 93, 111)

[103] Y. E. Shchadilova, R. Schmidt, F. Grusdt, and E. Demler. Quantum Dynamics of Ultracold Bose Polarons. *Physical Review Letters*, **117**: 113002, 2016. DOI: 10.1103/PhysRevLett.117.113002. (see pp. 64, 93, 111)

[104] N. N. Bogoliubov. On the Theory of Superfluidity. *Journal of Physics*, **11**: 23–32, 1947. Reprinted in D. Pines, *The Many-Body Problem*, (New York, W. A. Benjamin, 1961), p. 292. (see p. 65)

[105] A. P. Albus, S. A. Gardiner, F. Illuminati, and M. Wilkens. Quantum field theory of dilute homogeneous Bose-Fermi mixtures at zero temperature: General formalism and beyond mean-field corrections. *Physical Review A*, **65**: 053607, 2002. DOI: 10.1103/PhysRevA.65.053607. (see p. 66)

[106] L. Landau. Theory of the Superfluidity of Helium II. *Physical Review*, **60**: 356–358, 1941. DOI: 10.1103/PhysRev.60.356. (see p. 72)

[107] T. D. Lee and C. N. Yang. Many-Body Problem in Quantum Mechanics and Quantum Statistical Mechanics. *Physical Review*, **105**: 1119–1120, 1957. DOI: 10.1103/PhysRev.105.1119. (see p. 80)

[108] T. D. Lee, K. Huang, and C. N. Yang. Eigenvalues and Eigenfunctions of a Bose System of Hard Spheres and Its Low-Temperature Properties. *Physical Review*, **106**: 1135–1145, 1957. DOI: 10.1103/PhysRev.106.1135. (see p. 80)

[109] K. A. Brueckner and K. Sawada. Bose-Einstein Gas with Repulsive Interactions: General Theory. *Physical Review*, **106**: 1117–1127, 1957. DOI: 10.1103/PhysRev.106.1117. (see p. 80)

[110] T. T. Wu. Ground State of a Bose System of Hard Spheres. *Physical Review*, **115**: 1390–1404, 1959. DOI: 10.1103/PhysRev.115.1390. (see p. 80)

[111] K. Sawada. Ground-State Energy of Bose-Einstein Gas with Repulsive Interaction. *Physical Review*, **116**: 1344–1358, 1959. DOI: 10.1103/PhysRev.116.1344. (see p. 80)

[112] N. M. Hugenholtz and D. Pines. Ground-State Energy and Excitation Spectrum of a System of Interacting Bosons. *Physical Review*, **116**: 489–506, 1959. DOI: 10.1103/PhysRev.116.489. (see p. 80)

[113] P. W. Anderson. Infrared Catastrophe in Fermi Gases with Local Scattering Potentials. *Physical Review Letters*, **18**: 1049–1051, 1967. DOI: 10.1103/PhysRevLett.18.1049. (see p. 89)

[114] J. Kondo. Resistance Minimum in Dilute Magnetic Alloys. *Progress of Theoretical Physics*, **32**: 37, 1964. DOI: 10.1143/PTP.32.37. (see p. 89)

[115] F. Dalfovo, S. Giorgini, L. P. Pitaevskii, and S. Stringari. Theory of Bose-Einstein condensation in trapped gases. *Reviews of Modern Physics*, **71**: 463–512, 1999. DOI: 10.1103/RevModPhys.71.463. (see p. 96)